Corrosion of Reinforcing Steel in Loaded Cracked Concretes exposed to De-icing Salts

by
Antonio R. Mendoza

A thesis
presented to the University of Waterloo
in fulfilment of the
thesis requirement for the degree of
Master of Applied Science
in
Mechanical Engineering

Waterloo, Ontario, Canada, 2003

I hereby declare that I am the sole author of this thesis. This is a true copy of the thesis, including any required final revisions, as accepted by my examiners. I understand that my thesis may be made electronically available to the public.

Abstract

The corrosion of the reinforcing steel in concrete by de-icing salts is one of the major issues concerning the durability of reinforced concrete. Different methods have been used to protect the reinforcing steel, but still corrosion of reinforced structures continues to be a big problem causing enormous costs in their restoration and rehabilitation.

The continuity of the pores of concrete plays a crucial role in the corrosion of the reinforcing steel. The ingress of corrosive species, such as chloride ions, oxygen and water, through the pores of the concrete cover cause the breakdown of the passive layer formed on the steel by the high pH of the concrete. The use of supplementary cementitious materials (SCM) in the production of high performance concrete (HPC) improves its resistance to corrosive species as a result of the pozzolanic reaction which forms more calcium silicate hydrates (C-S-H).

Most of the studies about the corrosion of the reinforcement in HPC have been carried out in sound concrete. However, very few works have been reported on the corrosion of steel in cracked concrete. The crack pattern on HPC is very distinct from that formed on ordinary portland cement (OPC) concrete, which may result in different corrosion mechanisms of the reinforcing steel.

The objective of the present work consisted in the evaluation of the corrosion of reinforcing steel in cracked HPC and OPC concrete under different exposure and loading conditions. For that purpose, two sets of beams of HPC (containing fly ash or slag) and two sets of OPC concrete were cast. The difference between the OPC concretes was the date of casting. Three sets of reinforcing steel probes were embedded in each beam at different locations. All the beams were cracked at midspan by the four-point method. Eight beams of each concrete were coupled in pairs and partially immersed in a solution of de-icing salts every two weeks. In this way, one set of the corrosion probes was non-submerged (top) while the other two were completely submerged (one at the crack level and the other at the bottom). Two pairs of beams were subjected to static loading whereas the other two were under cyclic loading.

The corrosion potentials readings were taken daily by a data acquisition system, whereas the corrosion rates were determined by the Linear Polarization technique using a corrosion monitoring system.

According to the results obtained, the corrosion rates of the submerged and non-submerged probes are very low. This behaviour is observed for the four concretes and for both loading conditions. The type of loading did not influence the corrosion rates of these probes, which were in the same range for all the concretes.

On the other hand, the probes close to the crack showed higher corrosion rates, especially those under cyclic loading. In general, the OPC concrete cast during the winter presented the highest corrosion rates for both loading conditions, followed by the OPC concrete cast in the summer (as were both HPCs), then by HPC-Slag and HPC-Fly Ash, which showed the lowest values. In most of the cases there was a good agreement between the corrosion potentials and the corrosion rates, so that the OPC concretes exhibited the most negative values. The lower corrosion of the probes in the HPC-Fly Ash and HPC-Slag beams was ascribed to the continued pozzolanic activity, which may result in the self-healing of the crack with time.

The probes close to the crack in the dynamically loaded beams experienced higher corrosion than those in the static beams. In some cases the corrosion rate reached values above 100 μm/year. The lower corrosion of the probes in the static beams was attributed to the self-healing of the crack. The formation of additional microcracks in the dynamic beams during cyclic loading may be responsible for their higher corrosion.

The corrosion potential of the rebar cage shifted to more negative values during cyclic and static loading. This change in the potential was associated with stress concentration of the reinforcement surface, making it more active. Although the shift in the potential was not really significant, this may have important consequences in practice where the concrete is subjected to higher loads.

Acknowledgments

My special thanks to Professor Carolyn Hansson for her valuable help and who made possible my graduate studies in the University of Waterloo.

My thanks to my co-workers Dr. Laura Mammoliti, Alain Laurent, Samuel Okulaja, Shahzma Jaffer and Amir Poursee for their collaboration during my stay in Waterloo. I also greatly appreciate the assistance of the technical staff in the department of Mechanical Engineering, Andy Barber, Jim Baleshta, John Boldt and Marius Van Reenen, and Richard Morrison from Civil Engineering, who made possible a great deal of the experimental work of this thesis.

I would also like to thanks to my dearest friends Elaine Gonzalez and Humberto Garcia for their moral support and encouragement during all this time.

Financial support was provided by the Cement Association of Canada, Materials and Manufacturing Ontario, and the Natural Sciences and Engineering Research Council of Canada (NSERC).

List of Tables

List of Figures

Introduction

Concrete is generally very resistant to environmental conditions, so that concrete structures are designed to have a long service life. However, many new constructions are showing signs of deterioration long before their expected lifetime and huge investments are made in the rehabilitation and restoration of these structures.

Corrosion of the reinforcing steel is one of the major causes of deterioration of reinforced concrete. Concrete normally protects the reinforcement from corrosion not only by acting as a barrier against corrosive species, but also by forming a passive layer on the steel as a result of the high pH of the solution present in the concrete pores. However, the diffusion of carbon dioxide from the atmosphere and/or chloride ions into the concrete can result in destruction of this passive layer, and hence provoke corrosion of the reinforcing steel. Carbon dioxide reduces the pH of the pore solution, making the passive film unstable and causing generalized corrosion. Chloride ions, on the other hand, locally destroy the passive film provoking localized or pitting corrosion. The corrosion by chlorides is more common, especially in coastal regions and in countries where de-icing salts are used during the winter.

The corrosion of the steel results in the formation of corrosion products, oxides and hydroxides, which have a greater volume than that of the original steel. These corrosion products expand and exert internal stresses in the concrete leading to cracking and spalling of the concrete cover.

The porosity of concrete is the major factor responsible for the degree of protection of the reinforcement by the concrete cover. It is affected by several parameters such as the water/cement ratio and the degree of hydration of the cement paste. The presence of macrocracks and microcracks also significantly enhances the permeability of concrete, so that the aggressive species penetrates easily and accelerate the process of deterioration. Microcracks throughout the concrete can form even before the application of external load. The extension of pores and microcracks present in concrete can be the result of different

causes. Concrete shrinkage, thermal stresses, chemical reactions, poor construction practices and construction overloads are some of the causes of cracks in concrete.

Supplementary cementitious materials, such as fly ash, silica fume and slag, are being extensively used in the production of high performance concrete (HPC). These materials reduce the permeability of concrete by increasing the amount of calcium silicate hydrates (C-S-H), which also lead to the high strength characteristic of HPC. However, HPC is more brittle and more prone to cracking than ordinary portland cement concrete. Moreover, the high reactivity of the cementitious materials, especially silica fume, also leads to the formation of microcracks, thus potentially increasing the permeability of concrete.

The objective of this work consists in the study of the influence of cracks on the corrosion of the reinforcing steel in different concretes exposed to de-icing salts under static and dynamic loading. Ordinary portland cement (OPC) concrete and high performance concretes are studied to determine whether the latter do or do not provide better protection against corrosion when cracks are present.

1. Literature Review

1.1.- Ordinary Portland Cement Concrete.

The main components of ordinary portland cement (OPC) concrete are cement, water and fine and coarse aggregates. Admixtures are also usually used with different purposes, for example, to reduce the water content. Its good resistance to water, low cost and ease of casting in different shapes and sizes at ambient temperature are some of the reasons that make concrete the most extensively used construction material (Hansson 1995).

OPC is made by heating a mixture of limestone and clay, or other materials with similar bulk composition and sufficient reactivity. This results in the formation of the clinker, which is mixed with a few per cent of gypsum ($CaSO_4 \cdot 2H_2O$) and finely ground to make the cement (Neville 1990). The clinker contains four major phases (see Table 1.1 for composition): tricalcium silicate ($3CaO \cdot SiO_2$ or C_3S), dicalcium silicate ($2CaO \cdot SiO_2$ or C_2S), tricalcium aluminate ($3CaO \cdot Al_2O_3$ or C_3A) and tetracalcium aluminoferrite ($4CaO \cdot Al_2O_3 \cdot Fe_2O_3$ or C_4AF). Minor amounts of alkali sulphates and different oxides are normally present in cement clinker (Mehta 1986).

The silicates appear in commercial cements in impure forms as alite (C_3S) and belite (C_2S). Alite is the most important of the constituent phases for strength development, whereas belite contributes little to the strength during the first 28 days, but significantly at later ages (Taylor 1990).

Table 1.1.- Composition of normal portland cement clinkers (Taylor 1990).

Phase	Compound composition
C_3S	50-70%
C_2S	15-30%
C_3A	5-10%
C_4AF	5-15%

The hydration of OPC results in the formation of calcium silicate hydrates (C-S-H) and calcium aluminate hydrates. The former are mainly responsible for the adhesive properties of cement, whereas the latter are related to setting of cement. Calcium hydroxide ($Ca(OH)_2$ or CH) is also formed on the hydration of silicates according to the following reactions (Mindess and Young 1986; Neville 1990):

$$2(3CaO{\cdot}SiO_2) + 6H_2O \rightarrow 3CaO{\cdot}2SiO_2{\cdot}3H_2O + 3Ca(OH)_2 \quad (1.1)$$

$$2(2CaO{\cdot}SiO_2) + 4H_2O \rightarrow 3CaO{\cdot}2SiO_2{\cdot}3H_2O + Ca(OH)_2 \quad (1.2)$$

The C-S-H phase makes up to 50 to 60% of the volume of solids in a completely hydrated OPC paste, while calcium hydroxide constitutes 20 to 25% (Mehta and Monteiro 1993). Some of the CH reacts with sodium and potassium salts present in cement to form soluble hydroxides, responsible for the high pH of the solution in the pores of the cement paste, typically >13.

The hydration of calcium aluminates can result in the formation of ettringite according to the following reaction (Mehta 1986):

$$3CaO{\cdot}Al_2O_3 + 3CaSO_4{\cdot}2H_2O + 26H_2O \rightarrow 3CaO{\cdot}Al_2O_3{\cdot}3CaSO_4{\cdot}32H_2O \quad (1.3)$$

The precipitation of ettringite contributes stiffening, setting, and early strength development. However, after depletion of sulphate in the solution when the aluminate concentration in solution goes up again due to renewed hydration of C_3A and C_4AF, ettringite becomes unstable and is converted to monosulphate. The proposed reaction is as follows (Mindess and Young, 1981; Kuzel, 1996):

$$2CaO{\cdot}Al_2O_3 + 3CaO{\cdot}Al_2O_3{\cdot}3CaSO_4{\cdot}32H_2O + 4H_2O \rightarrow 3(3CaO{\cdot}Al_2O_3{\cdot}CaSO_4{\cdot}12H_2O) \quad (1.4)$$

Ettringite is the first compound to form, and after few hours CH and the calcium silicate hydrates, which begin to fill the empty space formerly occupied by water and the dissolving cement particles (Mehta 1986). The space not filled by hydration products consists of capillary

pores, the volume and interconnectivity of which are mainly determined by the water/cement ratio and degree of hydration. Capillary pores larger than 50 nm are known as macropores, and those smaller than 50 nm as micropores. Macropores play an important role on the strength and permeability of concrete, while micropores seems to affect shrinkage and creep (Mehta and Monteiro 1993). A high permeability will affect the durability of concrete by allowing the ingress into concrete of aggressive species such as chloride ions, carbon dioxide and sulphate compounds.

Another group of pores in the ranges of 0.5-2.5 nm, known as gel pores, represents the interlayer space within the C-S-H structure and account for ~28% porosity in solid C-S-H (Neville 1990). According to Mehta (1986) these pores are too small to have an adverse affect on the strength and permeability of the cement paste, but may contribute to drying shrinkage and creep.

1.2.- High Performance Concrete: Supplementary Cementitious materials.

High Performance Concrete (HPC) meets special combinations of performance requirements, such as workability and strength development, that cannot always be attained using conventional materials and normal mixing, placing and curing practices (Kosmatka et al. 2002). The use of low water/cement ratios in HPC results in a low-permeability concrete with generally higher strength (40-140 MPa at 28 to 91 days) and durability than OPC concrete. However, HPC is generally more brittle than OPC concrete.

The water/cement ratio of HPC range from 0.20 to 0.45. Such a low ratio requires the use of plasticizers, which increases the plasticity of the concrete making the concrete fluid and workable.

Supplementary cementitious materials (SCM) such as silica fume (SF), fly ash (FA) and slag are used extensively in construction as a partial replacement of some of the concrete

constituents, but mainly of OPC. One of the main uses of these materials has been in HPC, since they enhance some of the properties of fresh and hardened concrete. For example, they improve the resistance to cracking and reduce the expansion due to reactive aggregates (ACI-224 2001; Sioulas and Sanjayan 2000). They also improve the rheology of fresh concrete. These materials are by-products of different industries, so that their uses also lead to ecological and economic benefits.

1.2.1.- Fly Ash

Fly ash is the residue of the combustion of pulverized coal in electric power plants. Fly ashes are generally divided in Class F for low calcium content (≤ 8% CaO), and Type C for high calcium content (≥ 8% CaO). This difference in composition influences significantly the behaviour of concrete. High calcium fly ashes generally react faster than low calcium fly ashes and have less effect on the early strength of concrete (Thomas et al. 1999). In general, low calcium fly ashes retard the setting of cement, while high-calcium fly ashes have given different results (Malhotra and Ramezanianpour 1994). The use of FA allows a reduction of the water requirement for given slump, and improves the workability by increasing the paste volume (Malhotra and Ramezanianpour 1994).

It has been reported that the compressive strength development of concretes prepared from FA is slower than concrete prepared from OPC, but it increases at later ages of curing (Thomas et al. 1999; Papadakis 1999). However, according to Malhotra and Ramezanianpour (1994), this is not always true because of the influence of other concrete components.

The slower development of the early strength is attributed to the slow pozzolanic reaction between FA and CH produced during portland cement hydration (Lee and Lee 1997). The product of this reaction is C-S-H, and the reaction continues as long as calcium and hydroxyl ions are available (Taylor 1997). According to Leng et al. (2000), FA and blast furnace slag may improve the distribution of pore size and pore shape of concrete. The formation of additional C-S-H phases and the disruption of the continuity of the pore system by reaction

products increase the resistance of HPC to fluid flow and ionic diffusion (Schießl and Wiens 1997; Thomas et al. 1999). In this way, FA concretes provide a better protection to steel than OPC concrete. The addition of FA also increases the resistance to sulphate attack due to the reduction of C_3A (Mehta and Monteiro 1993).

Although FA can reduce the pH as a result of its reaction with CH, which together with NaOH and KOH is responsible for the formation of a passive film on the steel, it is generally agreed that FA can reduce corrosion. The reduction of the pH is limited to a level above 12.5, at which the passive film is still stable.

1.2.2.- Slag

Slag is one of the by-products of steel production. Concretes prepared from slag also have significantly lower permeability, which results in a highly durable concrete. A significant reduction of chloride permeability and penetrability with increasing slag replacement has been obtained (Aldea et al. 2000). The addition of slag also reduces the pore diameter (Aldea et al. 2000; Osborne 1999) and the water requirement to obtain a given consistency (Swamy 1997). Generally, it is reported an improvement of the pore structure of OPC and a decrease of the chloride diffusion coefficient with the addition of slag. Osborne (1999) states that slag increases resistance to sulphate attack and alkali silica reaction. This same author points out the importance of a good early curing to minimize the effects of higher rates of carbonation, surface scaling and frost attack.

Chemical compounds similar to C-S-H form during the pozzolanic reaction of slag, causing pore refinement (Jaul and Tsay 1998). It has been found that slag is better than FA in pore refinement (Swamy 1997). Slag seems to be more efficient in blocking the pores since it reacts not only with $Ca(OH)_2$ but also with water to form C-S-H and calciumaluminates, whereas Fly ash reacts only with $Ca(OH)_2$ (Bakker 1983). Chloride ions may be trapped or bound by some of the components of concrete. Thus, the additional formation of C-S-H gel result in the absorption of more chloride ions and blocking of diffusing paths. A higher content of C_3A in

slag and FA can also absorb more chlorides to form Friedel's salt (Leng et al. 2000). However, the chloride-binding capability of slag can be reduced in the presence of sulphates (Luoa et al. 2003; Leng et al. 2000).

Thus, slag not only decreases the permeability of concrete, but also decreases the free chloride and increases the bound chloride content in concrete (Mohammed and Hamada 2003), which result in a lower probability of corrosion of the reinforcing steel. A decrease of corrosion rates and pitting corrosion of steel in concrete with 30% slag and exposed to sodium chloride (NaCl) solutions has been observed (Dehghanian 1999). Other authors have found that concrete with 20–30% substitution has the best corrosion resistance (Jaul and Tsay 1998).

A negative effect of slag is, as in the case of FA, the slower compressive strength development than concrete prepared from OPC (Khatri et al. 1995). Slow strength development has been associated to the slow hydration rate of SCM in the alkaline solution, which is controlled by dissolution and diffusion processes (Khatri et al. 1995). It has been reported that slag replacement up to 50% has little effect on strength, whereas higher replacement results in a drop of the compressive strength (Aldea et al. 2000).

Slag replacement can also reduce the hydration temperatures, which is an issue of concern in concrete with high cement contents and massive structures (Sioulas and Sanjayan 2000; Osborne 1999).

1.2.3.- Silica Fume

Silica fume is a by-product of the induction arc furnaces in the silicon metal and ferrosilicon alloy industries. Silica fume samples show particle size distributions (0.1 μm average) that are two orders of magnitude finer than FA (typically under 20 μm), slag (under 45 μm) and OPC (typically under 45 μm; average around 15 μm) (Kosmatka et al. 2002). This explains why SF is highly pozzolanic, but reduces workability and increases water requirements (Taylor 1997). As a result, SF starts to contribute to the strength development as early as one day after mixing

of concrete, whereas slag takes more than three days and FA takes more than seven to fourteen days before it makes any significant contribution to the development of strength of concrete (Khatri et al. 1995).

It has been reported that the addition of SF decreases the setting times but the compressive strength is improved at all ages (Khatri et al. 1995; Thomas et al. 1999). However, according to Thomas et al. (1999), much of the increase occurs at early ages and the rate of strength development at later ages is similar for SF concrete and OPC concrete.

Several authors agree that the addition of SF to concrete improves the durability of concrete by reducing the overall capillary porosity, leading to a reduction in the ingress of harmful ions (Babu and Prakash 1995; Li and Chung 1998). The reaction of SF with the CH present in the transition zone, makes this zone dense and uniform (Vivekanandam 1997; Bentz 2000) and without crystalline CH (Mehta 1986). According to Mehta (1986) microcracks in this zone is the major location of concrete permeability in OPC concretes, whereas a relatively discontinuous system of fine pores exists in hydrated cement pastes containing SF. The reduction of the CH content by the pozzolanic reaction also results in a higher resistance to sulphate attack and alkali-silica reaction (Babu and Prakash 1995). This may be due to a decrease in the porosity of concrete. It has been also stated that the C-S-H gel produced by the pozzolanic reaction has a much lower relative diffusivity than that of the C-S-H gel produced from conventional cement hydration (Bentz 2000).

The decrease in permeability will also improve the ability of SF concrete to protect the embedded steel from corrosion (Babu and Prakash 1995). Silica fume also enhances electrical resistivity of concrete (Mehta 1986), so that the corrosion rate is reduced. An increase of the bond strength with the reinforcing steel has also been reported (Li and Chung 1998).

1.2.4.- Combination of pozzolans

According to Lilkov et al. (1997), the problem of low early-age strength can be overcome by using both FA and SF. This was confirmed by Thomas et al. (1999), who concluded that the combination of SF and low calcium FA is complementary, resulting in concrete with improved early age and long-term strength development, superior to OPC concrete. In their opinion, the deficiency of high calcium FA as regard sulphate resistance can be compensated for by the addition of small quantities of SF (Thomas et al. 1999). However, Khatri et al. (1995) reported a decrease in the early age strength with the inclusion of low calcium FA into concrete containing OPC and SF, whereas the strain due to drying shrinkage and creep increased.

Turkmen et al. (2003) reported that the addition of 10% SF and 40% slag causes a reduction of the corrosion of reinforcing steel in concrete exposed to 5% NaCl solution. It has been found that the use in high-performance concretes of triple blends of either a slag or a silica fume added to the FA/OPC system could further enhance the chloride resistance of the concretes (Sirivivatnanon and Kidav 1997) and decrease permeability and corrosion (Lilkov et al. 1997).

Mehta (1986) reports that the threshold pore diameter (the minimum pore diameter in a solid at which a continuous pore system exists) decreases in the following order: OPC > [OPC + FA] > [OPC + SF + FA] > [OPC + SF]. Comparisons with slag combinations were not found in the literature.

1.3.- Causes of cracking of concrete

The extension of pores and microcracks present in concrete can be the result of different causes (Mehta 1986). The durability of concrete structures is commonly affected by the formation and growth (initiation and propagation) of cracks, which are related to other causes of concrete deterioration. Concrete shrinkage, thermal stresses, chemical reactions, poor

construction practices and construction overloads are some of the causes of cracks in concrete (ACI-224 2001).

The formation of cracks increases the permeability of concrete, so that the aggressive species penetrates easily in the interior and accelerate the process of deterioration. In this way, cracks favour the development of corrosion, and in turn, corrosion provokes more cracking and eventually the deterioration of concrete (Mehta 1986).

Cracks range from very small internal microcracks that occur on the application of modest amounts of stress, through to quite large cracks caused by undesirable interactions with the environment (Mindess and Young 1981). Their significance depends on the type of structure, as well as the nature of the cracking (ACI-224 2001). Microcracks throughout the concrete can form even before the application of external load (Mehta 1986). The interface zone between the cement paste and the aggregates is considered the weakest element in normal concrete, so that it plays an important part in crack initiation and propagation (Chiaia et al. 1998). This zone together with other micro defects form the nucleus for successive macrocrack growth.

In concrete with silica fume, the cracks usually travel through the aggregate and fracture tends to be brittle in nature. In concretes without silica fume, the cracks usually develop around the coarse aggregate resulting in a more tortuous fracture path. This different cracks pattern can be attributed to the interfacial zone becoming stronger and more homogeneous, as a result of silica fume inclusion, and the material exhibits a more brittle behaviour and transgranular type of fracture (Tasdemir et al. 1996).

1.3.1.- Effect of loading

Microcracks increase under the effect of sustained and cyclic loading. A significant part of the bond cracking under these two forms of loading results from volume changes within the paste, but the effect on strength is negligible (ACI-224 2001). However, it is not entirely clear

whether mortar cracking itself controls the concrete strength or whether it only indicates damage of the cement paste (ACI-224 2001).

Fracture under cyclic loading, i.e. fatigue fracture, shows larger strains and microcracking compared to fracture of concrete under static loading. Fatigue failure is characterized by progressive and permanent internal damage, as a result of the propagation and growth of internal microcracks (Kim and Kim 1999).

The growth rate of cracks is considerably faster, and hence concrete deteriorates more rapidly under cyclic loading than under sustained loading (Ahn and Reddy 2001). It has been observed that, under sustained loading, cracks grow in width at a decreasing rate (ACI-224 2001). According to Kim and Kim (1999) the crack growth rate under cyclic loading increases with the strength of concrete, so that the fatigue life of lower-strength concrete should be longer than that of higher-strength concrete.

The development of a connected crack network also contributes to increase the permeability and diffusivity of concrete, and therefore the corrosion of the reinforcing steel. Microcracking due to mechanical loading increases the ingress of aggressive species from outside to the reinforcement, leading to the propagation of steel corrosion (Castel et al. 1999). Saito and Ishimori (1995) also found that compressive static loading had a little effect on the permeability of normal concrete, whereas under cyclic loading increased significantly. Other results show that the load applied to a reinforced concrete beam and its intensity play a significant role in the penetration of the CO_2 as a result of the increase of the tensile concrete microcracking mainly located at the paste-aggregate interface (Castel et al. 1999).

Ahn and Reddy (2001) obtained more and longer cracks induced by corrosion on beams exposed to simulated marine environment and less ultimate strength under cyclic loading than under static loading.

1.4.- Corrosion of reinforcing steel in concrete

Whereas the reinforcing steel enhances the tensile strength and toughness of concrete, a good quality concrete acts in turn as a physical barrier to corrosive species protecting the steel from corrosion. In addition, the high alkalinity (pH 12.5-13.8) of the pore solution in concrete, due to the presence of hydroxides such as NaOH, KOH and $Ca(OH)_2$ produced during the hydration of cement, results in the formation of a protective passive layer on the steel that reduces significantly the corrosion rate. This can be observed in the Potential-pH diagrams, also known as Pourbaix diagrams, where different regions are identified according to the corrosion product formed and its corrosion protection properties (see Figures 1.1 and 1.2).

However, the penetration of carbon dioxide or depassivating anions such as chloride can destroy the passive layer and cause severe corrosion of the reinforcement in the presence of moisture and oxygen (see Figure 1.2). The degree of protection of steel by concrete is mainly a function of the porosity and cracks of the hydrated cement paste. Although pores are intrinsic to concrete, they can also result from high water/cement ratios and inadequate compaction. The presence of microcracks also enhances the diffusion of corrosive agents.

The corrosion of the reinforcement results in the formation of expansive products (such as $Fe(OH)_2$, Fe_3O_4 and Fe_2O_3) with a volume greater than iron, which generate internal stresses and subsequent cracking and spalling of concrete (Hansson 1995). Corrosion is considered to be the major cause of deterioration of reinforced concrete structures.

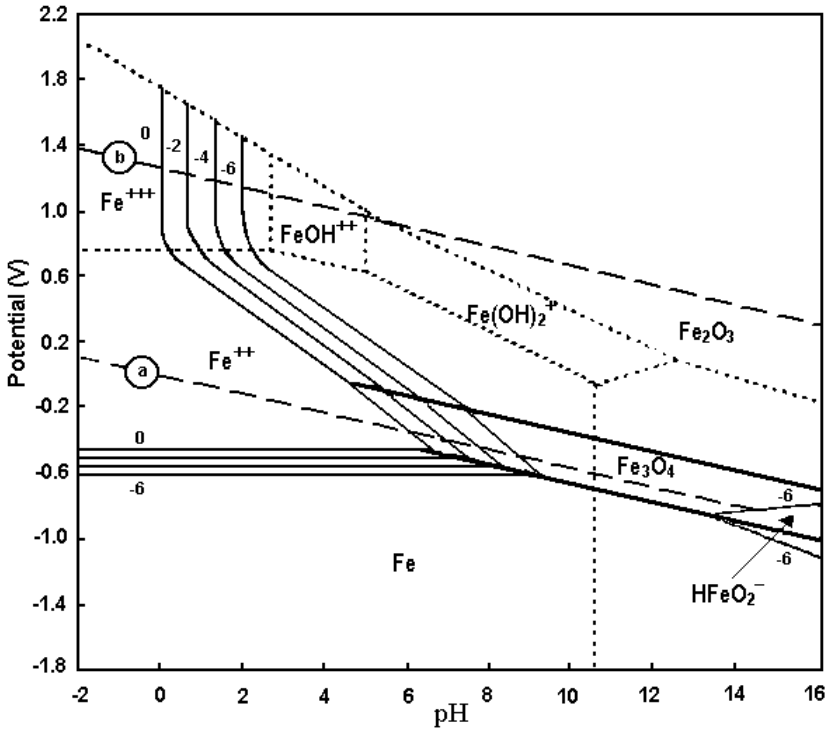

Figure 1.1.- Potential-pH potential for iron at 25 ^{o}C (Pourbaix, 1974).

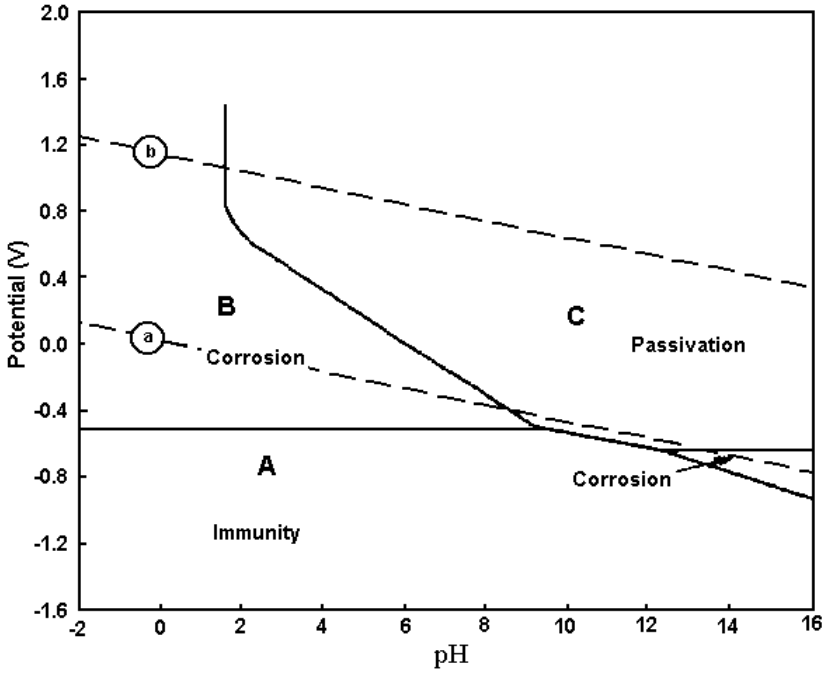

Figure 1.2.- Potential-pH potential for iron at 25 ^{o}C. Thermodynamic conditions of iron in water (Pourbaix, 1974).

During corrosion an electrochemical cell is formed and the anode and the cathode may be located on the same rebar. The rebar also serves as the electronic conductor, whereas the concrete acts as the ionic conductor or electrolyte, as shown in Figure 1.3.

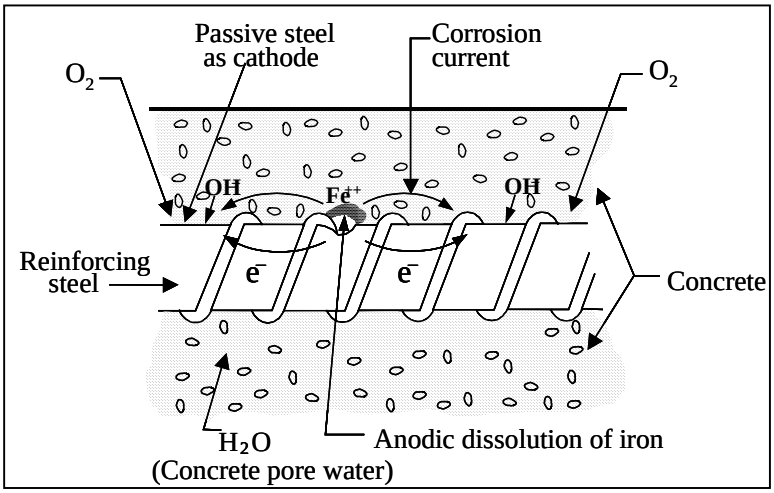

Figure 1.3.- Scheme of the corrosion process of reinforcing steel in concrete (Ahmad 2003).

Depending on the pH of the electrolyte, the presence of aggressive anions, and the existence of an appropriate electrochemical potential at the steel surface, the corrosion of steel embedded in concrete will proceeds according to the following possible anodic reactions (Hansson 1984; Ahmad 2003):

$$Fe \rightarrow Fe^{2+} + 2e^- \quad (1.5)$$

$$3Fe + 4H_2O \rightarrow Fe_3O_4 + 8H^+ + 8e^- \quad (1.6)$$

$$2Fe + 3H_2O \rightarrow Fe_2O_3 + 6H^+ + 6e^- \quad (1.7)$$

$$Fe + 2H_2O \rightarrow HFeO_2^- + 3H^+ + 2e^- \quad (1.8)$$

The availability of O_2 and the pH in the vicinity of the steel surface will determine the possible cathodic reactions. The most likely reactions are as follows (Hansson 1984; Ahmad 2003):

$$O_2 + 2H_2O + 4e^- \rightarrow 4OH^- \quad (1.9)$$

or

$$2H^+ + 2e^- \rightarrow H_2 \quad (1.10)$$

As mentioned before, chloride ions are one of the most important causes for corrosion of the reinforcing steel. Whereas corrosion of the reinforcement occurs uniformly in the presence of carbon dioxide, the chlorides cause localized corrosion as a result of the breakdown of the passive layer. The structural integrity of the structure is significantly reduced because of the very aggressive and local damaging effect of chlorides.

Chloride ions may be added during mixing either deliberately as an admixture or as a contaminant in the original constituents, or may enter the set concrete from an external source such as seawater and de-icing salts. However, corrosion will only occur in the presence of oxygen and moisture in the steel-concrete interface, and when the chlorides reach the steel and a certain concentration level needed to destroy the protective film. This threshold concentration depends on several factors, such as concrete mix proportions, type of cement, C_3A content, water/cement ratio, temperature, relative humidity, steel surface conditions and source of chloride penetration among others. Chlorides in concrete can be either dissolved in the pore solution (free chlorides), or chemically and physically bound to the cement hydrates (bound chlorides), but only the free chlorides are responsible for the corrosion of the reinforcing steel (Martinez-Perez 2000).

There are three theories about the mechanism of chloride attack (ACI-222, 2001): one theory postulates that “chloride ions penetrate the oxide film on steel through pores or defects in the film easier than do other ions”; in the second theory is stated that “chloride ions are adsorbed on the metal surface in competition with dissolved O_2 or hydroxyl ions”; and the third one

claims that “chloride ions compete with hydroxyl ions for the ferrous ions produced by corrosion and a soluble complex of iron chloride forms which can diffuse away from the anode destroying the protective layer of $Fe(OH)_2$ permitting corrosion to continue”. For this reason chloride-induced corrosion is considered to be the more severe process as the chlorides are not consumed, but act as a catalyst.

1.4.1.- Evaluation of corrosion activity in concrete.

1.4.1.1.- Corrosion Potential

The measurement of the corrosion potential (E_{corr}) with respect to a reference electrode is the simplest measurement in a corrosion system. This can be done simply by using a voltmeter. According to ASTM Standard C876-91 (ASTM 1991), the corrosion potential measured against the copper sulphate electrode (CSE) can give an indication of the probability of the occurrence of active corrosion, as it is shown in Table 1.2.

Table 1.2.- Probability of corrosion according to ASTM standard C876-91.

E_{corr} (V vs. CSE)	Probability of corrosion
More negative than –0.350	90%
More positive than –0.200	10%
Between –0.200 and –0.350	Uncertain

1.4.1.2.- Linear Polarization Resistance

Corrosion is an electrochemical process so that it can be studied by using electrochemical techniques. The Linear Polarization Resistance (LPR) technique, introduced by Stern and Geary (1957), is the most popular method for the evaluation of the corrosion rate, and many field applications are based on this technique. This popularity lies on its simplicity and speed of the measurement. In general, a three electrode configuration is used to determine the polarization resistance, R_p, and hence the corrosion rate. This configuration consists of a working electrode (metal of interest), a counter electrode to apply the current, and a reference electrode to control the voltage, which normally is a standard reference electrode, such as copper-copper sulphate or saturated calomel or a metal that does not corrode during the test.

A polarization resistance measurement is performed by scanning through a potential range of ± 20 mV about E_{corr}. In this potential range an approximate linear relationship exists between the current and the potential. The slope of this line corresponds to the polarization resistance:

$$R_p = \Delta E/\Delta I \qquad (1.11)$$

R_p = polarization resistance (Ω)

ΔE = potential gradient (V)

ΔI = current gradient (A)

The corrosion current, I_{corr}, which is a measured of the anodic and cathodic reactions, i.e. the flow of electrons from the anodic to the cathodic site, is related to R_p through the following equations (Stern and Geary 1957):

$$I_{corr} = R_p/B \qquad (1.12)$$

$$B = \frac{\beta_a \beta_c}{2.3(\beta_a + \beta_c)} \quad (1.13)$$

where:

B = constant (V);

β_a = slope of the anodic Tafel plot;

β_c = slope of the cathodic Tafel plot.

The anodic and cathodic Tafel plots (Potential versus logarithm of the current) are determined by polarizing the electrode from the corrosion potential in the anodic and cathodic directions, respectively. However, in general these constants are assumed, so that B takes a value of 0.026 V or 0.052 V when the metal is passive or active, respectively (Andrade and Gonzalez 1978).

The corrosion current is in turn related to the mass that reacts during the corrosion process through the Faraday's law:

$$m = I_{corr} W t / nF \quad (1.14)$$

m = mass (g)

W = atomic weight (g/mol)

n = number of equivalents

t = time (seconds)

F = Faraday's constant (96, 500 coulombs/equivalent)

Dividing Equation 1.14 by time, iron density (ρ) and the corroding area (A) the corrosion rate can be determined through the following relationship:

$$r = 1.16 \times 10^3 \, i_{corr} \quad (1.15)$$

where r is the corrosion rate (μm/year) and i_{corr} is the corrosion current density (A/m^2).

Some researchers have concluded that corrosion rates below ~1 μm/yr (0.1 μA/cm^2) are characteristics of passive systems, whereas over ~10 μm/yr (1 μA/cm^2) are characteristics of systems with high corrosion (Gonzalez et al. 1995; Polder and Peelen 2002; Alonso et al. 2002). However, some precautions may be taken in the interpretation of these values, since they were obtained with a piece of equipment that generally gives lower values than other commercial corrosion rate meters (Hansson, 2003).

1.4.1.3.- Electrochemical Noise

Electrochemical noise (EN) refers to the spontaneous fluctuations in potential (electrochemical potential noise, EPN) that can be observed on a corroding metal (electrode) and/or the spontaneous fluctuations in current (electrochemical current noise, ECN) when the electrode is externally polarized, either by a potentiostat or by another electrode (Lowea et al. 2003). These fluctuations can be measured in freely corroding systems; therefore the characteristics of electrochemical noise are influenced only by the type and rate of corrosion. However, the major advantage of Electrochemical Noise consists in the fact that the electrode does not need to be polarized, consequently the corrosion processes are not disturbed by any external voltage or current. The electrochemical cell generally consists of two identical electrodes, although a reference electrode can also be used.

The measurement of these fluctuations results in a time series which can be observed in real time and detect any burst or spike on the current or the potential, as indication of corrosion onset. The EN data is commonly processed by statistical analysis or by spectral analysis using the Fast Fourier Transform (FFT) or the Maximum Entropy Method (MEM). The spectral analysis of electrochemical noise in the frequency domain achieves good correlation with corrosion rate and type, i.e. localized, uniform or passivation (Legat and Govekar 1994).

In the statistical analysis, the standard deviations of the two time series and their ratios are calculated. From this ratio is possible to determine the noise resistance, R_n, and hence to

calculate the corrosion rate according to Equation 1.12. Thus, R_n is determined by using the following relationship:

$$R_n = \sigma V/\sigma I \qquad (1.16)$$

where:

R_n = Noise Resistance, Ω.

σV = Standard Deviation of Potential, V.

σI = Standard Deviation of Current, A.

1.4.1.4.- Electrochemical Impedance Spectroscopy

Electrochemical Impedance Spectroscopy (EIS) is another technique commonly used to study corrosion. Electrochemical impedance is measured by applying an AC voltage to the corrosion cell, instead of a DC voltage as in the case of LPR. In this way, the impedance, Z, and the phase angle between Z and the applied potential are determined over a wide range of frequencies (Stansbury and Buchanan 2000). The amplitude of the excitation is usually very small (around 10 mV), so that the perturbation of the corrosion system under study is minimal.

The main advantage of this technique consists in the fact that the corrosion system can be represented by an equivalent circuit such as the one shown in Figure 1.4 (Montemor et al. 2003). This allows a better characterization of the corrosion system, including the determination of the solution resistance (R_e), the capacitance of the double layer (C_d) among others.

The EIS data is normally plotted in different formats. The most common plot is the Nyquist plot (Figure 1.5) where the imaginary impedance component, Z_{im}, is plotted against the real impedance component, Z_{real}. Another frequently used format is the Bode plot (Figure 1.6), where the logarithm of the absolute impedance is plotted against the logarithm of the angular frequency (ω). Figures 1.5 and 1.6 are the corresponding plots for the equivalent circuit

shown in Figure 1.4. As can be seen, from these diagrams it is possible to determine R_e and R_p, the latter being used to evaluate the corrosion rate by using Equation 1.12. Several equivalent circuits have been proposed in the literature for modelling the steel-concrete interface (Figure 1.7). Figures 1.8 and 1.9 show the Nyquist and Bode plots for the equivalent circuit (E), where the Warburg impedance (W) is included. The Warburg impedance represents a resistance to mass transport.

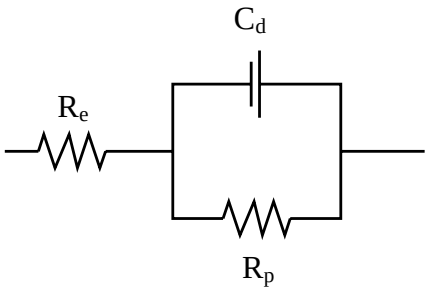

Figure 1.4.- Equivalent circuit for a simple corrosion system.

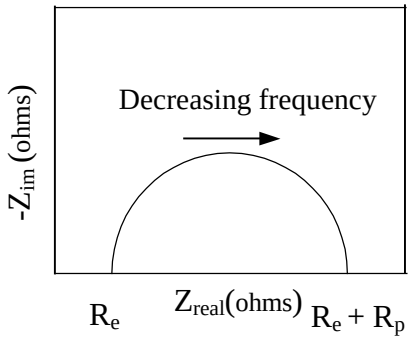

Figure 1.5.- Nyquist plot for a simple corrosion system. R_e electrolyte resistance, R_p charge polarization resistance, C_d double layer capacitance.

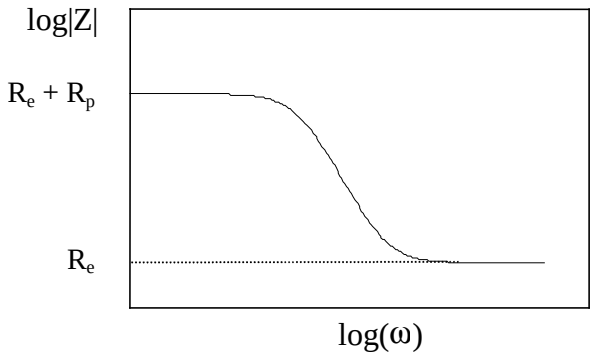

Figure 1.6.- Bode plot for a simple corrosion system.

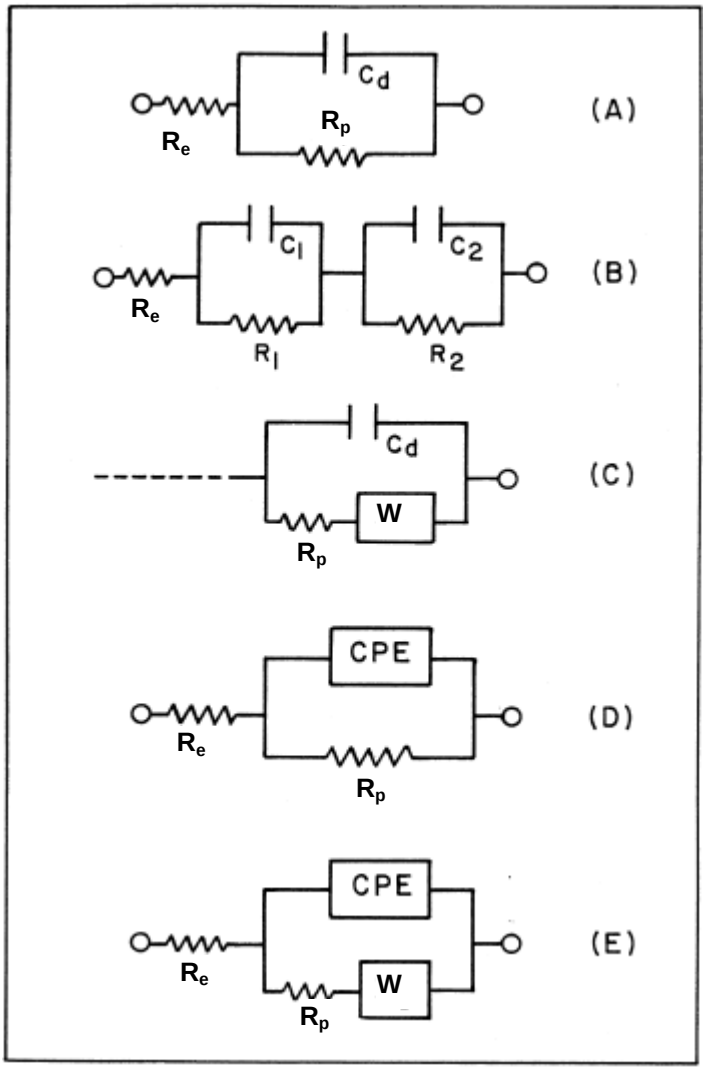

Figure 1.7.- Equivalent circuits for modelling the steel-concrete interface. R_0 undefined resistance, C_0 undefined capacitance, CPE constant phase element, W Warburg Impedance (Feliu et al. 1998).

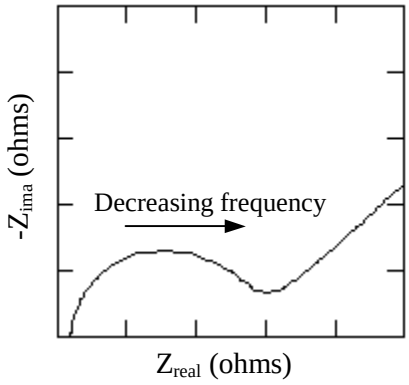

Figure 1.8.- Nyquist plot showing diffusion control at low frequencies.

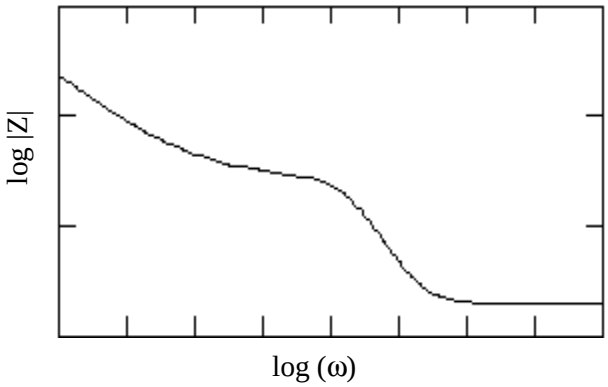

Figure 1.9.- Bode plot showing diffusion control at low frequencies.

2. Experimental Procedures

2.1.- Materials

Type 10 ordinary portland cement (OPC) and Type 10E SF cement, which contains 9% Silica Fume, were used to cast four different groups of concrete specimens. Partial replacements of Type 10E SF cement by 25% (by weight) of fly ash or slag were made to cast two sets of High Performance concrete (HPC). Table 2.1 shows the chemical analyses of cements, FA and slag used for each type of concrete. The concrete mixture proportions for producing 1 m^3 of concrete are reported in Table 2.2.

Table 2.1.- Chemical analysis of cements used for each type of concrete. OPC-TC for concrete cast in February 2001 and OPC-C for concrete cast in May 2001.

	OPC-TC	OPC-C	Type 10E SF	Fly ash	Slag
Loss on Ignition	2.17	2.24	1.94	0.28	0.68
SiO_2	19.57	19.40	25.23	34	39.93
Al_2O_3	5.20	5.20	5.38	19	8.67
Fe_2O_3	2.39	2.35	2.21	5.7	0.57
CaO	62.07	62.20	57.85	18	37.69
MgO	2.47	2.50	2.26	3.8	10.35
SO_3	4.08	4.03	3.56	4.2	2.72
Free Lime	1.54	1.40	1.21	–	–
Na_2O	0.25	0.30	0.29	0.7	0.30
K_2O	1.11	1.11	1.07	0.7	0.45
Alkalis (Na_2O equivalent)	0.98	1.03	0.99	0.72	–
Insoluble residue	0.43	0.29	–	–	–
C_3S	53.92	55.97	3.23	–	–
C_2S	15.44	13.40	74.76	–	–
C_3A	9.75	9.82	9.54	–	–
C_4AF	7.27	7.14	6.73	–	–

Table 2.2.- Concrete mixture proportions for producing 1 m^3 of concrete.

Component	OPC concrete	HPC-Fly Ash	HPC-Slag
Type 10 Portland, kg	355	–	–
Type 10SF Portland, kg	–	337	337
Slag, kg	–	–	113
Fly ash, kg	–	113	–
Sand, kg	770	718	718
Stone 20 mm, kg	1070	1065	1065
Water, L	153	158	158
Eucon MRC air entrainment	40ml/100kg cementitious	65ml/100kg cementitious	65ml/100kg cementitious
Water reducer	250 ml/100kg cementitious	250 ml/100kg cementitious	250 ml/100kg cementitious
Superplasticizer	–	3.5 L	3.5 L
water/cement ratio	0.43	0.35	0.35

2.2.- Design of concrete specimens

The beams (1200×150×130 mm) were made with reinforcement cages consisting of two longitudinal carbon steel (10M) reinforcing bars, two longitudinal stainless steel (316L) rebars, and 14 stirrups of stainless steel (316L). Two electric wires were attached to two stirrups, each one located at the extremes of the beam. The rebars were placed at 36 mm from the wall of the formwork and separated 40 mm from each other. Two plastic tube sections were placed at both ends to allow coupling the beams in pairs. A manganese/manganese oxide (Mn/MnO_2) embeddable reference electrode (ERE) was also fixed in one beam from each type of concrete to measure the corrosion potential. Figure 2.1 shows a photograph of the reinforcement cages in the formwork and Figure A.1 of Appendix shows a diagram with the dimensions of the different sections of the beam. This design was made by former graduate student Oliver Gepraegs.

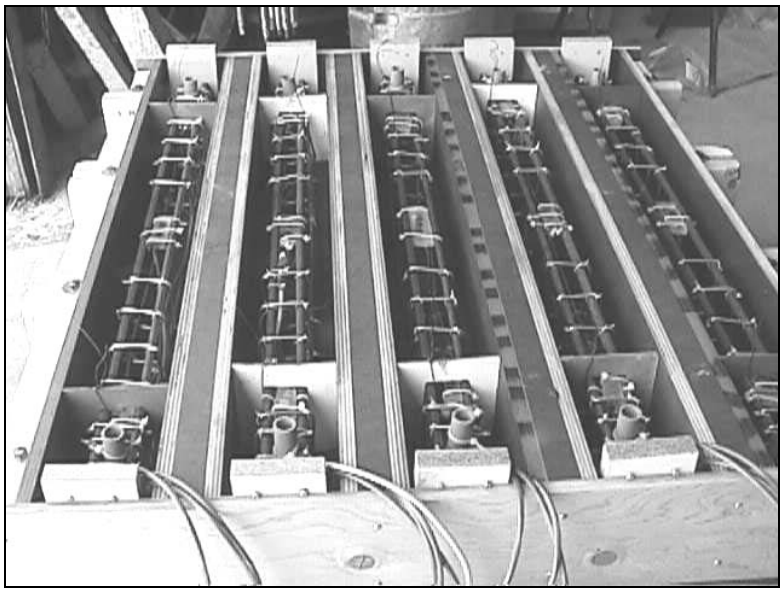

Figure 2.1.- Framework for concrete beams.

2.3.- Design of Reinforcing Steel Probes

Three sets of corrosion probes, shown in Figure 2.2, were embedded in each beam, one set at each end and one in the middle for monitoring their corrosion behaviour. Each set consisted of three small sections (3.5-4.5 mm long - height) of reinforcing bar 10M and one 10 mm diameter section of stainless steel 316L of around 3 mm long. These pieces were individually wired to one of their transversal sections and embedded separately in epoxy resin, leaving the other section exposed. The exposed section was polished to remove any possible remainder of epoxy and to smooth the metal surface. In this way the metal surfaces would be in direct contact with concrete. The three sets of probes were tied with straps to the carbon steel reinforcement as shown in Figure 2.2. A diagram of the corrosion probe set and the wire connections are shown in Figures A.2 and A.3 of the Appendix.

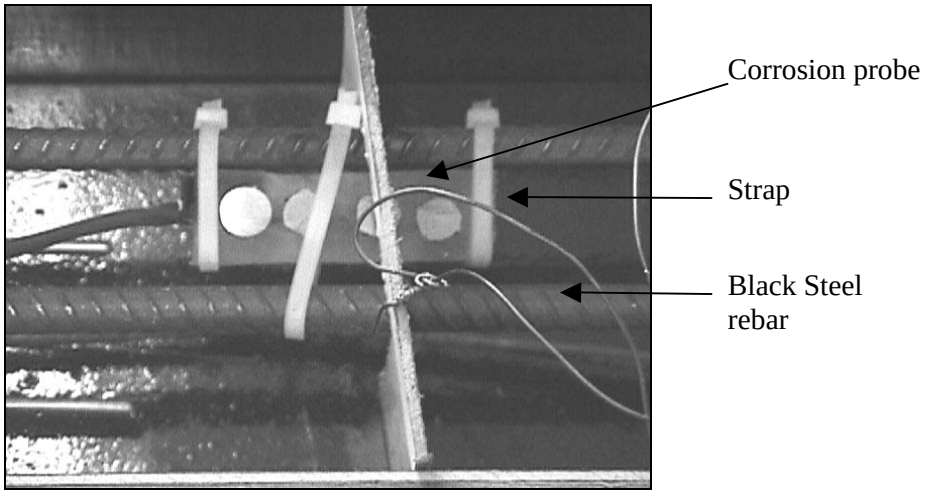

Figure 2.2.- Set of corrosion probes attached to the rebar.

3.4.- Casting and curing of specimens

Two sets of OPC concrete and two of HPC were cast for a total of 40 specimens. All the beams were cast by the Corrosion Group before starting this project. One set of OPC concrete was cast during the winter and all other concretes were cast during the summer (see Table 2.3). This difference in casting date allows studying the effect of freeze/thaw cycles during curing on the corrosion behaviour of OPC concrete. HPC beams were prepared according to the specifications of the Ministry of Transportation of Ontario (MTO 1999). All the beams were cured under wet burlap and plastic, but whereas the HPC beams were cured for seven days, the OPC concrete beams were cured for only two days. Afterwards, they were kept outdoors until October when the beams were loaded to cracking and set for corrosion tests.

Cylinders of 100 mm in diameter by 200 mm in height were also cast for each type of concrete and kept in the fog room for compression tests. The compressive strengths for OPC-C and HPC after 28 and 56 days are reported in Table 2.4.

Table 2.3.- Dates of casting the different types of concrete.

Type of concrete	Date of casting
OPC concrete TC	February 1, 2001
OPC concrete C	May 29, 2001
HPC with Fly ash	June 5, 2001
HPC with slag	June 5, 2001

Table 2.4.- Compressive strengths (MPa) of the concrete mixes.

Age, days	OPC-C	HPC-Fly Ash	HPC-Slag
28	27.2	51.1	49.2
56	42.2	55.4	51.6

2.5.- Induced cracking

The beams were pre-cracked at midspan (along the 130 mm side) by the four-point bending method on a computer-controlled press. The purpose of the crack is to study its effect on the development of the corrosion process. A strain gauge consisting of a linear variable differential transformer (LVDT) was placed on one side of the beam to monitor the strain at cracking and the displacement. The LVDT gauge was attached by magnets to two small metallic pieces glued with epoxy to the beams around the crack region. A crack comparator was used to measure the crack width, which was expected to be around 0.3 mm under loading. As Figure 2.3 shows, the crack extends perpendicularly to the reinforcement around the half of the 150 mm dimension. In the case of one OPC-C beam (C10) two cracks were accidentally induced during cracking.

Figure 2.3.- Concrete specimen after inducing cracking.

2.6.- Preparation of beams for static and dynamic loading

2.6.1.- Beams for static loading

The beams were coupled in pairs with two long stainless steel bolts through the plastic tubes positioned at the top and the bottom of the beam. These bolts were also used to lift the coupled beams. Between the beams also a small bar of stainless steel was collocated as fulcrum at the crack level. In this way the beams were constantly under static loading in three-point bending. The load is applied by the torque force at the bolts, which also allow maintaining the crack opening around 0.3 mm. Figure 2.4 (left) shows the coupling of the beams for static loading.

2.6.2.- Beams for dynamic loading

For dynamic loading, two clamps were used at the top and the bottom to couple the beams, instead of the bolts, since the plastic tubes were not completely aligned. This was necessary because the beams had to be perfectly parallel to each other, in order to put a hydraulic

cylinder (actuator) between them at the level of the crack for applying the load. The cylinder was fixed to a metallic clamp and attached to one beam (at the crack level), and a second clamp was attached to the other beam, so that the force of the piston was exerted over this clamp. In this way, the dynamic beams were also loaded in three-point bending, allowing a crack opening of an additional 0.1 mm. For this purpose a hydraulic pump connected to a function generator was used, and only the beams in solution were loaded. The original set-up for dynamic loading is shown in Figure 2.4 (right). Unfortunately, this set-up presented some difficulties such as oil leaking, spring failure and erosion of the piston, so that it was necessary to change it for a different set-up.

The new set-up consisted of a cylinder activated by compressed air and it was attached to the top of one of the coupled beams (Figure 2.5). A metallic plate was fixed to the second beam to which two rods were screwed along the sides of the beams and to a plate attached to the cylinder on the first beam (see Figure A.4 for details). The nuts at the two rods through which the cylinder is fixed to the plate were also used to set the piston travel/stroke. In this way, the crack is open by pushing the beams against each other. The three point bending was achieved by using a metallic tube between the beams at the crack level. A valve was connected to the cylinder, as well as a function generator to control the loading frequency. A manifold was used to distribute the load to the eight pairs of beams at the same time. For this reason the loading frequency was reduced to 0.5 Hz and the load was applied for around 15 hours per day.

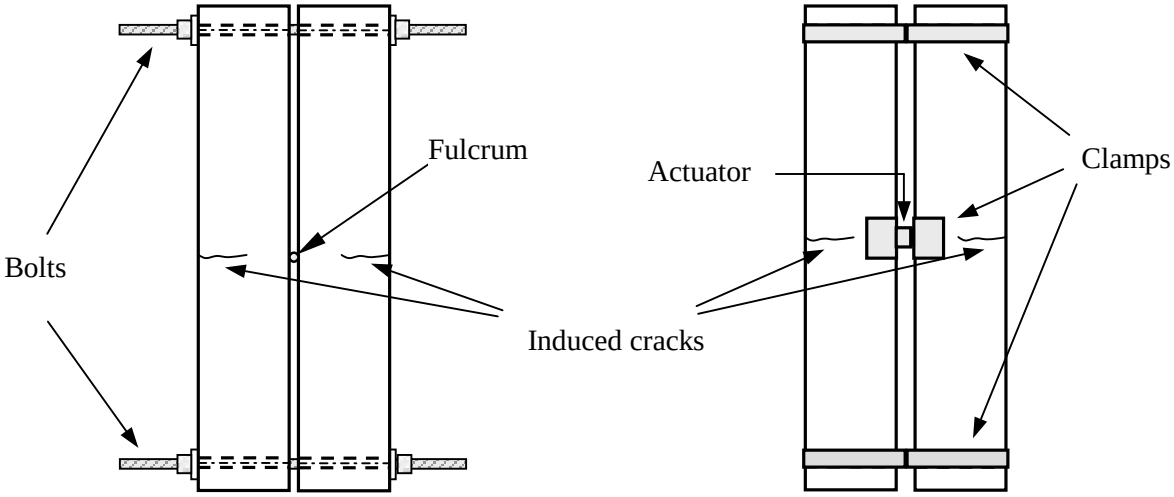

Figure 2.4.- Set-up for static (left) and dynamic (right) tests.

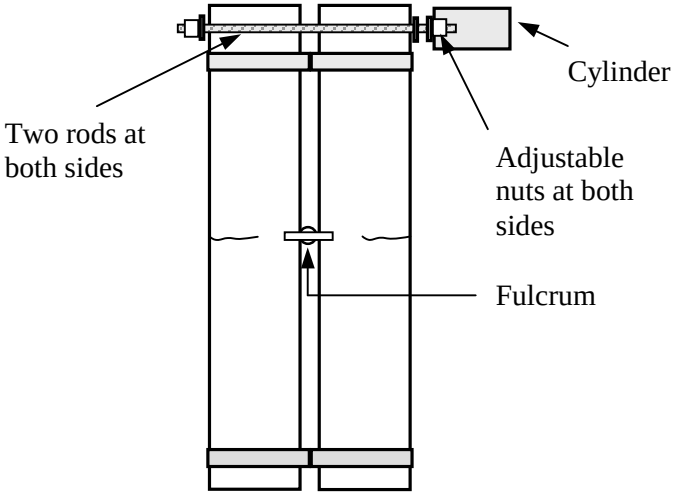

Figure 2.5.- New set-up for dynamic loading test.

2.7.- Corrosion tests

Four pairs of each type of concrete were vertically placed in four different tubs. Two pairs of each concrete were under static loading while the other two were under dynamic loading. They were immersed in the solution to just above the crack level and tested under wet-dry cycles. The specimens were immersed for two weeks and kept dry for other two weeks to complete one cycle. The level of the solution was kept just above the crack region, so that the top corrosion probes not be submerged during the test but the probes at the bottom and crack level would be. With the new dynamic loading set-up, the load was activated by high-pressure air through the cylinder.

2.7.1.- Solution of de-icing salts

A 3% chloride solution of commercial de-icing salts was used in the test. Tables 2.4 and 2.5 show the chemical analyses of the de-icing salts. To obtain a 3% chloride concentration 24.3 kg of de-icing salts were dissolved in 424.8 litres of tap water. Fresh water was added periodically as needed to maintain constant water level and chloride concentration. The concentration was measure every two weeks by potentiometric titration. A TitraLab 80 titration system from Radiometer was used for this purpose. A Hg/Hg_2SO_4 reference electrode and a silver electrode were used in the measurements. The measurement of the chloride concentration lies in the precipitation of silver chloride (AgCl) when a solution containing chloride ions is titrated with a silver nitrate ($AgNO_3$) solution.

A small sample of the solution was taken from the tanks by using a syringe and subsequently filtered through a 0.45 μm filter attached to the tip of the syringe. From this filtered solution was taken 50 μL with an automatic micropipette and transferred to another beaker to which distilled water was added to reach 50 mL of solution. A drop of nitric acid (HNO_3) was also added to get an acidic solution. Afterwards, the procedure was followed according to the instructions manual of the titration system.

Table 2.5.- Concentration of most important anions and cations in the de-icing salt solution and in distilled water.

Element	Distilled Water (mg/L)	De-icing Salt Solution (mg/L)
Cl^-	0.06*	10900
NO_3^{2-}	<0.05	2.83
SO_4^{2-}	0.06*	72.1
Ca^{2+}	<0.005	34.7
K^+	0.461	4.38
Na^+	<0.065	7510**

* Difficult to get consistent results due to low concentrations

** Dilution was 1:50. All others diluted 1:5

2.7.2.- Electrochemical measurements

2.7.2.1.- Corrosion Potential

The corrosion potentials of the carbon steel probes were monitored twice per day, whereas the corrosion rates were measured monthly after two weeks of immersion in the salt solution (once every two weeks dry and two weeks in solution).

The beams were connected to junction boxes to facilitate the measurements of such a large number of corrosion probes, and also to reduce the risk of errors during the measurements. The corrosion potentials were measured through a data acquisition system (manufactured by Keithley Instruments model 2750) connected to a computer and using a LabView program designed for this purpose. The wiring configuration between the junction boxes and the data acquisition system is tabulated in tables A.1-A.4 from the Appendix. The corrosion potential of each black steel probe (working electrode) was measured with respect to the stainless steel probe (used as a reference electrode) twice per day. In the case of the dynamically loaded beams, one measurement coincided with the loading period and the other with the stationary

period. Only 5 probes (out of 9) per beam were monitored, one at the top (non-submerged), one at the bottom (submerged), and three at the crack level.

The corrosion potentials of some black steel and stainless steel probes were also measured versus the ERE in the case of the beams containing this type of electrode, as well as versus an external saturated calomel electrode (SCE). A wet sponge was used to measure the potential versus the SCE. The measurements were taken manually by means of a Hewlett Packard Multimeter model 34401A.

2.7.2.2.- Corrosion rate

The corrosion rate was measured on all 9 probes using the Linear Polarization Resistance (LPR) and Electrochemical Noise (EN) techniques. The measurements were done by means of a corrosion monitoring system manufactured by Real Time Corrosion Management Limited (CML). This piece of equipment allows monitoring eight probes at the same time through its eight channels. In this case the LPR method is based on the two-electrode configuration. Thus, a black steel probe acted as the working electrode, whereas the stainless steel probe acted both as counter electrode and reference electrode. The LPR measurement consisted in the application of a potential signal of ± 20 mV with respect to E_{corr} in the form of a square wave between a black steel probe and the stainless steel probe. The steady current response is then measured and the polarization resistance is calculated as the ratio of the potential gradient to the current gradient (see Figure 2.6). The corrosion rate is obtained from the polarization resistance through the Stern-Geary equation. According to the instrument manual the corrosion current (I_{corr}) for a two-electrode configuration is determined as follows:

$$I_{corr} = 2B/(R_p \cdot A) \qquad 2.1$$

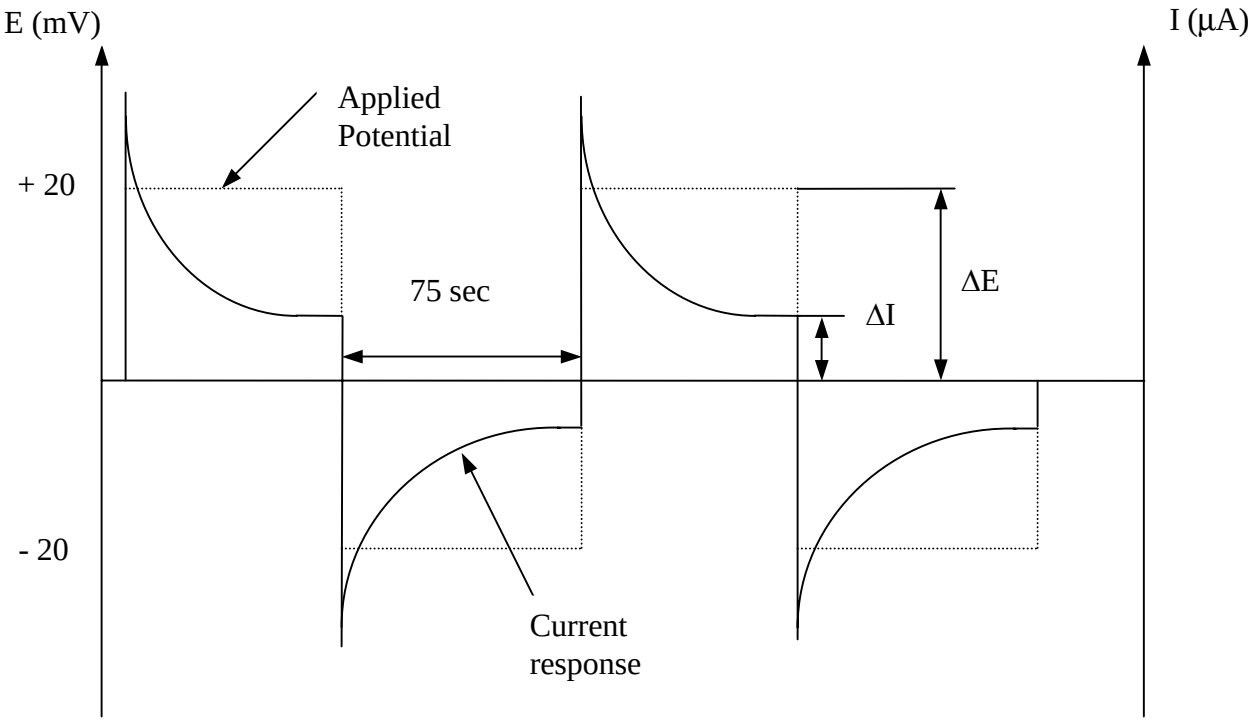

Figure 2.6.- Applied potential and current response during LPR measurements.

LPR measurements were also made using a Multi-Purpose Potentiostat/Galvanostat from Princeton Applied Research (PAR) model ParStat 2263-2. In this case was used both two- and three-electrode configurations. In the three-electrode configuration an external reference electrode of calomel (SCE) was used. The influence of the ohmic resistance on the magnitude of the corrosion rate was evaluated by selecting IR drop compensation provided in the software.

The fluctuations of the potential and current due to electrochemical processes were monitored by means of the EN technique. Values of potential of 0.1μV and current of 0.01μA can be measured. In this case the three black steel probes are used simultaneously, taking one common for both measurements, as shown in Figure 2.6. A data set of 1024 points was collected for each measurement at a rate of one point per second. The standard deviation for

each set of data was determined in order to calculate the noise resistance, and thus determine the corrosion rate by the Stern-Geary relationship. The noise resistance was calculated as the ratio of the voltage standard deviation to the current standard deviation (Equation 1.16). The corrosion current will be:

$$I_{corr} = 2^{1/2} \cdot B/(Rn \cdot A) \qquad 2.2$$

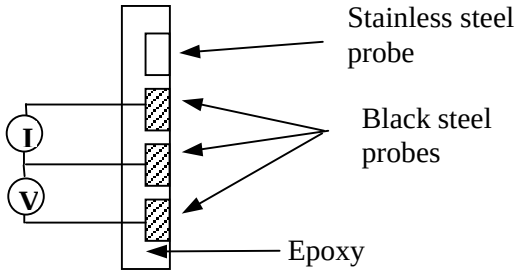

Figure 2.7.- Set-up for Electrochemical Noise Measurements.

2.7.2.3.- Electrochemical Impedance Spectroscopy (EIS)

The mechanism of the corrosion as well as the corrosion rate was determined by EIS using the same Potentiostat/Galvanostat model ParStat 2263-2. A 10 mV sine waveform was applied to the electrodes in a frequency range from 1 MHz to 3 mHz. The EIS data was fitted to an equivalent circuit, which allowed the calculation of the polarization resistance, the double layer capacitance and the resistance of the concrete, i.e. the ohmic resistance. The software ZSIMPWIN from PAR was used in the determination of the equivalent circuit.

2.7.2.4.- Cyclic Polarization

Cyclic Polarization curves were also obtained to determine the tendency to pitting corrosion on the corrosion probes using the Potentiostat/Galvanostat model ParStat 2263-2. The potential scan was started at -50 mV (vs. SCE) and continued in the positive direction until 500 mV with respect to the corrosion potential. Afterwards the scan was reversed until the corrosion potential. Figure 2.8 shows a schematic representation of the polarization curve of a metal (such as steel in concrete) that exhibits active to passive behaviour (without chlorides), and the cyclic polarization curve when the metal is undergoing pitting corrosion in the presence of chloride ions. Three regions can be distinguished from this curve depending on the corrosion activity of the metal: active, passive and transpassive. As can be seen, the presence of chlorides provokes a decrease of the passive region (potential range) and the reverse scan forms a hysteresis loop as a result of pitting corrosion. From the cyclic polarization curve, the pitting (E_{pit}) and the protection (E_{prot}) potentials can also be determined.

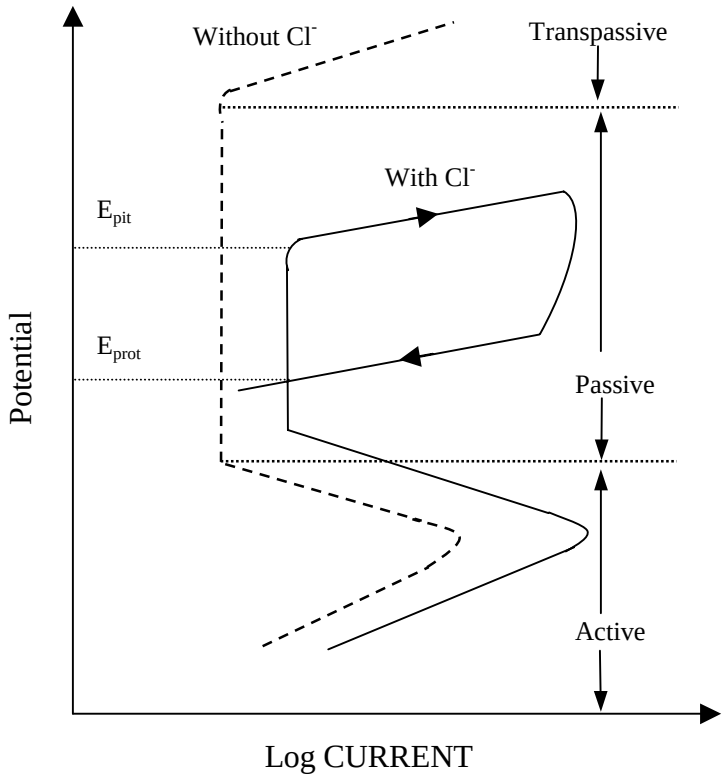

Figure 2.8.- Schematic representation of the cyclic polarization curve (Jones 1996).

3. Experimental Results

The results obtained from the static and dynamic tests are presented in the following section. The evaluation of the corrosion potentials and the corrosion rates measurements are summarised for each type of concrete and exposure condition. Each beam was identified depending on the type of concrete; thus, for HPC-Fly Ash will be F, HPC-Slag S, OPC-C C and OPC-TC TC. The corrosion probes were also identified as R1, R2 and R3 (see Figure A.2 of Appendix).

3.1.- Static Beams

3.1.1.- Corrosion Potentials

Corrosion potential measurements started after 20 weeks of immersion of the beams in the solution. The corrosion potentials for each type of concrete are plotted in Figures 3.1-3.4. Each plot represents the values obtained for the three probes at the crack, one at the top (non-submerged) and one at the bottom (submerged) for all the beams of the same type of concrete. The corrosion potentials were measured versus the stainless steel (S.S.) and changed to the copper/copper sulphate scale (CSE) to compare them with the values suggested in the ASTM standard C876-91 (see Table 1.2). For this purpose the corrosion potential of the embedded stainless steel was measured with a multimeter after two weeks in solution versus the saturated calomel electrode (SCE) and then transformed to the CSE scale. Thus, the final corrosion potential was determined as follows:

$$E_{corr} \text{ (Volts vs. CSE)} = - E_{corr} \text{ (Volts vs. S.S.)} + E_{S.S.} \text{ (Volts vs. SCE)} - 0.072$$

where,

E_{corr} (Volts vs. CSE) = Corrosion potential of carbon steel probes versus CSE;

E_{corr} (Volts vs. S.S.) = Corrosion potential of carbon steel probes versus the stainless steel (measured with the DAQ);

$E_{S.S.}$ (Volts vs. SCE) = Potential of the stainless steel versus SCE; determined as described above.

The value 0.072 corresponds to the difference between the SCE and the CSE in the hydrogen scale (Standard Hydrogen Electrode).

As can be seen from Figures 3.1-3.4 the corrosion potentials were plotted in histograms instead of scatter plots, which might be better to see their trends when the beams are dry or wet, but the continuous variations of the stainless steel potential make difficult to follow their behaviour. Furthermore, in this format, it is also possible to consider all the values obtained, which can be very different for the same type of concrete.

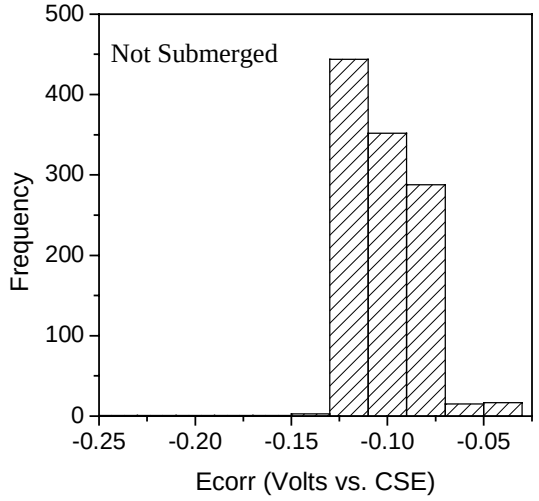

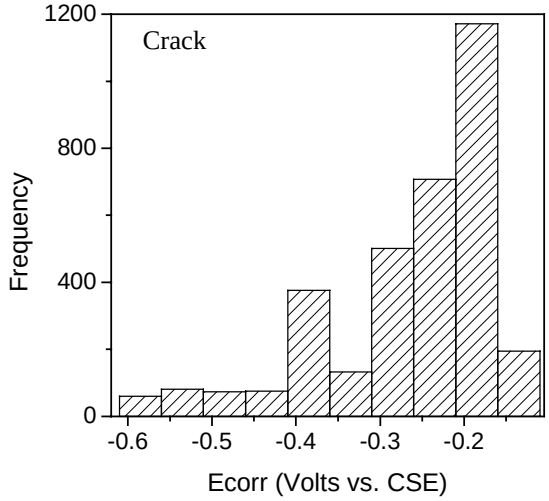

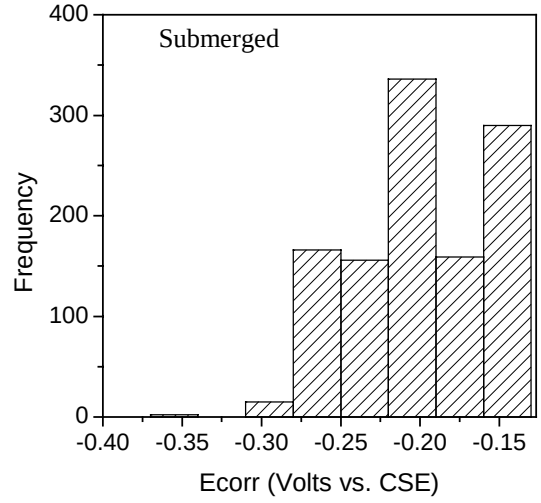

Figure 3.1.- E_{corr} Histograms for static HPC-Fly Ash beams. Frequency refers to the number of measurements.

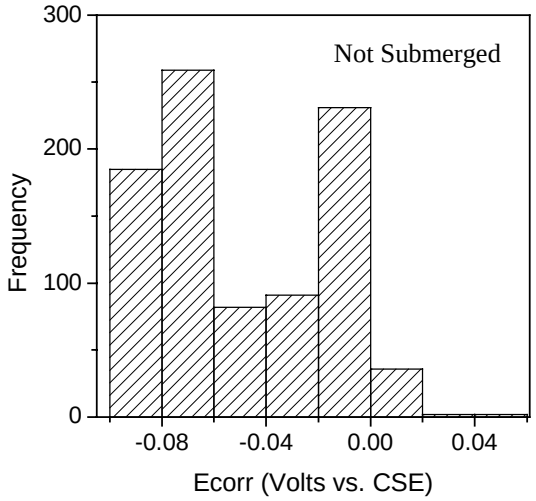

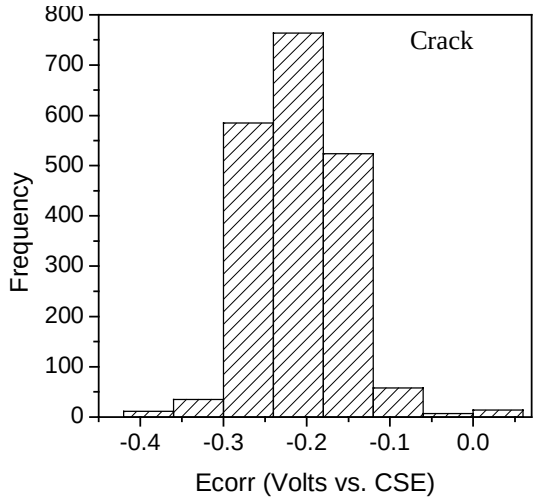

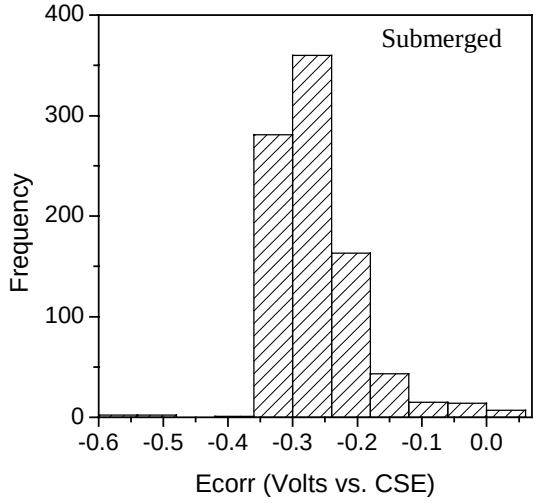

Figure 3.2.- E_{corr} Histograms for static HPC-Slag beams. Frequency refers to the number of measurements.

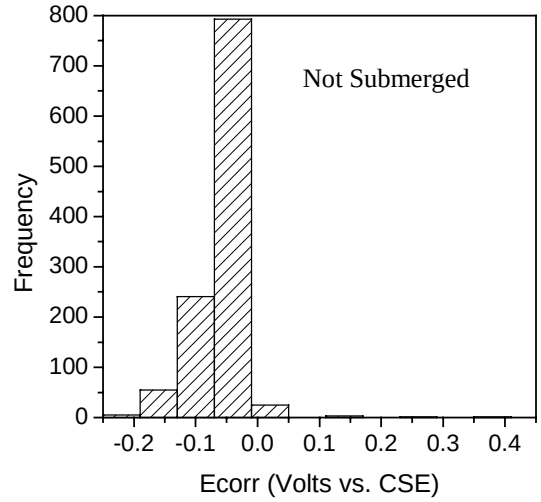

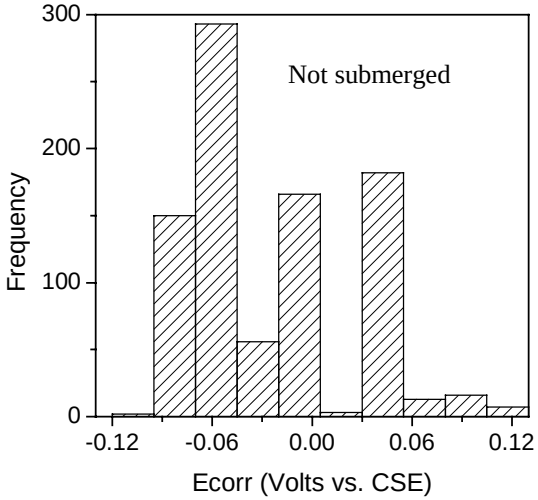

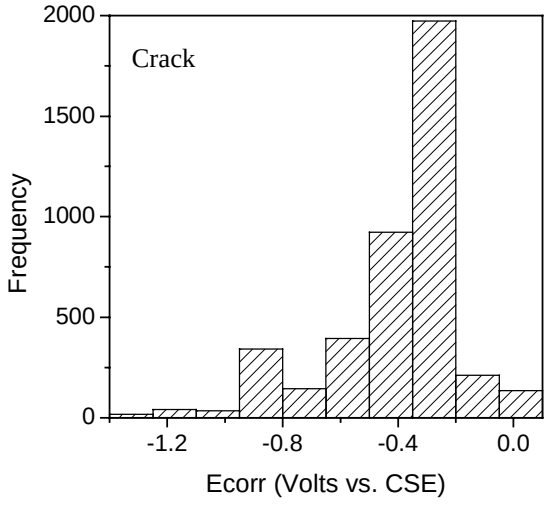

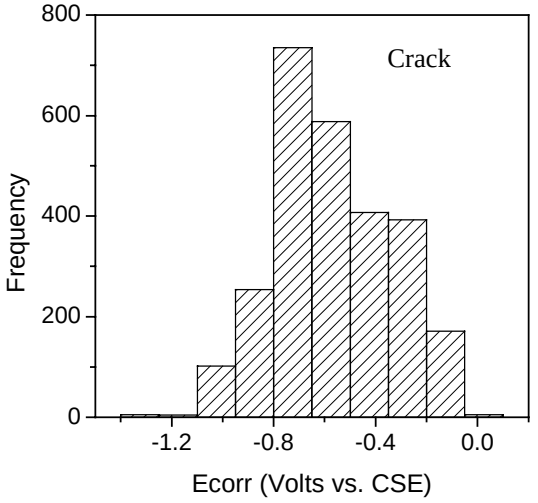

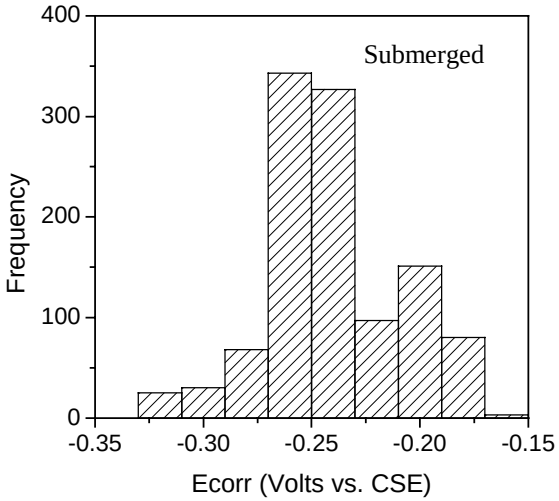

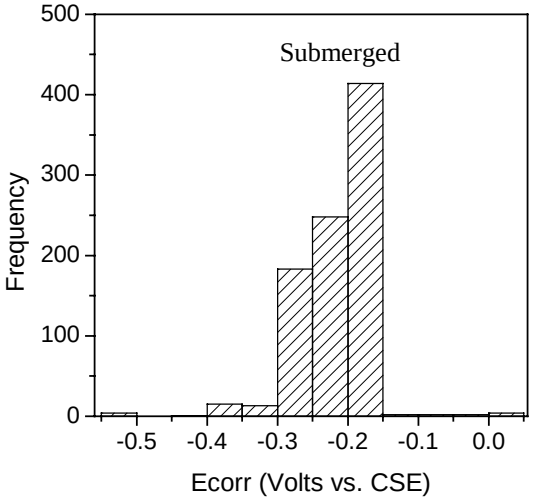

Figure 3.3.- E_{corr} Histograms for static OPC-C beams. Frequency refers to the number of measurements.

Figure 3.4.- E_{corr} Histograms for static OPC-TC beams. Frequency refers to the number of measurements.

Tables 3.5 and 3.6 show the potentials of stainless steel after two weeks dry and after two weeks wet, as well as the potential of the embeddable reference electrode (ERE) versus SCE. As it was mentioned above, the stainless steel potentials after two weeks wet were used to transform the corrosion potentials to the CSE scale. In this way, the most negative values are considered, which also coincide with the day of the corrosion rate measurements. Nevertheless, the number of more positive corrosion potentials in Figures 3.1-3.4 may increase in the case where the potential of the stainless steel shows the largest changes. It should be also noted that the potentials of the stainless steel after 45 weeks in solution can be very different from those obtained at the beginning of the test, but the E_{corr} of the carbon steel were measured before starting the measurements by the DAQ. The potential of the ERE showed fairly steady values, although those in TC and C showed variations of around 10 mV during a wet/dry cycle.

Taking into account these changes of the stainless steel potential, the E_{corr} values from most of the corrosion probes do not vary significantly during the testing period. The HPC-Fly Ash beams showed the steadiest E_{corr}. This was verified by measuring the E_{corr} of the carbon steel probes submerged and at the crack versus the ERE (on beams F4, S10, TC4 and C8). As can be seen from Tables B.1 and B.2 of Appendix B, the largest variations in E_{corr} during the wetting and drying stages were obtained for the probes at the crack. The changes in E_{corr} were around 200 mV (vs. ERE) in all the cases. Measurements of E_{corr} versus SCE were also made (on beams F1, TC4 and C10) and gave similar results.

Table 3.1.- Potential of stainless steel in HPC after two weeks dry and two weeks wet.

Level	E_{corr} (mV vs. SCE)							
	F1	F3	F4	F6	S1	S5	S7	S10
Not submerged	-11	30	0.4	-35	-2	-2	40	40
Crack-Dry	-541	-128	-69	-5	-211	-75	-255	-230
Crack-Wet	-575	-166	-88	-49	-235	-108	-270	-239
Submerged -Dry	-90	-91	-71	-77	-111	-84	-107	-194
Submerged -Wet	-116	-120	-93	-92	-224	-101	-222	-210
ERE	-	-	89	-	-	-	-	78

Table 3.2.- Potential of stainless steel in OPC concrete after two weeks dry and two weeks wet.

Level	E_{corr} (mV vs. SCE)							
	C3	C8	C9	C10	TC3	TC4	TC5	TC6
Not submerged	43	-60	35	60	1	4	25	70
Crack-Dry	-290	-180	-128	-184	-280	-280	-603	-420
Crack-Wet	-322	-238	-150	-809	-664	-485	-627	-672
Submerged -Dry	-156	-111	-134	-143	-103	-43	-162	-76
Submerged -Wet	-160	-157	-152	-170	-108	-93	-252	-169
ERE	-	80	-	-	-	65	-	-

The effect of the stainless steel potential changes can be observed in Figures 3.5 for beam F4. This figure shows the E_{corr} of the carbon steel probes versus the stainless steel and versus ERE and, the potential of the stainless steel versus the ERE measured during a whole wet/dry cycle (two weeks dry and two weeks wet) for a HPC-Fly Ash beam (F4, probes 1 and 3). The first value corresponds to the potential after two weeks in solution, the second one when start drying until day 14, and then when start wetting. As can be seen from this figure the E_{corr} of the probe 1 (R1) versus ERE decreases when it is exposed to the solution, but versus the stainless steel is constant during the whole cycle. On the other hand, the E_{corr} of probe 3 (R3) versus ERE is relatively constant, whereas versus S.S. varies. This behaviour is due to the fact

that the stainless steel potential changes during the test period, and cancels (R1) or provokes variation (R3) in the E_{corr} of the corrosion probes. Other beams show similar conduct with changes even more pronounced than those exemplified in Figure 3.5.

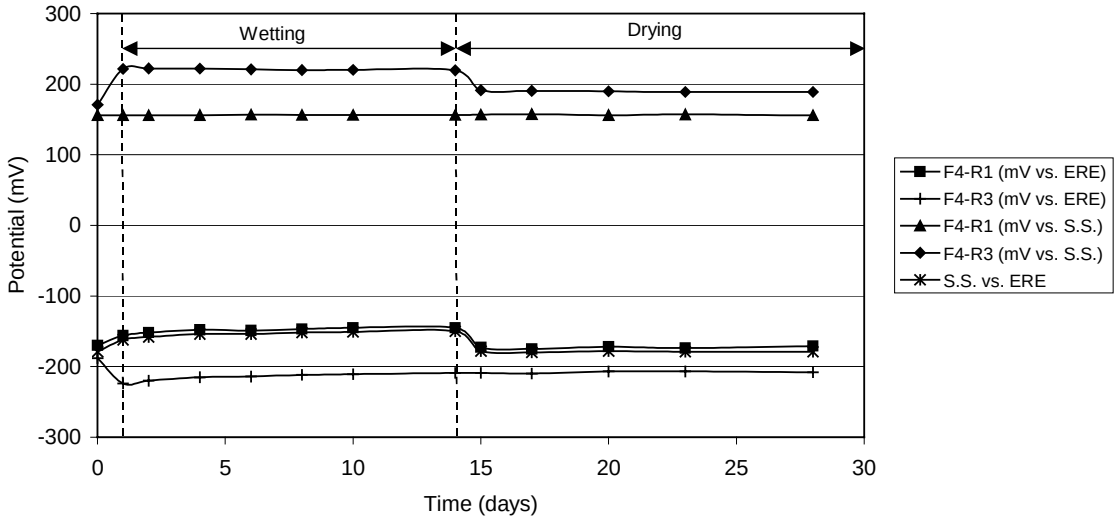

Figure 3.5.- Potential of corrosion probes of stainless steel during a wet/dry cycle.

Despite the abovementioned observations, the E_{corr} of the corrosion probes versus the stainless steel can still give an approximate idea of the probability of corrosion. In all the beams the probes at the top (non-submerged) showed the most positive values, whereas those at the crack are the most negative particularly in the OPC concretes, as can be seen in Figures 3.1-3.4. According to these figures the E_{corr} of the top probes, as well as most of the values from the submerged probes, the corrosion potentials are more negative than -350 mV (vs. CSE), indicating high probability of corrosion. However, the probes at the crack in OPC concretes are generally above this limit. The HPC concretes show more positive values in the crack region than OPC concretes, in such a way that many of them are still below the corrosion limit.

Figure 3.6 gives the E_{corr} averages for each probe at the crack and for each beam (3 probes per 4 beams for each concrete type). Notice that each point is independent of each other and that

they were joined by a line to have a better picture of the behaviour of E_{corr} for each type of concrete; it is not intended to show any tendency.

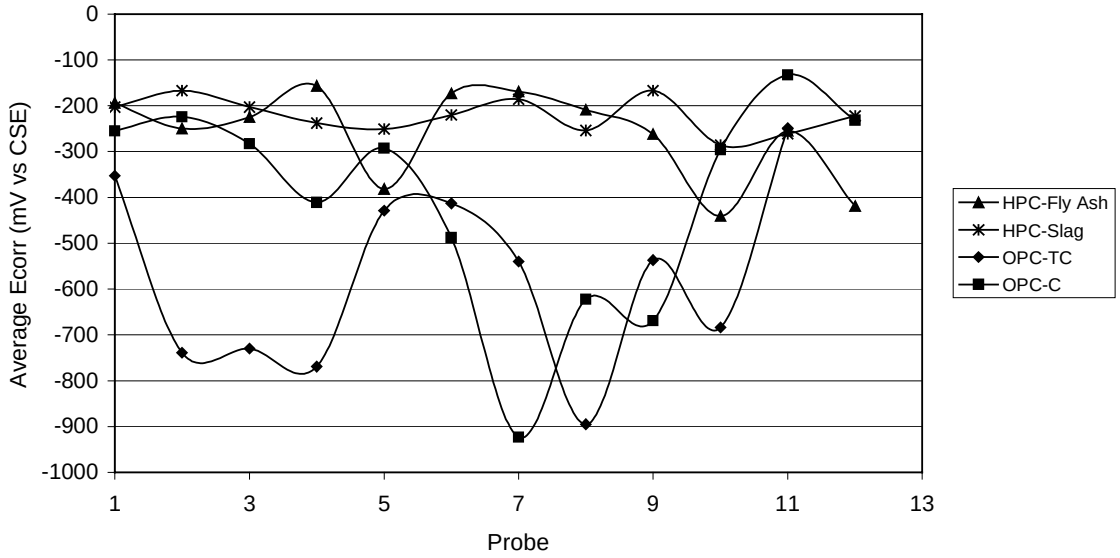

Figure 3.6.- Average corrosion potential for each probe measured at the crack. Each type of concrete is plotted in the following order (3 rebars by beam): HPC-Fly Ash (F3, F4, F6, F1); HPC-Slag (S10, S7, S5, S1); OPC-C (C9, C8, C10, C3); OPC-TC (TC6, TC3, TC5, TC4).

3.1.2.- Corrosion rates determined by LPR

In the following section are presented the corrosion rates measured with the CML for all the statically loaded beams. The corrosion rates were measured every month, after two weeks dry and two weeks in solution. The raw data are tabulated in Tables B.3-B.6 of Appendix B. Figures 3.7 and 3.8 reproduce the average corrosion rates of the corrosion probes at the different locations in each beam for each pair of HPC-Fly Ash concrete. Thus, each value corresponds to the average of the corrosion rates for the three probes located at each level, i.e. non-submerged (top), crack, and submerged (bottom). As can be seen from Figures 3.7 and 3.8 the corrosion rates are very low, most of them below 2.5 μm/year for all the probes, independent of the location in the beam. In general, the corrosion is highest for the probes at the crack region, followed for those submerged; however, some submerged probes showed

slightly higher or similar corrosion rates for short periods. The latter is reflected in Tables B.3-B.6 and it is confirmed by the more negative E_{corr} obtained for the submerged probe (mainly F3). A relatively high corrosion is observed for beam F4, which decreases with the exposure time.

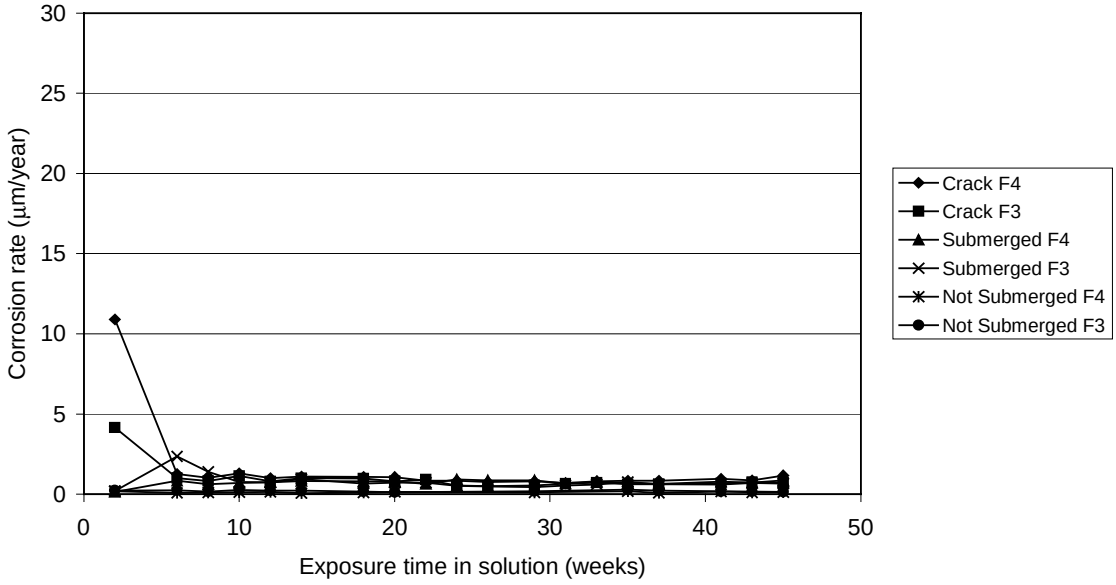

Figure 3.7.- Corrosion rates of HPC-Fly Ash beams (F3 and F4) statically loaded.

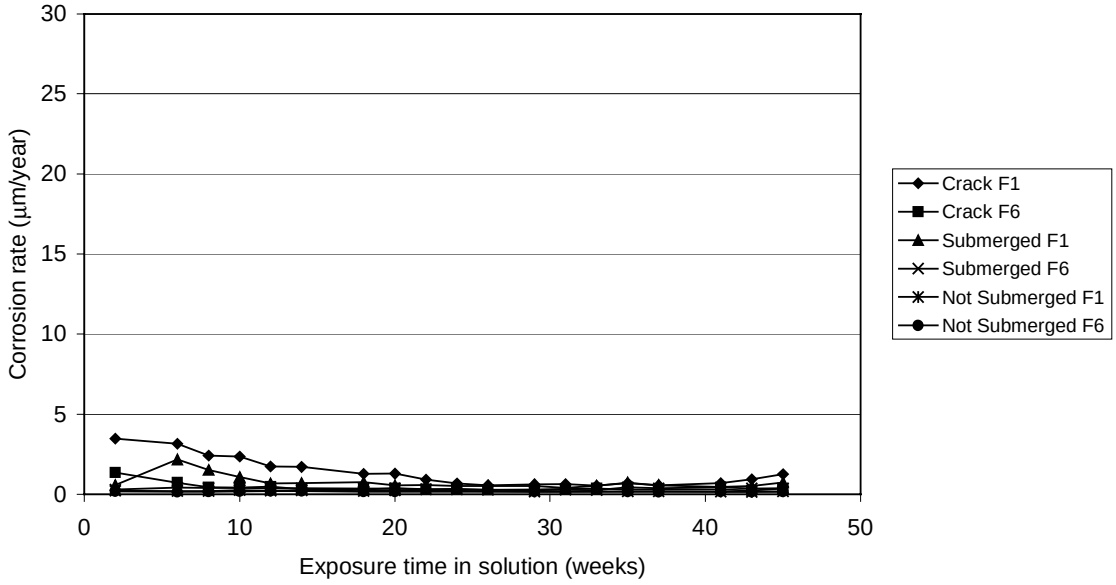

Figure 3.8.- Corrosion rate of HPC-Fly Ash beams (F1 and F6) statically loaded.

The corrosion rates of probes in HPC-Slag beams are plotted in Figures 3.9 and 3.10. Compared to those in HPC-Fly Ash beams, the steel in HPC-Slag beams show slightly higher corrosion rates but still below the 5 μm/year in most cases. A peculiarly high value is obtained during the first month of exposure. However, a decrease in the corrosion rate with time is also observed for probes in some of the HPC-Slag beams. In very few cases the corrosion rate of the submerged probes is close to those at the crack level; this is better observed in the raw data presented in Tables B.7-B.10 of Appendix B.

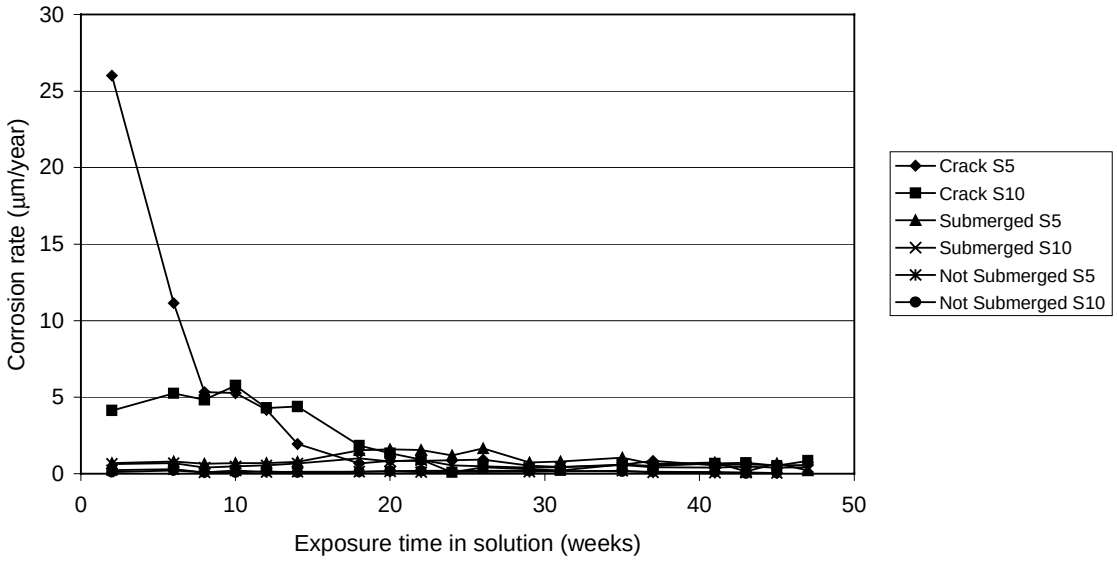

Figure 3.9.- Corrosion rate of HPC-Slag beams (S5 and S10) statically loaded.

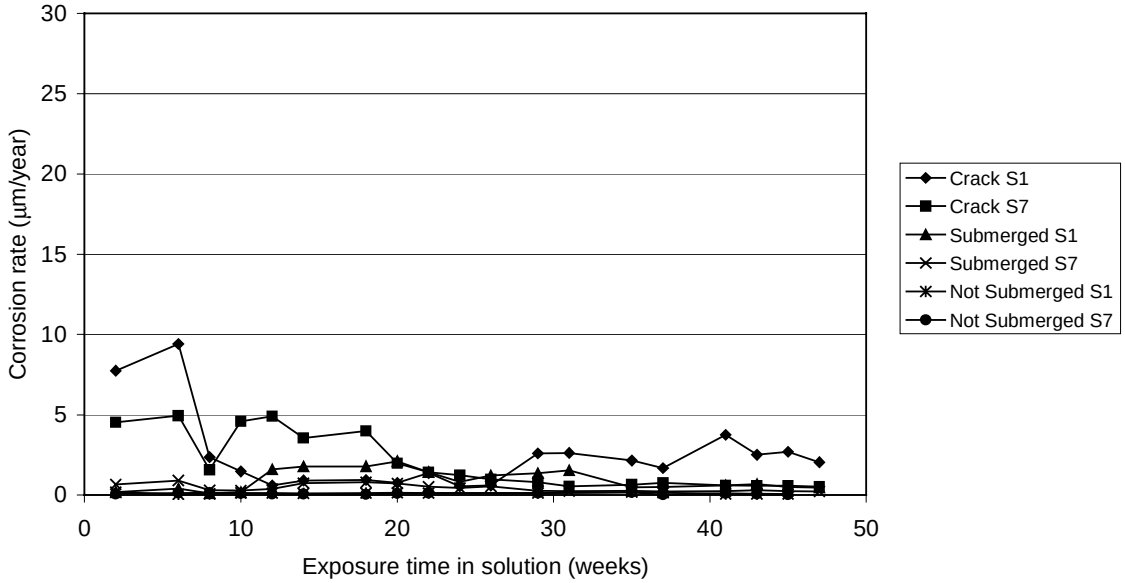

Figure 3.10.- Corrosion rate of HPC-Slag beams (S1 and S7) statically loaded.

Figures 3.11 and 3.12 correspond to the corrosion rates for probes in OPC-C, and Figures 3.13 and 3.14 for probes in OPC-TC. The corrosion rates for all the probes are shown in Tables B.11-B.14 and B.15-18, respectively. Bear in mind that the main difference between these two concretes is the date of casting. OPC-TC was cast and cured during the winter, whereas OPC-C was cast and cured during the summer together with HPC beams.

The probes in OPC-TC beams experienced the highest corrosion at the crack level in all the cases. OPC-C beams showed similar behaviour except for beam C9. It is evident from Figure 3.11 that the corrosion of the submerged probes in beam C9 is higher than that of the probes at the crack. From Table B.14, it is observed that even the three submerged probes show higher corrosion rates, mainly after the 25th week in solution, which has not been the case in the rest of the concretes.

As can be seen from Figures 3.13-3.14 the corrosion rates of probes in the OPC-TC beams are generally higher than those in OPC-C, and much higher than those in HPC-Fly Ash and HPC-Slag beams.

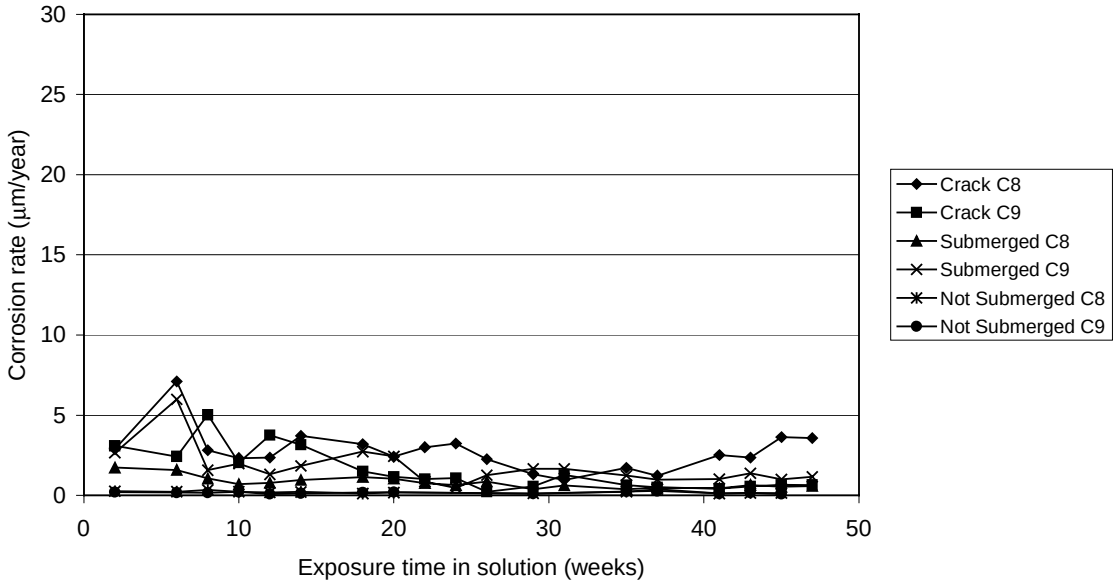

Figure 3.11.- Corrosion rate of OPC-C beams (C8 and C9) statically loaded.

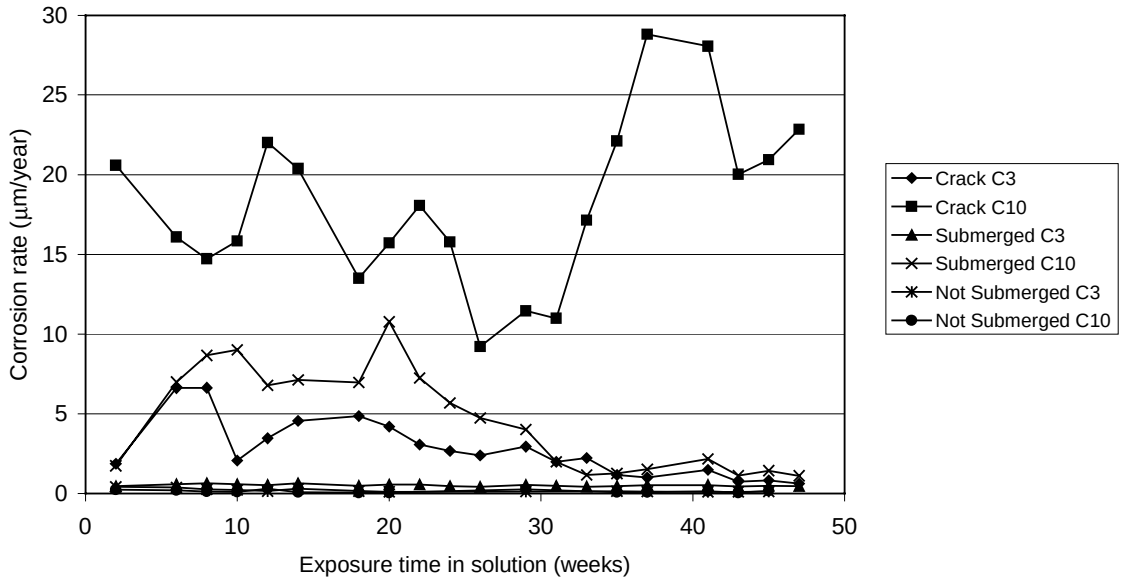

Figure 3.12.- Corrosion rate of OPC-C beams (C3 and C10) statically loaded.

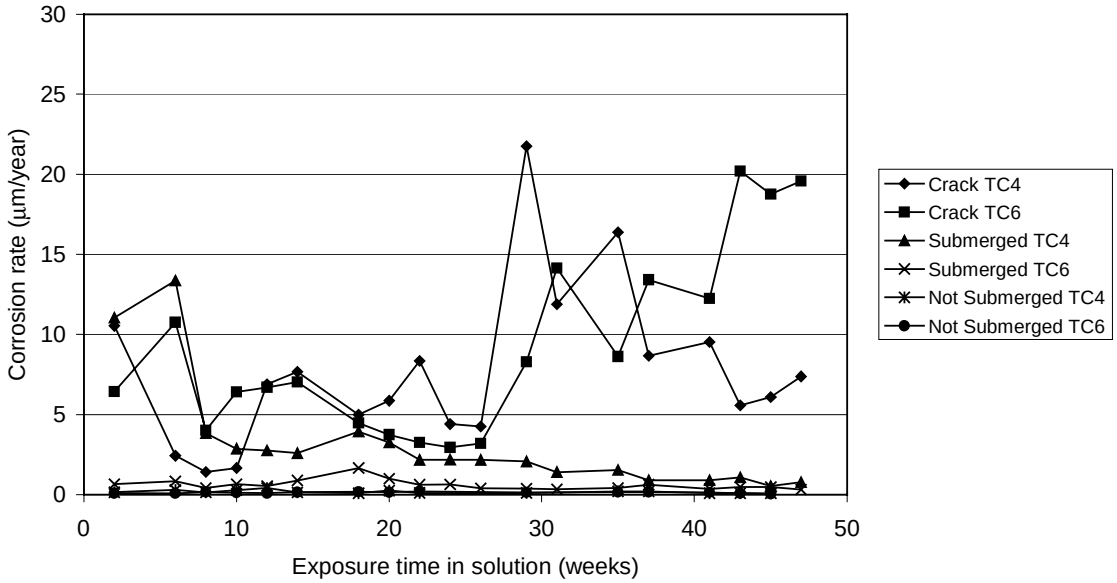

Figure 3.13.- Corrosion rate of OPC-TC beams (TC4 and TC6) statically loaded.

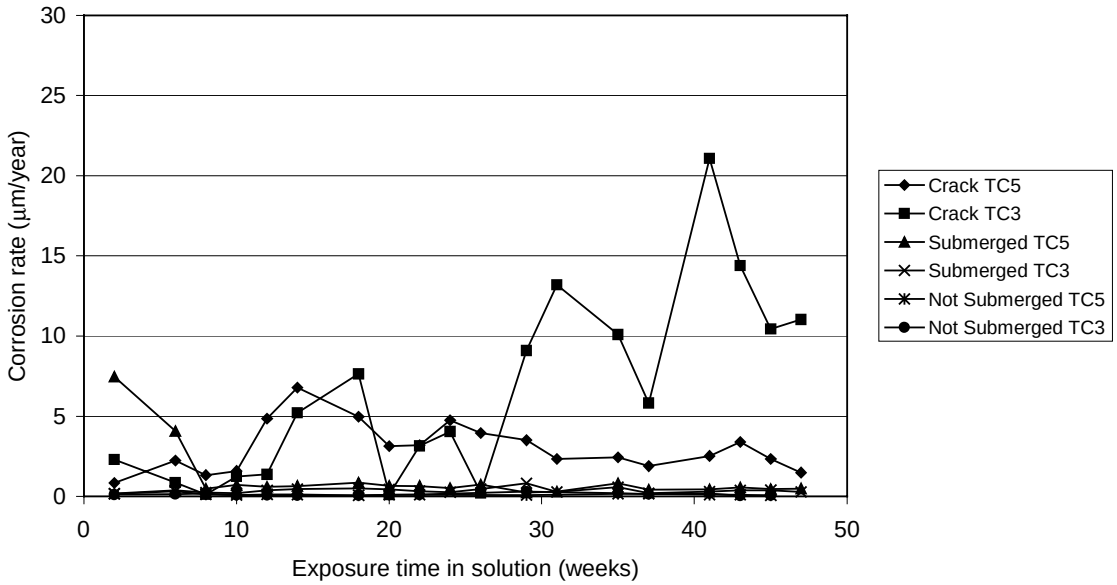

Figure 3.14.- Corrosion rate of OPC-TC beams (TC5 and TC3) statically loaded.

The CML corrosion rates measurements were confirmed by using the Potentiostat/Galvanostat PARStat 2263. For this purpose, pairs of OPC-C (C8&C9), OPC-TC (TC4&TC5) and HPC-Slag (S1&S10) beams were chosen, and the corrosion rate of the probes at the crack and submerged were measured (36 probes in total). The corrosion rates measured with the CML after 45 and 47 weeks in the de-icing salt solution, and the corrosion rates measured with the Potentiostat/Galvanostat ParStat 2263-2 (using a two-electrode configuration) after 47 weeks are plotted in Figure 3.15. As can be seen from this figure there exists a very good agreement between both measurement systems. The X-axis represents the individual probes at the crack and submerged.

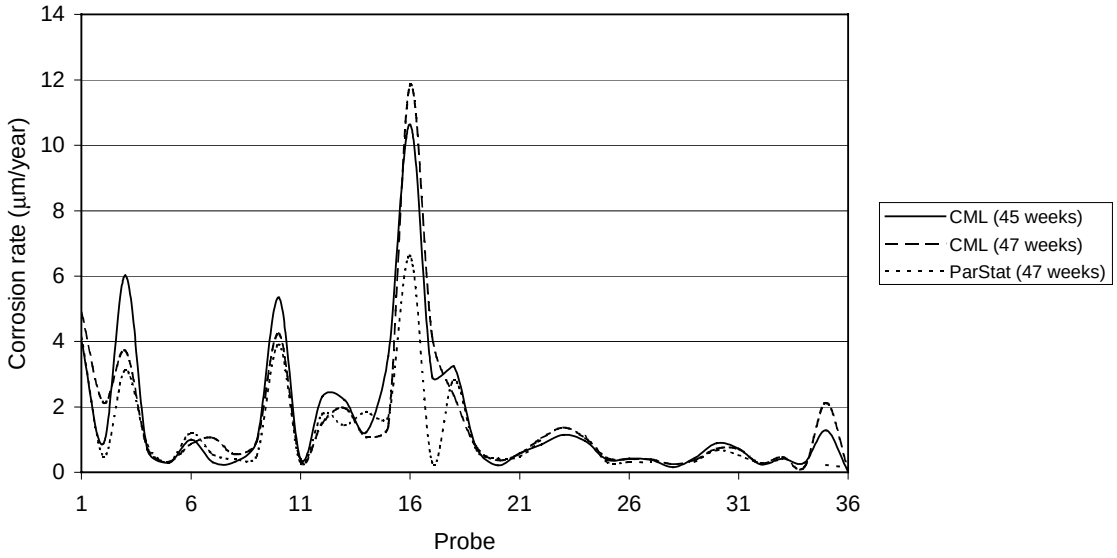

Figure 3.15.- Comparison of the corrosion rates measured by using the CML and the Potentiostat/Galvanostat on corrosion probes at the crack and submerged. Highest value corresponds to TC4-R1.

Three-electrode configuration measurements were also used with the Potentiostat/Galvonastat in order to study the effect of the IR drop through the solution/concrete on the value of the corrosion rate. However, it was not possible to evaluate the corrosion rate from the measurements made with IR compensation because of the noise in the current response. When IR compensation was not selected, the noise was avoided and the corrosion rate could be determined. Three-electrode configuration without IR compensation was also used to assess

the effect of the anode/cathode area ratio on the corrosion rate. For this purpose an external rod of stainless steel (exposed area 74.06E-04 m^2) was connected to two of the black steel probes (one at a time) at the crack from beams TC5 and C8. Since the stainless steel is more resistant to corrosion it would behave as a larger cathodic area than the corroding section, i.e. the corrosion probe (the cathodic/anodic ratio increase). This increase in the cathodic area resulted in a higher corrosion rate of the black steel probe, considering its area as the only corroding section. The increase of the area of the probe in the beam TC5 resulted in an increased of the corrosion rate from 1.91 to 153 μm/year, whereas the probe in the beam C8 increased from 0.37 to 170 μm/year.

Table B.15 of Appendix B shows the corrosion rate measurements after the two-week drying stage (after 45 weeks in solution). The latter was done on the probes at the crack and at the bottom (submerged) for all the beams. According to the results, for most of the probes, the corrosion rates did not experience major differences between the ones obtained during wetting and those obtained during drying. The most remarkable difference is observed for C8-R1, which showed an increase of around 10 times from the dry to the wet condition.

3.1.3.- Cyclic Polarization curves

The Cyclic Polarization technique was used to determine if there were any tendency to pitting corrosion especially on OPC-C (C8-R1) and OPC-TC (TC5-R2) beams, which exhibit the highest corrosion rates. It should be kept in mind that this technique is considered destructive (at least in the short term) since it changes the conditions on the electrode surface as a result of the large range of potential scanned. For this reason only one probe at the crack level for both types of concrete was analyzed. The potential was positively (anodically) scanned from -50 mV to 500 mV (vs. SCE) with respect to the corrosion potential, and after reaching this value, the scan was reversed in the negative (cathodic) direction until E_{corr} (note that for the beamTC5-R2 the scan was stopped at -200 mV (vs. SCE)). Figure 3.16 shows the cyclic polarization curves for both cases. As can be seen from these curves the probes do not seem to

undergo pitting corrosion, even though they are among the most corroded according to the LPR measurements.

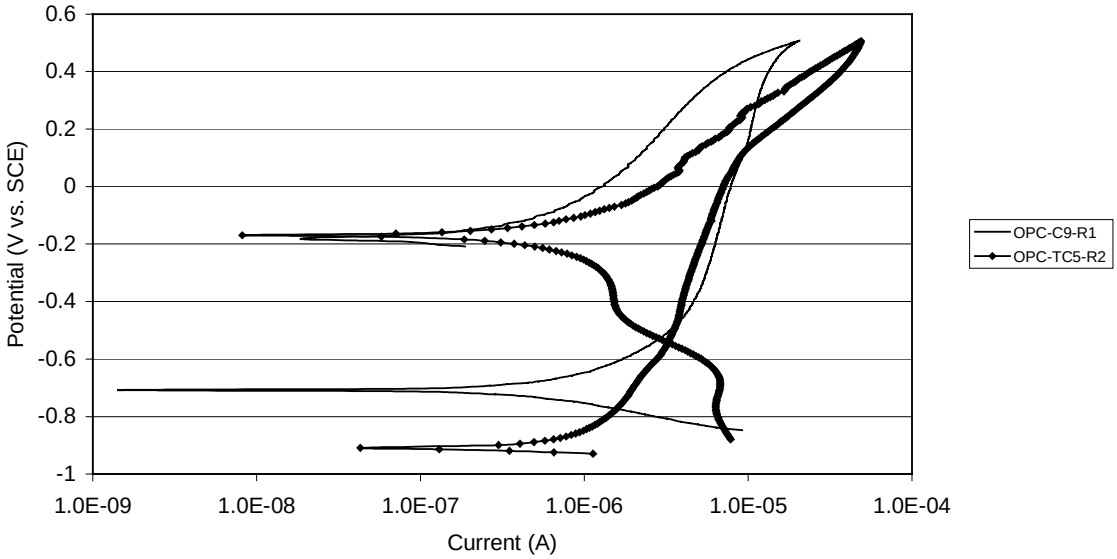

Figure 3.16.- Cyclic polarization curves for probes at the crack in C9 and TC5 beams statically loaded.

3.1.4.- Electrochemical Noise

The electrochemical noise measurements were started after 22 weeks of immersion in the chloride solution. Figures 3.17-3.20 illustrate some examples of the electrochemical current noise (ECN) and the electrochemical potential noise (EPN) from the probes at the crack and submerged. In general, the non-submerged probes showed very low noise levels, although very fluctuating, probably due to the retention of the passivity of the corrosion probes.

In most of the cases, the ECN of the probes at the crack was higher than the one from the submerged probes. This can be observed in Figures 3.17 and 3.20 and please note the different ordinate scales in these figures. These figures also demonstrate the higher ECN of the C3 beam compared to the ECN of F4, which is in agreement with the LPR results. The ECN results from the corrosion current flowing between two corrosion probes when one electrode

becomes more or less anodic with respect to the other; that is, it is not an absolute value of the corrosion current. However, its mean value can give an estimate of the corrosion activity. Figure 3.19, on the other hand, represents a case when the corrosion of the submerged probes is higher than those at the crack. The latter confirms the results obtained through the LPR measurements (Appendix B).

Figure 3.20 displays ECN (the current noise) curves for probes in TC6 that showed suddenly spikes, which then return slowly to the baseline. This behaviour was only observed during these two measurements of TC4 under submerged conditions and TC6 at the crack. This pattern is characteristic of the initiation of pitting corrosion, although crevice corrosion also has similar patterns, making difficult to differentiate between each other. However, for longer periods the patterns of the curves were similar to those previously discussed. As Figure 3.20 illustrates, the EPN (the potential noise) was not able to detect the sudden changes in the corrosion activity of the corrosion probes. This indicates that ECN may be a more reliable indicator of pitting corrosion than EPN. However, the removal of background noise using digital filters can reveal in some cases a correlation between ECN and EPN.

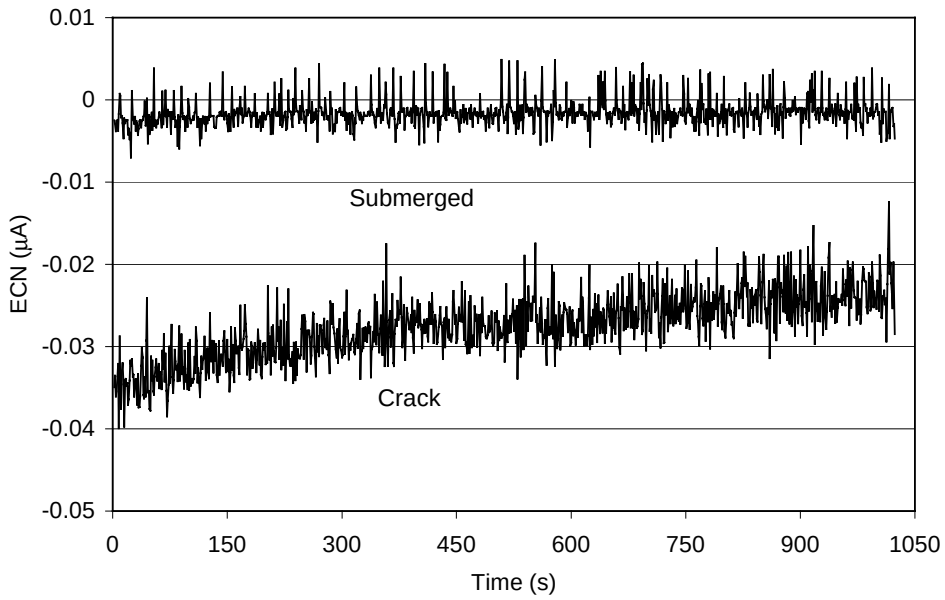

Figure 3.17.- ECN from the probes at the crack and submerged of a Fly-Ash beam (F4) statically loaded.

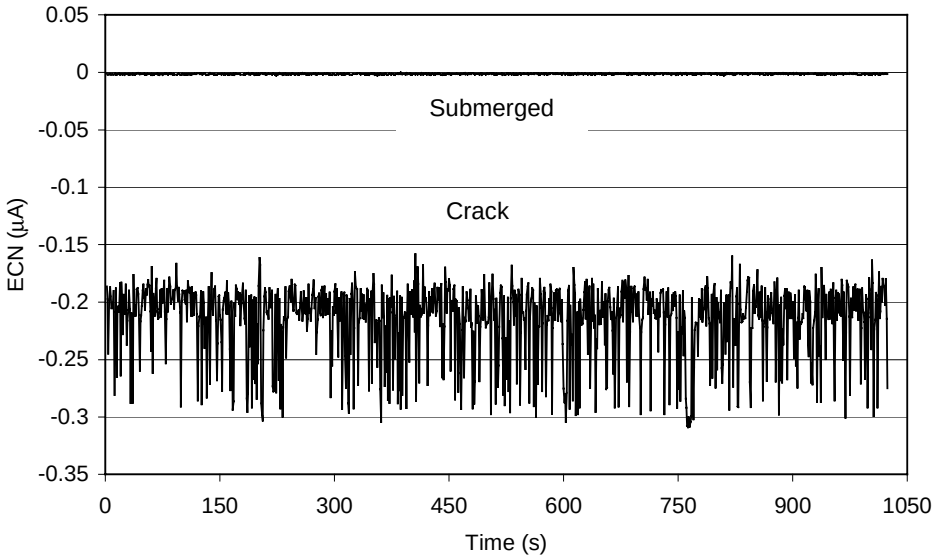

Figure 3.18.- ECN from the probes at the crack and submerged of a OPC-C beam (C3) statically loaded.

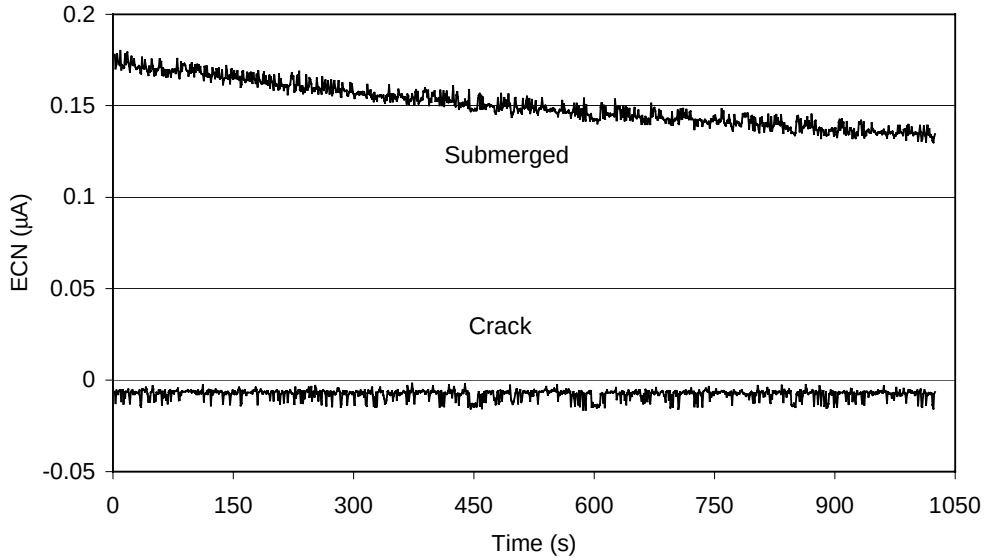

Figure 3.19.- ECN from the probes at the crack and submerged of a OPC-C beam (C9) statically loaded.

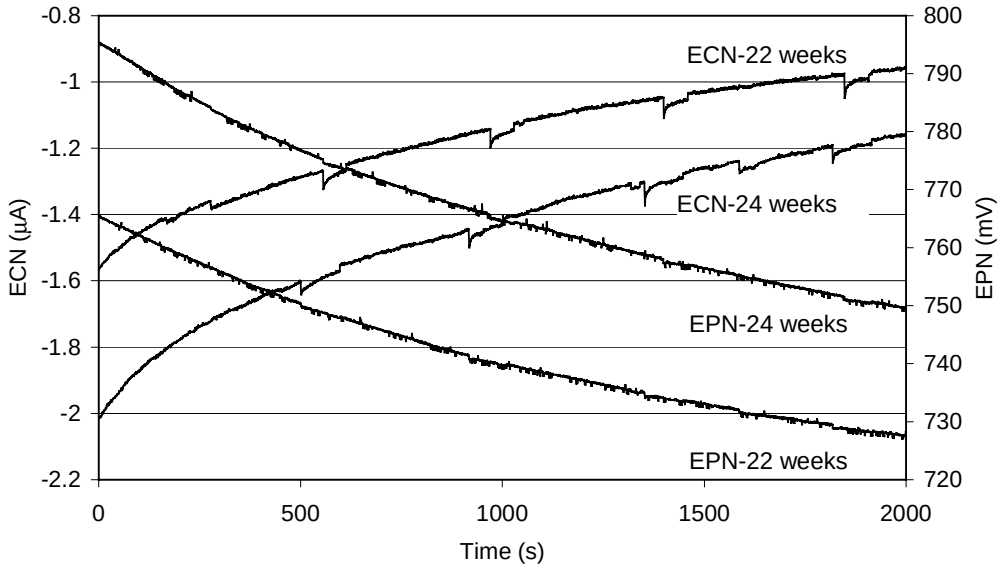

Figure 3.20.- ECN and EPN from the probes at the crack and submerged of a OPC-TC beam (TC4) statically loaded.

3.1.5.- Electrochemical Impedance Spectroscopy

Figures 3.21 and 3.22 summarise some of the EIS measurements after two weeks in solution (after the 45th week) for the different concretes. The measurements were performed using two electrodes, the stainless steel as the counter electrode and one of the corrosion probes as the working electrode. Figure 3.21 represents the logarithm of the impedance versus the logarithm of the frequency (Bode plot) for one probe at the crack from each type of concrete. Figure 3.22 illustrates the imaginary component of the impedance versus the real component (Nyquist plot) for the same probes. As can be seen from Figure 3.21 the HPC-Fly Ash beam shows the highest impedances at intermediate frequencies, which is mainly due to the resistance of concrete. The lowest value is obtained for the OPC-C beam. However, the latter also shows a large capacitive component (a slope close to -1 is indicative of a capacitive behaviour) at lower frequencies, as it is also observed on the Nyquist plot (Figure 3.22). The semicircle at low frequencies is characteristic of the electrochemical reactions. This could explain the fact that the corrosion rate determined by LPR is larger for TC3 than for C8 (see Figures 3.11 and 3.14).

The EIS spectra from the submerged probes were generally very variable between probes within the same beam, as well as for beams of same type of concrete. Some of them seem to show diffusion control (a slope of -0.5 is indicative of diffusion control) at low frequencies, whereas others present a very large semicircle. In the case of the probes non-submerged a very capacitive behaviour is observed for practically all the beams.

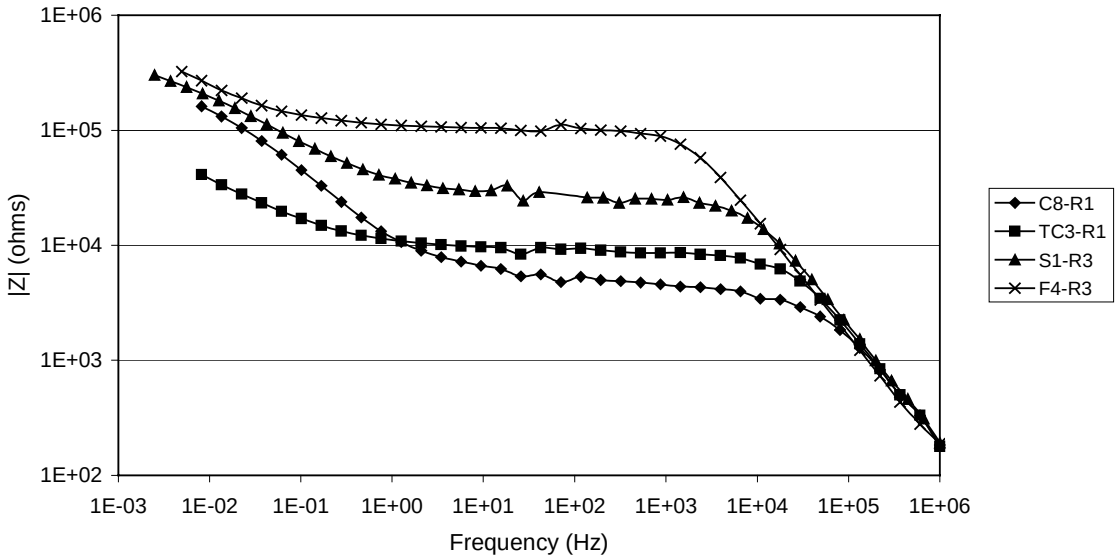

Figure 3.21.- Bode plot of one probe at the crack for each type of concrete.

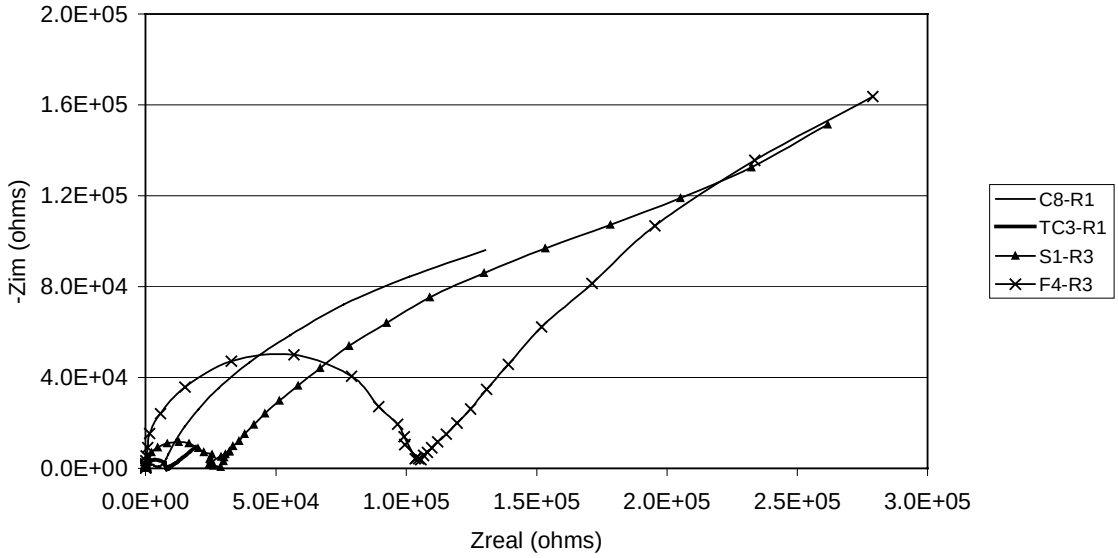

Figure 3.22.- Nyquist plot of one probe at the crack for each type of concrete.

Figures 3.23 presents the Bode plot for the probes at different locations in the case of OPC-TC beam TC4. From this figure can be observed the influence of the exposure conditions of the probes on the Bode plot. As it was expected, the probe at the top showed the highest impedance and the one at the crack the lowest. The same behaviour was generally observed for the other types of concrete. Figure 3.24 shows the corresponding Nyquist diagram for probes 1 and 3 at the crack level. The curves for the submerged and non-submerged probes were not included because the impedances of these probes are much larger than those at the crack. This makes difficult to observe the curves from the probes at the crack. The semicircle at low frequencies is a characteristic of the corrosion process: the diameter representing Rp, the polarization resistance. As can be seen the probe 3 (R3) has a larger semicircle than R1 at low frequency, which is characteristic of the corrosion process. This agrees with the higher corrosion rate obtained for R1 through LPR (see Table B.10).

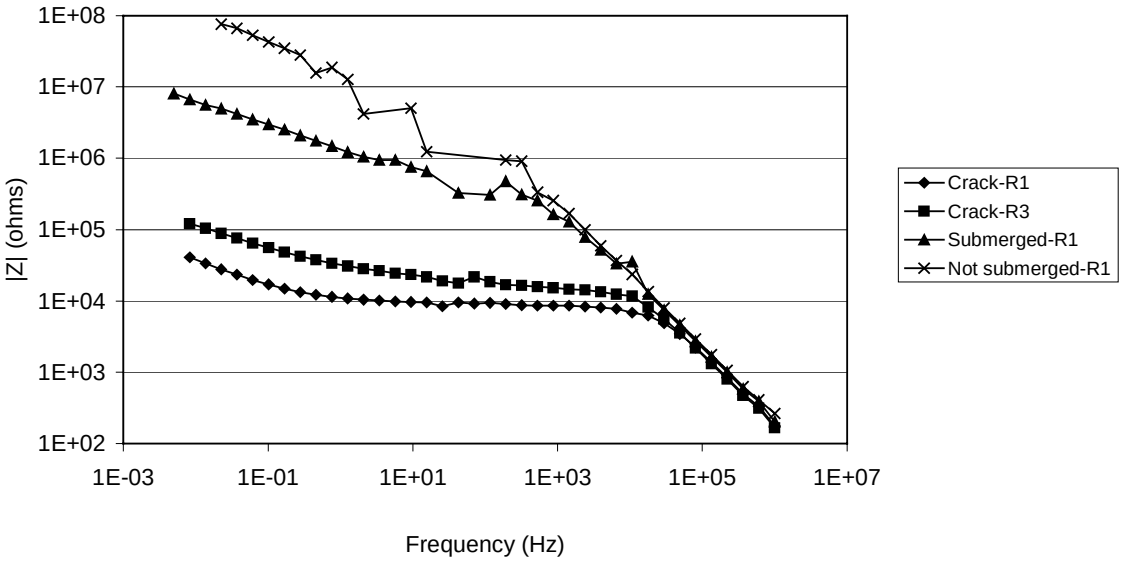

Figure 3.23.- Bode plot of one probe at the three locations in OPC-TC beam TC4.

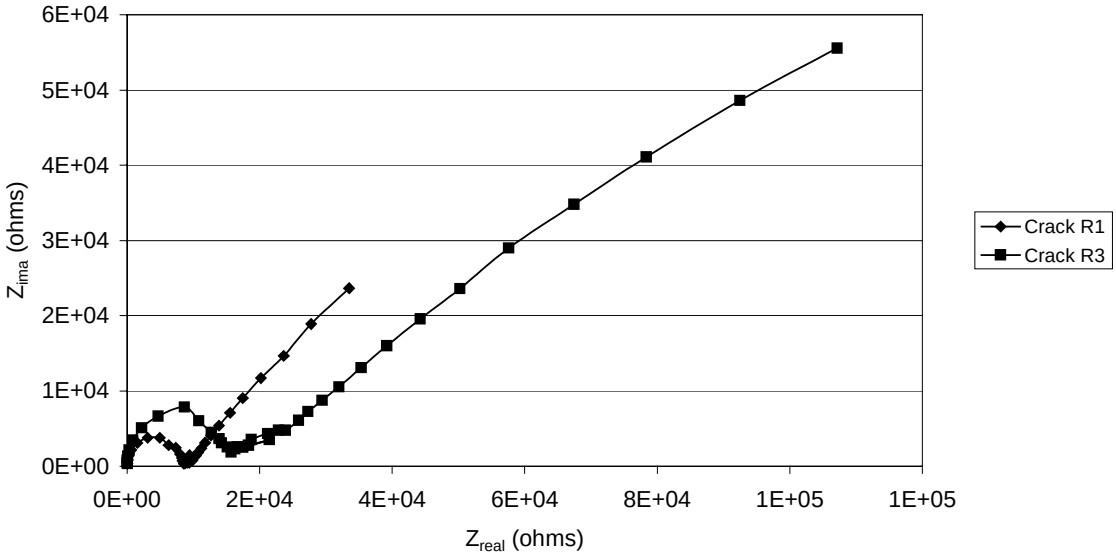

Figure 3.24.- Bode plot of probes at the crack level in OPC-TC beam TC4.

EIS measurements of some beams (on probes at the crack and submerged) were carried out after the two weeks of drying to see if there were significant variations with respect to those obtained after wetting. A great number of the cases analyzed showed the same behaviour. Those that experienced some differences were not consistent between probes of the same beam and at the same location, and between beams of the same concrete.

Other EIS measurements consisted in the use of three electrodes with the objective of studying the position of the reference electrode and the differences with respect to the stainless steel when it is used as both the counter electrode and the reference electrode. For this purpose the embedded ERE and an external SCE were used separately. The measurements using these two electrodes resulted in exactly the same curves. However, compared to the two-electrode configuration using the stainless steel, the Bode plots showed a shift of the curve to lower impedances, whereas the Nyquist diagrams showed a smaller semicircle at higher frequencies. This can be observed on Figure 3.25 where is represented the Bode plots for three types of concretes when the ERE or the stainless steel is used.

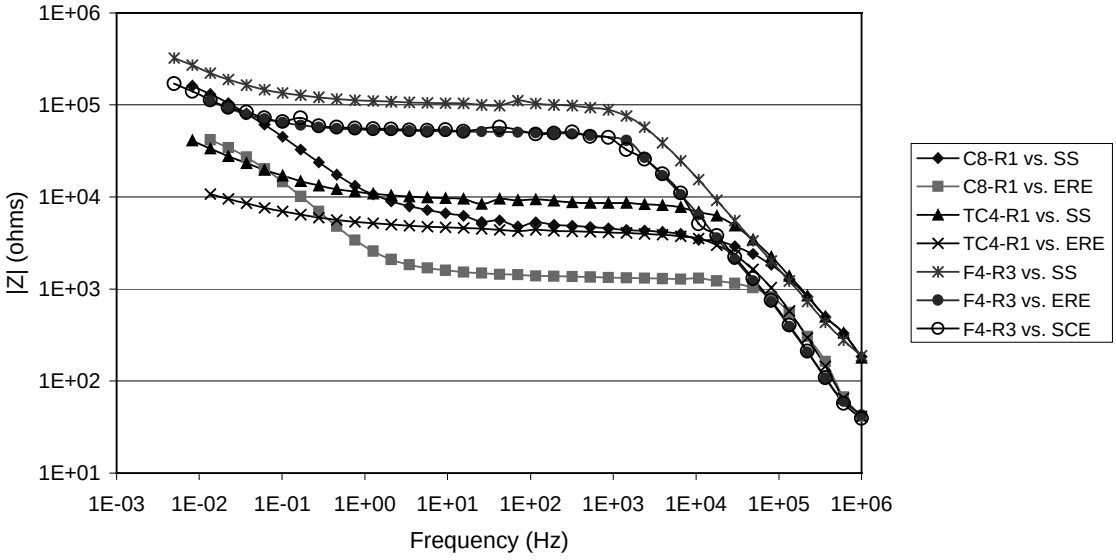

Figure 3.25.- Bode plot of one probe at the crack for different concretes using two- or three-electrode configuration.

The EIS data were fitted to several equivalent circuits. The most appropriate circuit is the one shown in Figure 3.26. Figure 3.27 illustrates an example of the fit to the data for one probe at the crack in HPC-Slag beam S1. The Circuit Description Code used was R(CR)(Q(RW)). Each parameter accounts for the solution resistance (R_e), the capacitance (C_c) and the resistance of concrete (R_c), the constant phase element, CPE, (Q according to the nomenclature used in the software), the polarization resistance (R_p) and the Warburg impedance (W). The constant phase element represents the double layer capacitance, but it does not behave as a pure capacitor which may result from the lack of homogeneity of the metal surface. The values obtained for each parameter are shown below. The curves represent the measured data from EIS (shown as Msd on the graph) and the resulting one from the mathematical fitting for that circuit (Calc). The fitting was made with the software ZsimpWin 3.10 from Princeton Applied Research. The calculated parameters for the chosen equivalent circuit are presented in Table 3.3.

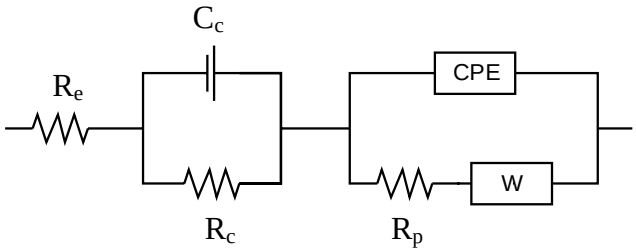

Figure 3.26.- Equivalent circuit used in the mathematical fitting of the EIS data.

Table 3.3.- Calculated parameters for Equivalent circuit in Figure 3.22.

R_e = 38.64 ohms	CPE = 5.76E-5 $S \cdot sec^n$
C_c = 8.52E-10 F	n = 0.6911
R_c = 2.79E+4 ohms	R_p = 11.8E+4 ohms
	W = 1.30E-4 $S \cdot sec^{0.5}$

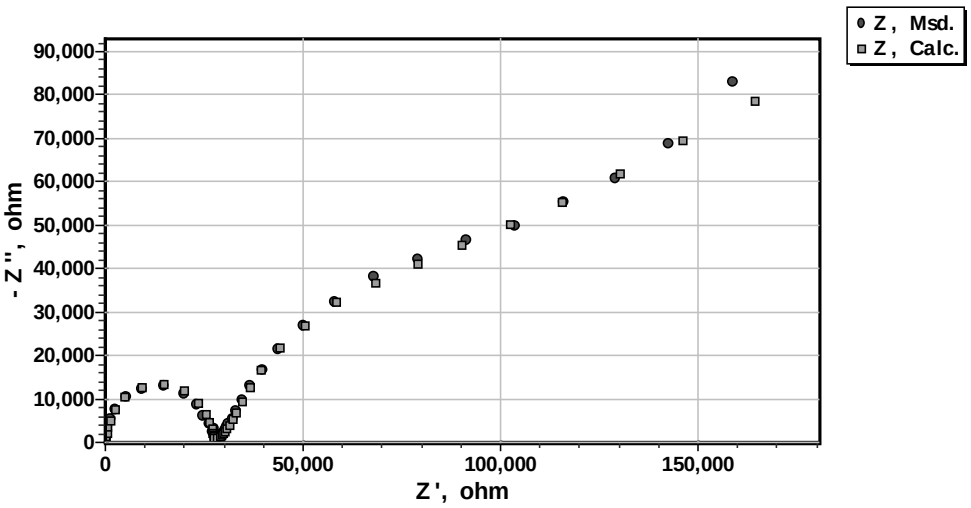

Figure 3.27.- Measured and calculated data from the equivalent circuit fitting for beam S1-R1.

3.2.- Dynamic Beams

3.2.1.- Corrosion Potentials

The corrosion potentials of the carbon steel probes in the dynamic beams are presented in Figures 3.28-3.31. The same analysis was done as in the case of the static beams. In Tables 3.3 and 3.4 are given the potentials of the stainless steel probes used as reference electrodes during the E_{corr} measurements with the DAQ. These values correspond to the period of wetting for two weeks (after 22 weeks in solution) and were the ones used to transform the potential to the CSE scale.

According to Figures 3.28-3.31 the probes at the top are below the corrosion limit established by ASTM for all the beams. Even the submerged probes show relatively high (more positive) corrosion potentials with exception of HPC-Slag beams. In the case of the probes at the crack, the potential has values more negative than -350 mV (vs. CSE) in all four concretes implying active corrosion.

Table 3.4.- Potential of stainless steel and ERE in HPC after two weeks wet.

Level	E_{corr} (mV vs. SCE)							
	F5	F7	F8	F9	S2	S3	S6	S9
Not submerged	-20	4	-14	-5	140	30	-150	139
Crack	-80	-1038	-248	-198	-90	-60	-552	-551
Submerged	-209	-140	-134	-166	-140	-182	-195	-233
ERE	-	-	-	101	-	-	-	78

Table 3.5.- Potential of stainless steel and ERE in OPC concrete after two weeks wet.

Level	E_{corr} (mV vs. SCE)							
	C2	C4	C5	C6	TC1	TC7	TC9	TC10
Not submerged	9	140	75	-130	6	116	-1	7
Crack	-450	-710	-184	-602	-790	-597	-678	-262
Submerged	-170	-167	-131	-123	-128	-118	-84	-110
ERE	-	-	90.9	-	-	-	-	-

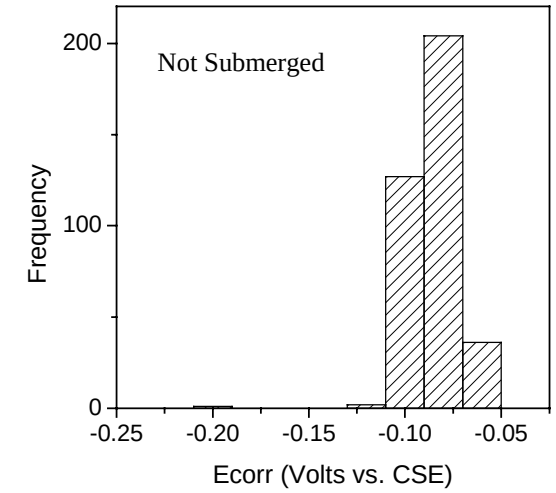

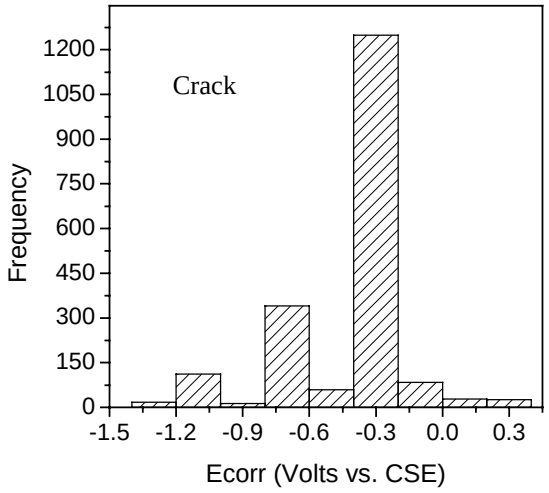

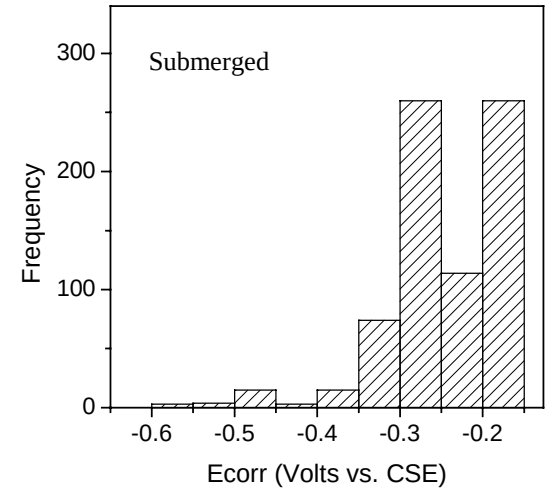

Figure 3.28.- E_{corr} Histograms for dynamic HPC-Fly Ash beams. Frequency refers to the number of measurements.

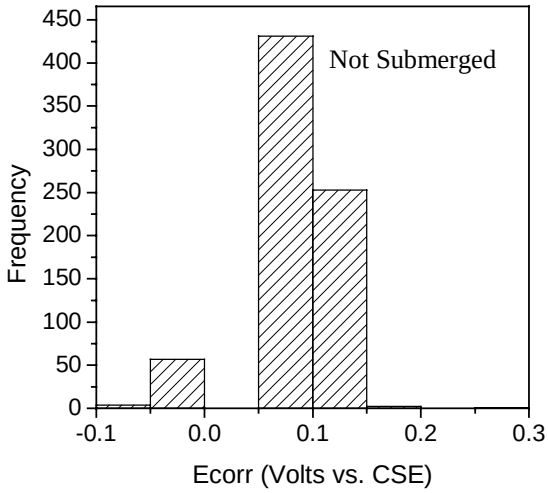

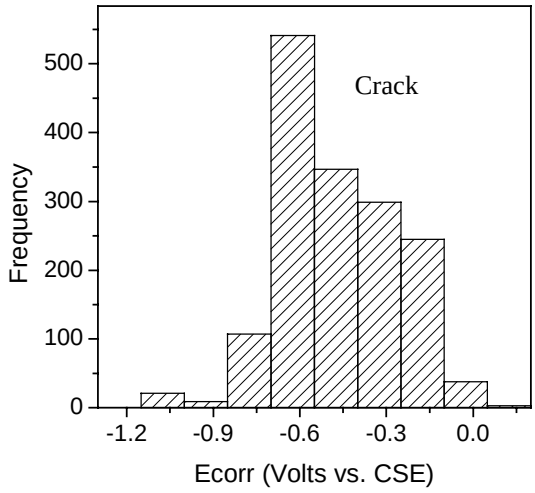

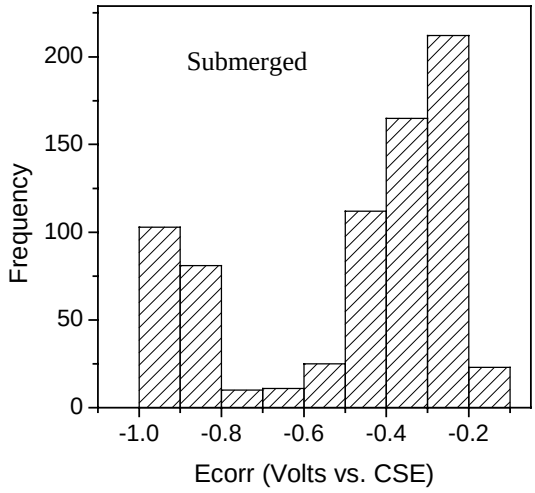

Figure 3.29.- E_{corr} Histograms for dynamic HPC-Slag beams. Frequency refers to the number of measurements.

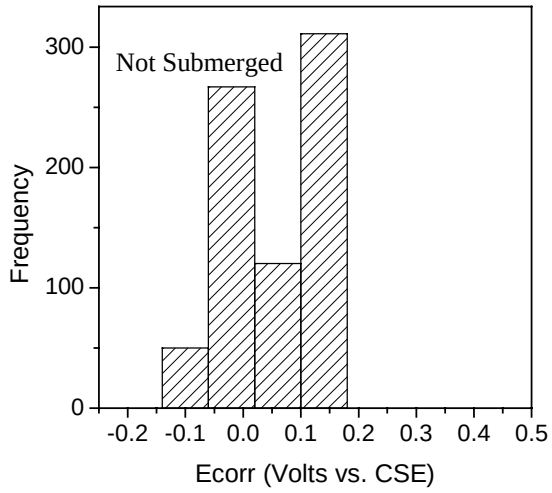

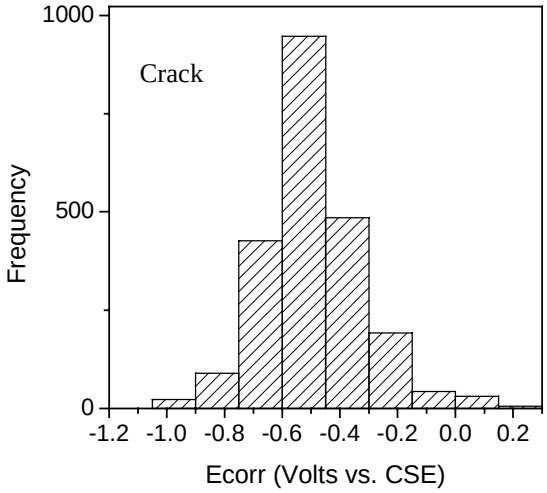

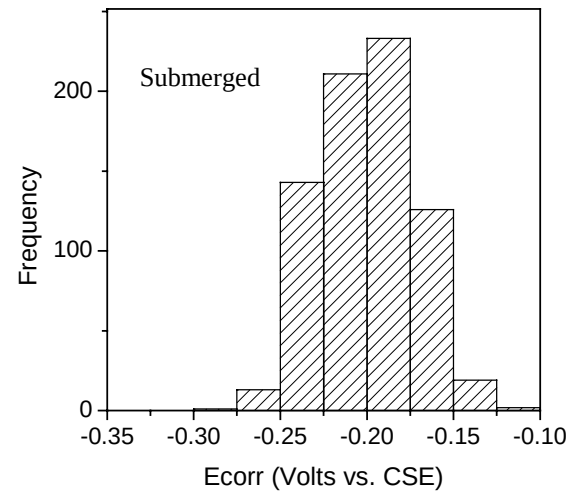

Figure 3.30.- E_{corr} Histograms for dynamic OPC-C beams. Frequency refers to the number of measurements.

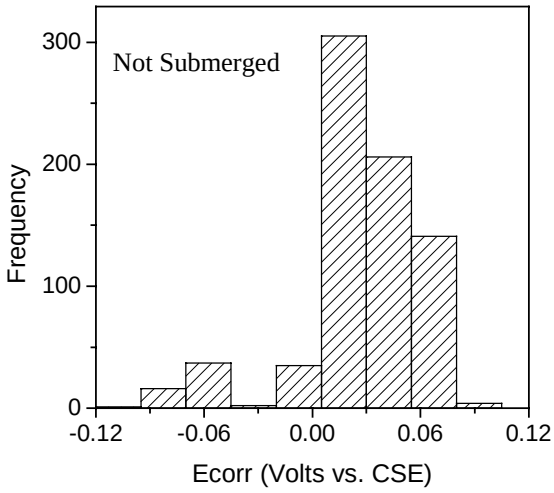

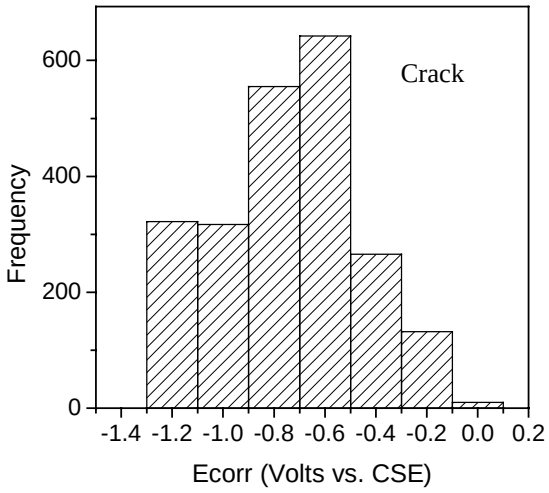

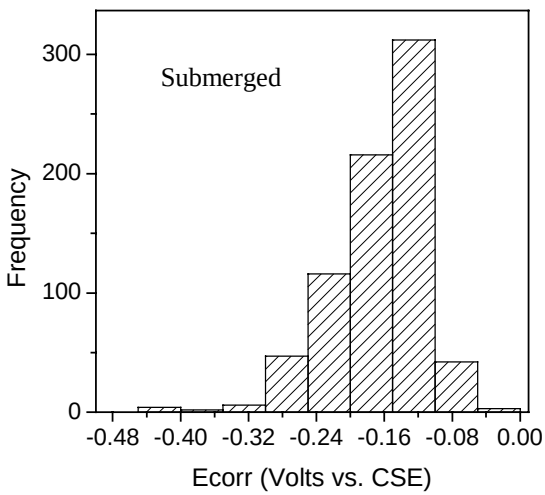

Figure 3.31.- E_{corr} Histograms for dynamic OPC-TC beams. Frequency refers to the number of measurements.

Figure 3.32 pictures the average of the corrosion potential for the measured probes in each type of concrete. Notice that each value corresponds to the average of the E_{corr} for each probe at the crack. According to this figure, the E_{corr} are closer among the different types of concrete. It is noteworthy the very negative values acquired by one of the HPC-Fly Ash beams (F7), which go from -200 mV to around -1200 mV (CSE). However, as can be seen from the histograms the other concretes also show very low corrosion potentials.

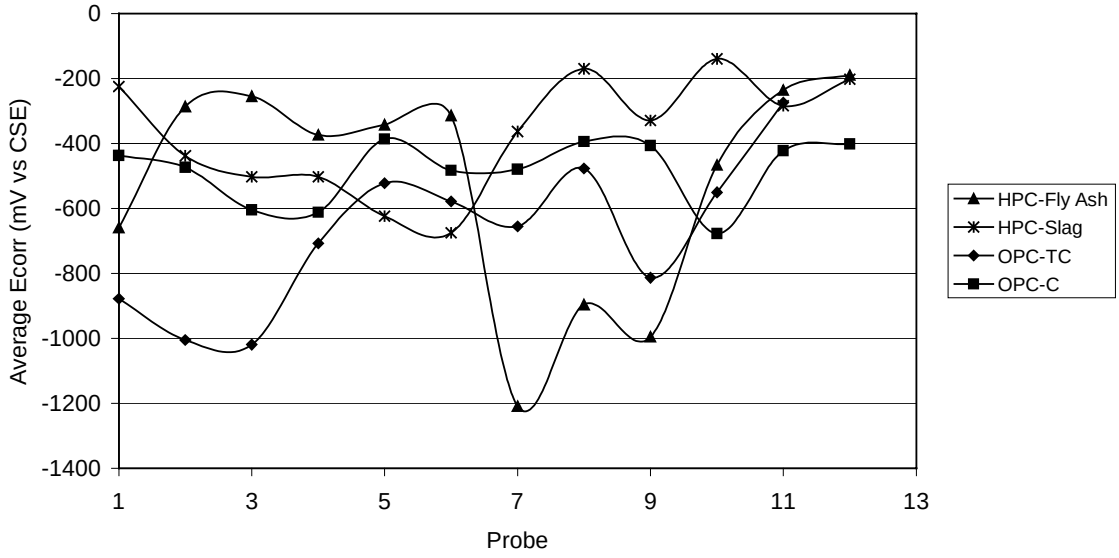

Figure 3.32.- Average corrosion potential for each probe measured at the crack. Each type of concrete is plotted in the following order (3 probes per beam): HPC-Fly Ash (F9, F8, F7, F5); HPC-Slag (S9, S6, S2, S3); OPC-C (C6, C2, C5, C4); OPC-TC (TC9, TC7, TC1, TC10).

Initially the corrosion potential of the corrosion probes was measured twice per day using the DAQ to follow the effect of loading. However, after several months of testing differences were not observed; the values of E_{corr} (versus the stainless steel) were practically the same during loading as when the beams were not loaded. Thus, it was decided to measure E_{corr} (versus SCE) every second for around 13 minutes with and without loading by using the CML to see if there was any effect during this time. For this purpose, the E_{corr} was measured without loading for the first 200 seconds, then the beams were cyclically loaded for other 200 seconds (until 400), afterwards they were statically loaded (by holding the load) for 200 seconds more

(until 600), and finally, the load was removed until the end of the test. Only a small number of probes (including the stainless steel probes) showed slight changes in E_{corr}. The clearest effect was obtained for HPC-Slag beam S9-R3, the result of which can be seen in Figure 3.33, but note that the total potential change was only ~8 mV.

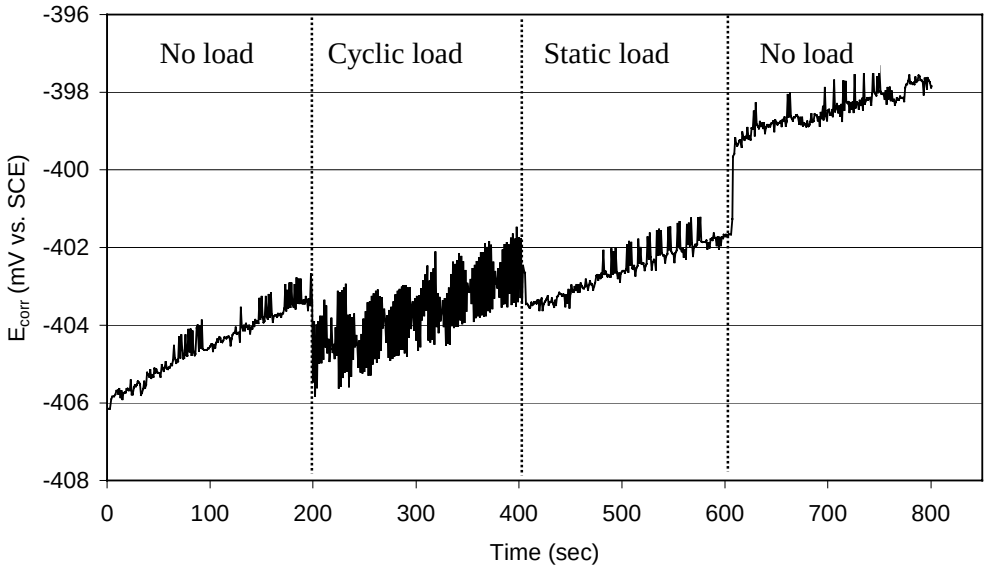

Figure 3.33.- Effect of loading on the corrosion potential of HPC-Slag S9-R3 submerged in solution.

The same test was carried out measuring the potential of the reinforcement cage, formed by two stainless rods and two black steel rebars versus and external saturated calomel electrode (SCE), interconnected by the stirrups. As it was mentioned in the Experimental Procedures wires were attached to both ends of the rebar cage for each beam. Figures 3.34-3.35 illustrate the effect of loading on the corrosion potential of the rebar cage of HPC and OPC beams.

These measurements were performed for both the corrosion probes and the rebar cage, not only during the wetting stage but also when the tanks were empty. The beams that showed variations in E_{corr} during wetting also did when the beams were drying. However, in this case, the E_{corr} was measured versus the stainless steel, which also shifted in some beams throughout the loading scheme followed.

Noteworthy from these figures is the shift in E_{corr} to more negative values as the load is applied. The shift is very small and E_{corr} returns to the baseline very fast. However, the test is run for only a few minutes. It is also worth to note the effect of increasing the load during the static stage, i.e. when the load is held. The load is not intentionally increased but it is just a result of the set-up design: since the cyclic loading is stopped the manifold used to distribute the compressed air to all the beams can reach the maximum pressure.

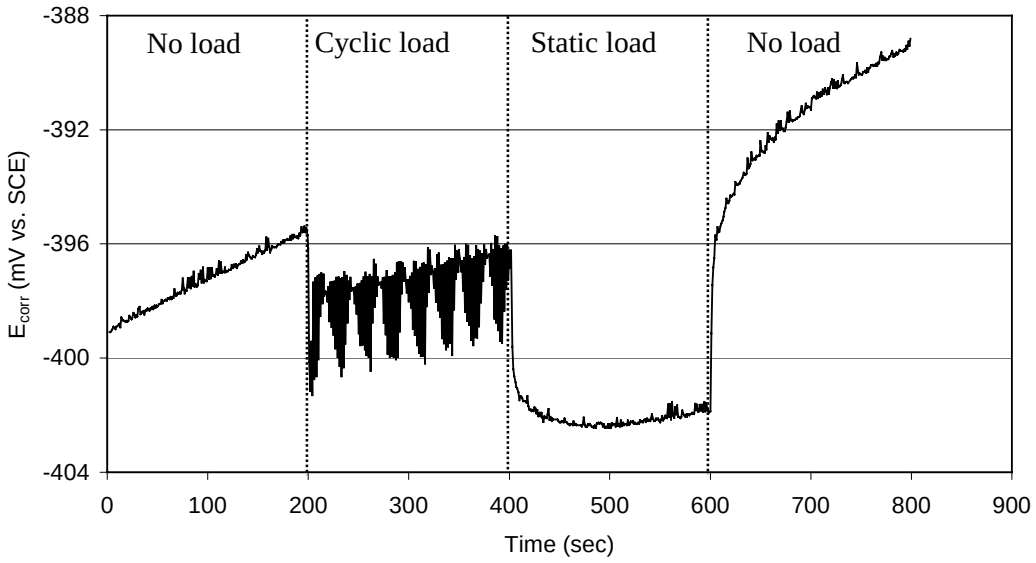

Figure 3.34.- Effect of loading on the corrosion potential of the rebar cage in HPC-Fly Ash F8 submerged in solution.

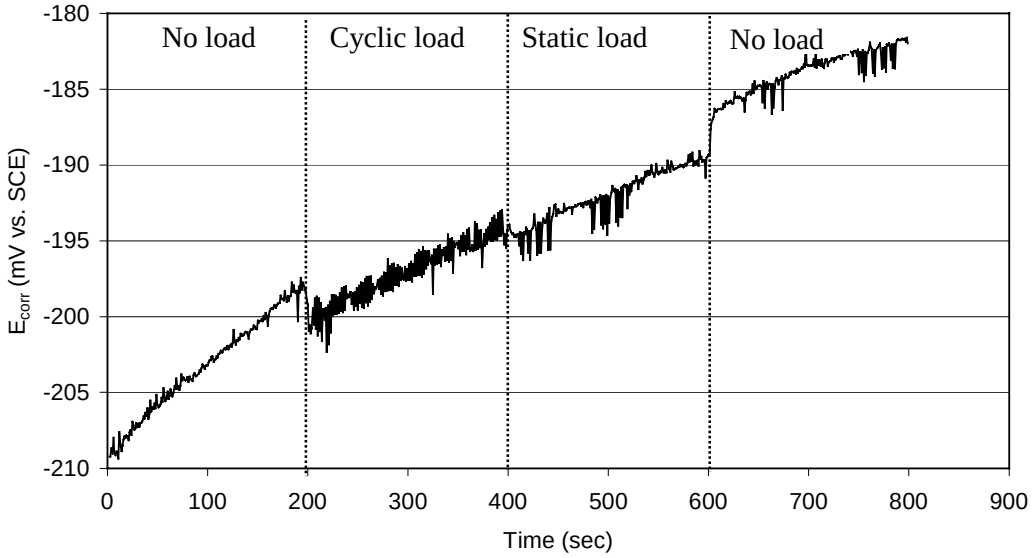

Figure 3.35.- Effect of loading on the corrosion potential of the rebar cage in HPC-Slag S9 submerged in solution.

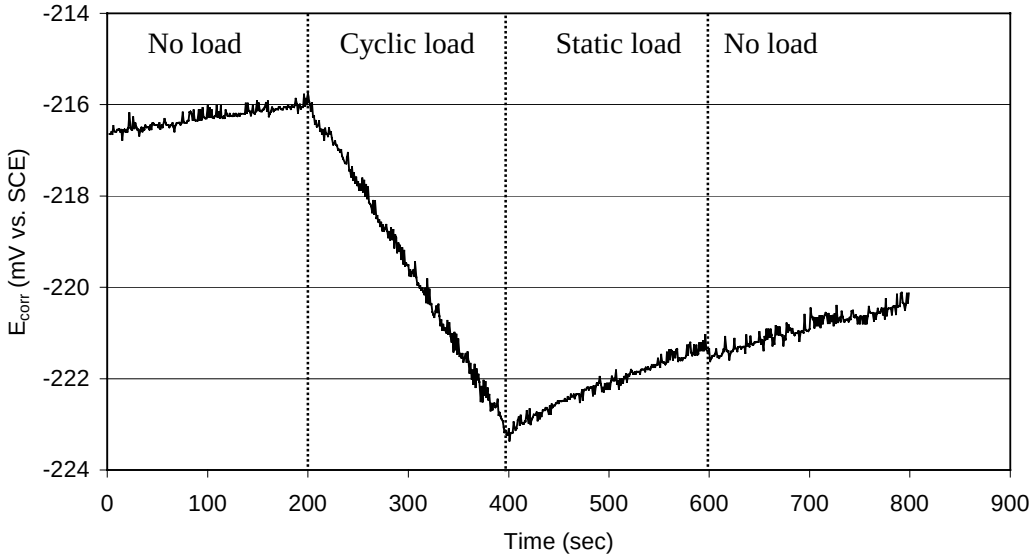

Figure 3.36.- Effect of loading on the corrosion potential of the rebar cage in OPC-C6 submerged in solution.

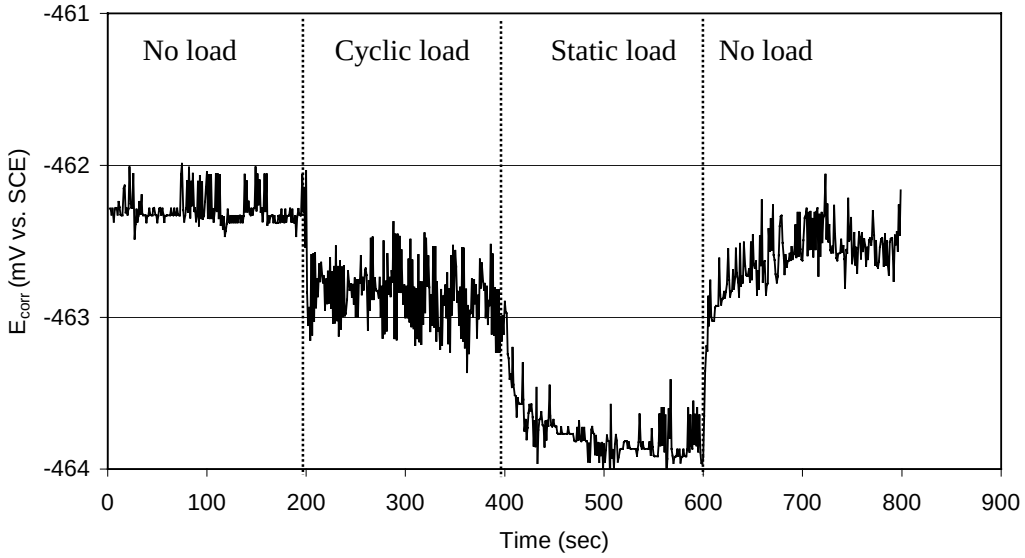

Figure 3.37.- Effect of loading on the corrosion potential of the rebar cage in OPC-TC7 submerged in solution.

3.2.2.- Corrosion rates

The corrosion rates of dynamic beams determined by LPR using the CML are summarised in Figures 3.38-3.45. In this case, fewer measurements were taken than for static beams due to the loading difficulties encountered during the test. Each plot represents the average corrosion rate of the three probes for every beam at the different locations (non-submerged, crack and submerged). Tables C.1-C.12 of Appendix C record the corrosion rates for each type of concrete and corrosion probe. The weeks in solution when the measurements were carried out are also specified on these tables.

The first measurement for all the beams was taken after a week being in solution without loading. However, some loading was necessary before starting the experiment to check if the pistons initially used were working properly. After the second measurement (4 weeks in solution) until the 8^{th} one (22 weeks in solution) the beams were loaded for around 84 hours between measurements. Note that, in some cases, it was not possible to take a measurement after 4 weeks in solution due to the problems described in section 2.6.2. The new loading

system was installed during the 23rd week. The corrosion rate readings during the 23rd and 24th weeks in solution for the beams in one tank (those represented in the first plot for each type of concrete) were made after 90 hours loading between measurements. However, for the rest of the beams in the second tank these readings were made after 267 and 94 hours of loading, respectively, since with this new system all the beams were loaded at the same time, as explained in the section 2.6.2. To this date the dynamic beams have been loaded for around 1000 hours, corresponding to 2.8 million cycles.

Figures 3.38 and 3.39 show the corrosion rates for HPC-Fly Ash beams. As can be seen from these figures the corrosion rates are relatively low, except for the beam F7, which exhibits values between 10-20 μm/year that decrease in time, but start increasing again after installing the new set-up. As it was previously mentioned, these values are characteristic of a system undergoing corrosion considered by some researchers; however, in the interpretation of the results some precaution must be taken. As it was mentioned for the static beams, it should considered that the corrosion at the crack may be very high compared to that of the rest of the probes in this location, due to the fact that one or even two them might be very close to the crack. This can be observed in Tables C.1-C.10 of Appendix C, where the standard deviation for all the values is also tabulated, and in the case of the crack region, it can reach very high values. The consideration applies to all the beams.

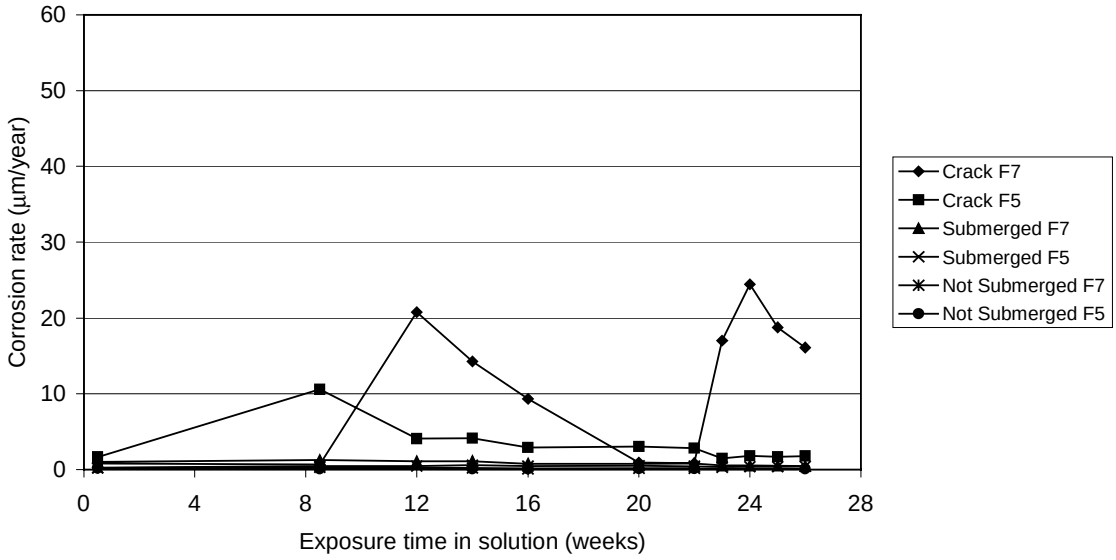

Figure 3.38.- Corrosion rate of HPC-Fly Ash beams dynamically loaded.

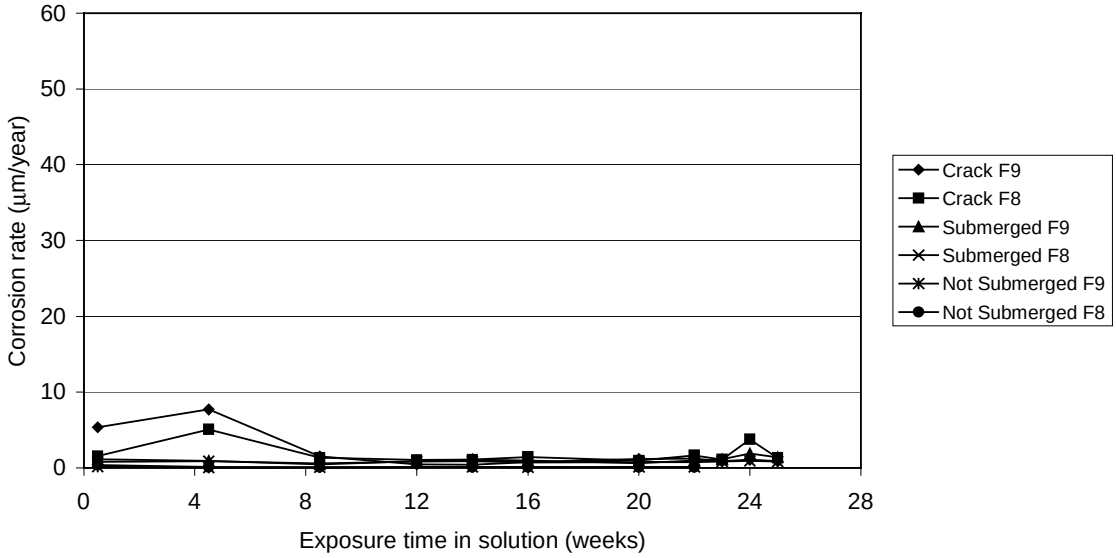

Figure 3.39.- Corrosion rate of HPC-Fly Ash beams dynamically loaded.

The corrosion rates of the HPC-Slag beams are illustrated in the following figures. In this case is possible to see higher corrosion rates than in HPC-Fly Ash beams, especially for beams S9 and S6, which undergo corrosion around the 40 µm/year. An increase of the corrosion rate with the new set-up is also observed.

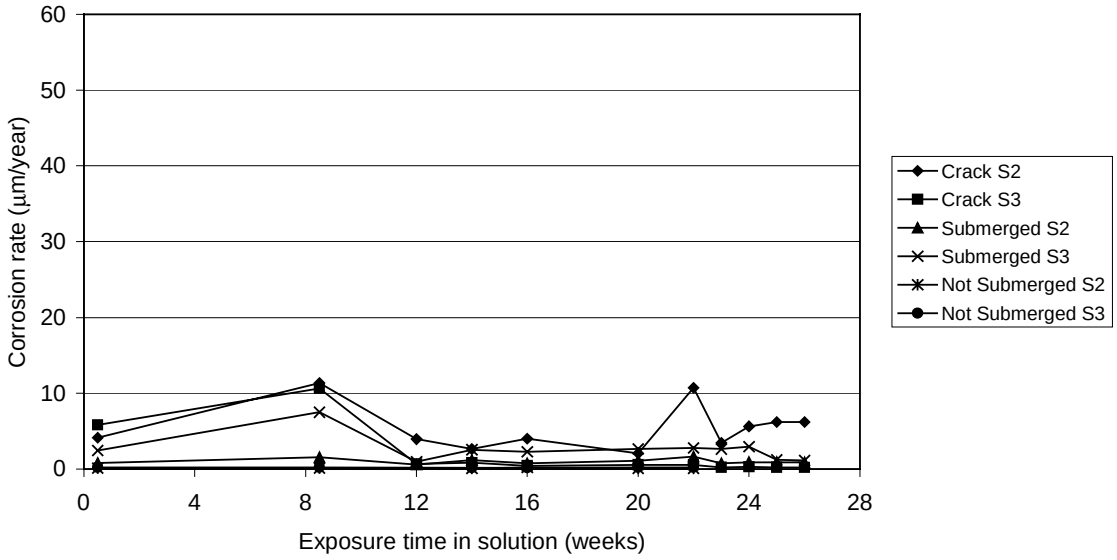

Figure 3.40.- Corrosion rate of HPC-Slag beams dynamically loaded.

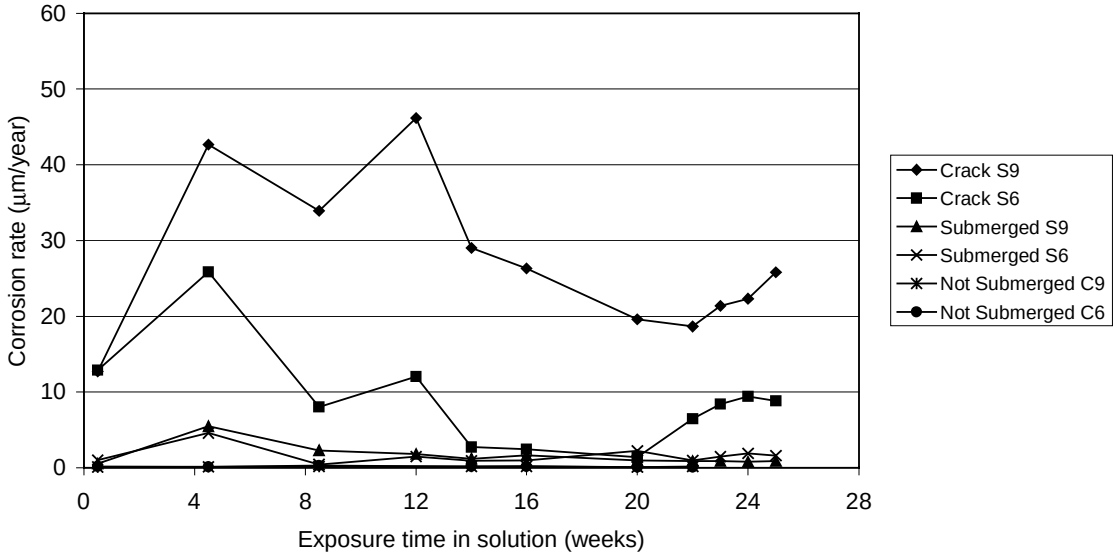

Figure 3.41.- Corrosion rate of HPC-Slag beams dynamically loaded.

Figures 3.42-3.50 represent the corrosion rates obtained for OPC beams. As can be seen from these figures, the OPC-TC beams show relatively higher corrosion rates than OPC-C beams. However, in general, both concretes seem to perform better than the HPC-Slag beams.

Nevertheless, it seems that with the new loading system the corrosion of two beams (C4 and TC1) will keep increasing with the exposure time. Notice from Table C.11 that TC1 at the crack reached a corrosion rate above 200 μm/year after 25 and 26 weeks in solution, but these measurements were not included in the plot since they are off the scale.

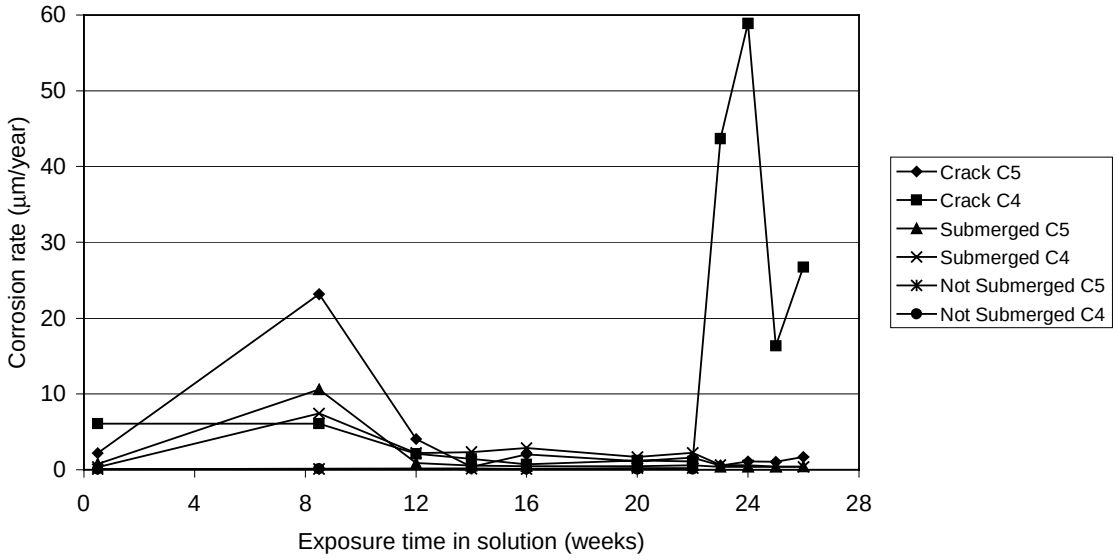

Figure 3.42.- Corrosion rate of OPC-C beams dynamically loaded.

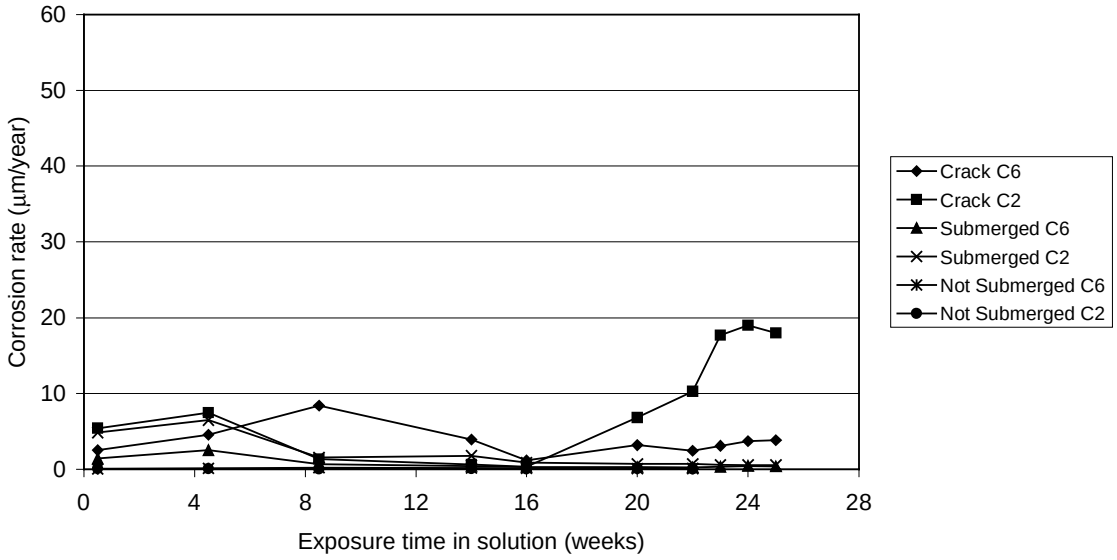

Figure 3.43.- Corrosion rate of OPC-C beams dynamically loaded.

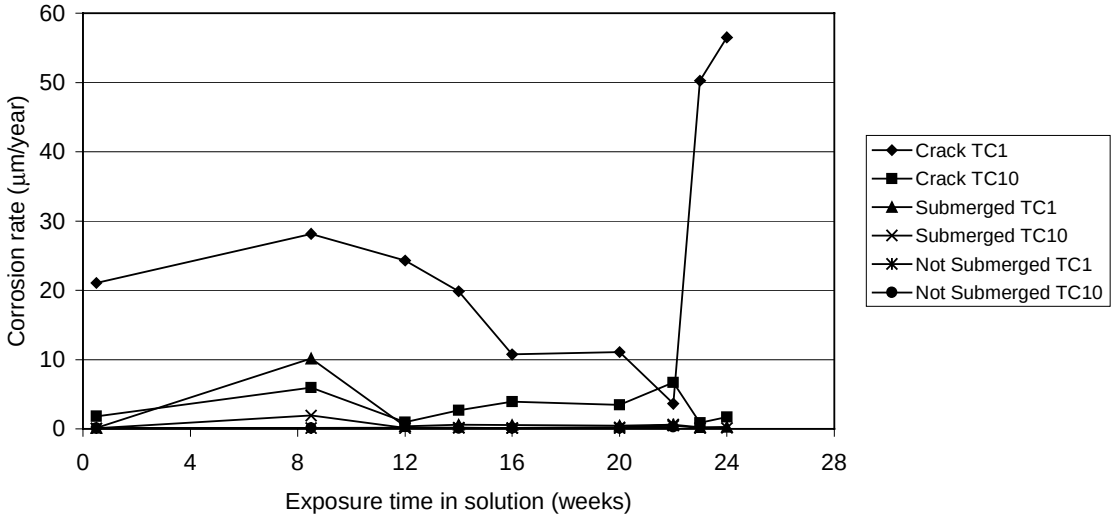

Figure 3.44.- Corrosion rate of OPC-TC beams dynamically loaded.

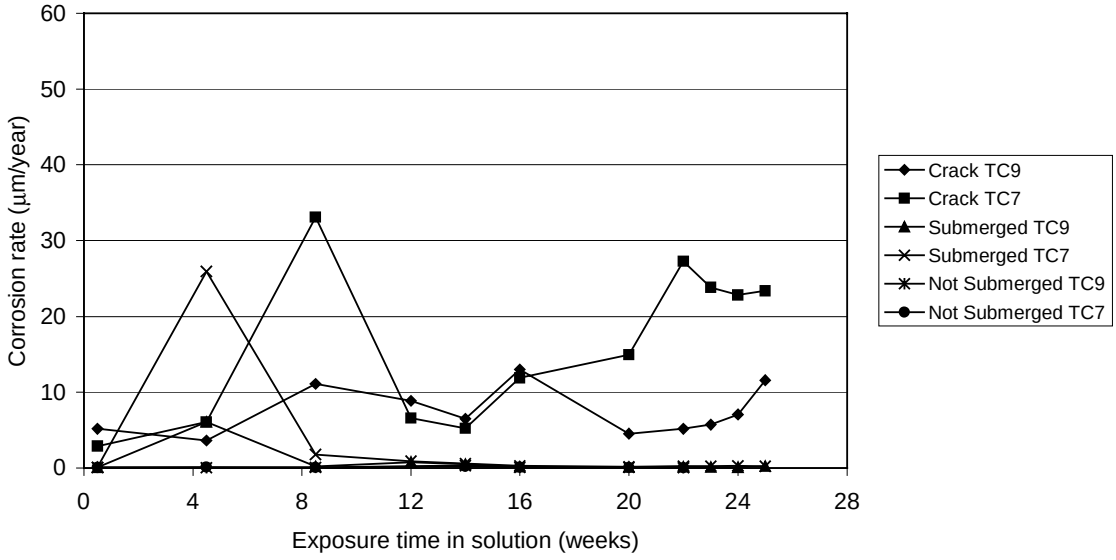

Figure 3.45.- Corrosion rate of OPC-TC beams dynamically loaded.

3.2.3.- Cyclic Polarization curves

Figure 3.46 illustrates the cyclic polarization curves from corrosion probes at the crack in OPC concretes (C4-R1 and TC1-R3), which show high corrosion rates and very negative E_{corr}. The polarization curves were obtained after 26 weeks in solution. The scan was started at E_{corr} raised to +500 mV with respect to E_{corr} and finally it was reversed to the initial E_{corr}. As can be seen from this plot, there is no indication of pits formation in the case of TC1, despite the very high corrosion rate determined by LPR (see Table C.11), but Tafel extrapolation of these curves would give corrosion rate values similar to the LPR values. However, C4 shows an increase in the current that may be associated with its tendency to pitting corrosion.

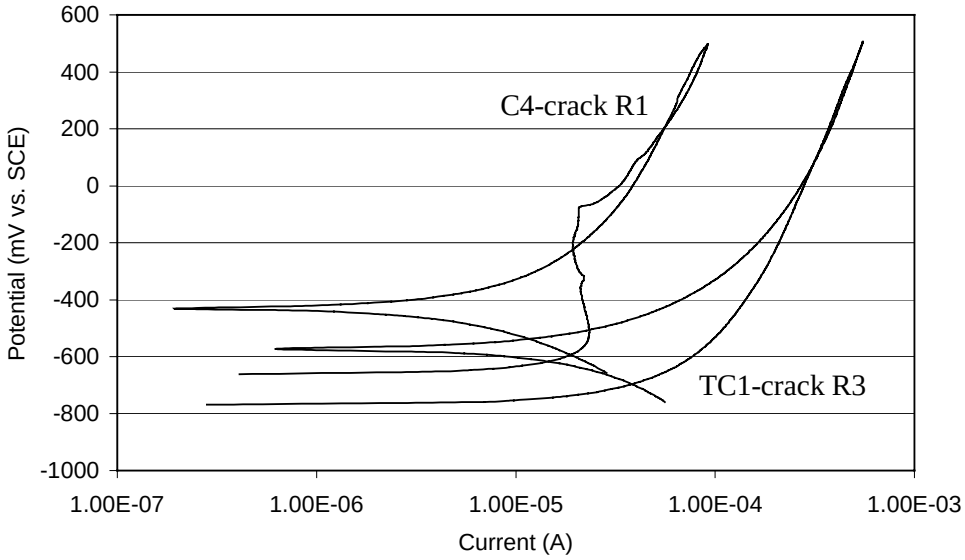

Figure 3.46.- Cyclic polarization curves of corrosion probes at the crack in OPC concretes dynamically loaded.

3.2.4.- Electrochemical Noise

In general, the electrochemical noise measurements of the dynamically loaded beams gave results similar to those obtained for static beams. However, there was less agreement with the

LPR measurements, specifically when the corrosion determined by the LPR method was compared to the average current noise. Thus, a higher ECN for the submerged probes than for the probes at the crack does not always correlate with a higher corrosion rate determined by LPR.

A different result from the noise measurements was obtained for probes in OPC-C (beam C5) and it is summarized in Figures 3.47 and 3.48. As can be observed from these figures a perfect correlation exists between ECN and EPN after 14 and 16 weeks in solution (336 and 420 hours of loading, respectively). This behaviour is repeated at longer exposure time but only in the case of C5.

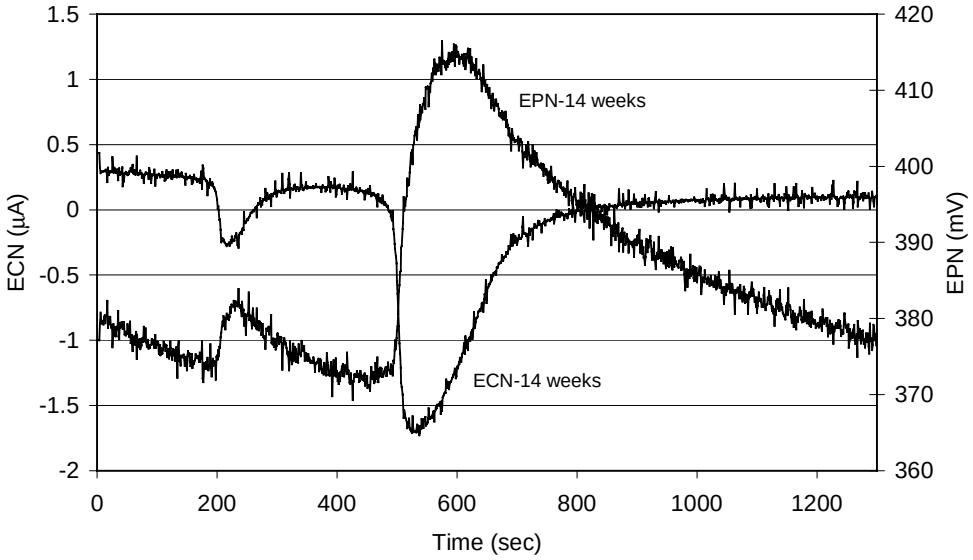

Figure 3.47.- ECN and EPN of corrosion probes at the crack in OPC-C5 after 14 weeks in solution and 336 hours of cyclic loading.

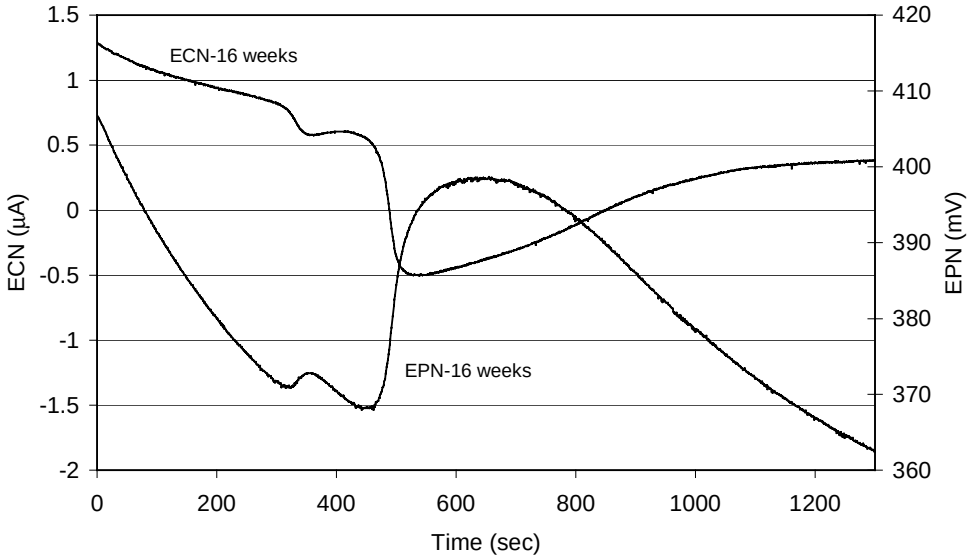

Figure 3.48.- ECN and EPN of corrosion probes at the crack in OPC-C5 after 16 weeks in solution and 420 hours of cyclic loading.

4. Discussion

The corrosion behaviour of static and dynamic beams is discussed in the following section, based on the results previously presented. The results are discussed separately for both static and dynamic beams, and finally a comparison between them is made.

4.1.- Statically loaded Beams

The results clearly indicate that the corrosion potential of the stainless steel, taken as the reference electrode, changes with the exposure time. This can lead to a misinterpretation of the corrosion potentials of the carbon steel probes if these changes are not taken into account. However, only a few stainless steel probes (6 out of 48) showed major variations during the testing period. Thus, it is possible to use the stainless steel as reference electrodes and have an idea of the corrosion potential of the reinforcing steel probes.

According to the corrosion potential measurements (Figures 3.1-3.4), the probes at the top (non-submerged in the solution) show the most positive and steady corrosion potentials, whereas the probes at the crack have the most negative values, for the four concretes studied. This behaviour was expected since at the top the probes are never in direct contact with the chloride solution. On the other hand, the probes at the crack are not only in direct contact with the solution but also the crack path allows the corrosive agents (water, chloride ions and oxygen) to be transported easily until the surface of the corrosion probes. As a result the probability of corrosion of the probes at the crack level is higher, even though they might not intersect the crack.

The corrosion potentials of the submerged probes lie between those at the crack level and those at the top. In this way, the probability of corrosion under such conditions should be lower. The corrosion of the probes under these conditions may be controlled by the diffusion of the corrosive species to the metal.

The histograms of E_{corr} presented in Figures 3.1-3.4 illustrate that the non-submerged probes in all the concretes have a probability of corrosion below 10%, according to the ASTM standard (C 876-87). Even in the case of the submerged probes the probability of corrosion is low since most of the values are more positive than -350 mV (vs. CSE).

On the other hand, it is expected that the corrosion of the probes at the crack, mainly for OPC beams (both C and TC), is higher since the corrosion potentials are mostly more negative than -350 mV (CSE). It is noteworthy that HPC-Slag beams display the most positive values, which are in the same range of those under submerged conditions. In the case of HPC-Fly Ash beams, it can be seen that the major proportion of the corrosion potentials are more positive than -350 mV (vs. CSE), while some have very negative potentials indicative of corrosion according to ASTM. A summary of this is presented in Figure 3.6, where the average corrosion potentials of the probes at the crack are plotted. From this figure can be observed the very negative values of E_{corr} for the OPC beams. Another important point from this figure is the great variation among beams of same concrete, as well as among probes in the same beam due to the presence of the crack (additional cracks are possible), which could reach or pass close to one or two of them. This high variability is also reflected in the histograms. It should be kept in mind that these values were determined relative to the potential of the stainless steel only after two weeks in solution; the potential during dry conditions was not considered.

Thus, according to the E_{corr} values, the probes in OPC beams (both C and TC) should be undergoing active corrosion at the crack region under the conditions tested. The probes in most of the HPC beams still show more positive corrosion potentials, although a number of values from HPC-Fly Ash beams fall below the -350 mV (vs. CSE).

Regarding the corrosion rate measurements (Figures 3.7-3.14), it is observed that under submerged and non-submerged conditions the values are very close for all the concretes. The probes in HPC-Fly Ash beams show slightly lower corrosion rates than those in OPC concretes. The probes at the crack in OPC beams undergo the highest rates, whereas those in the HPC-Fly Ash beams show very low values during almost the entire period. The corrosion rates of HPC-Slag beams are slightly higher than those in the Fly ash beams, even though the

latter present more negative corrosion potentials in some cases. Comparison between both OPC beams clearly shows the higher corrosion of OPC-TC beams, with the exception of beam C10. The high corrosion in the latter may be due to the double induced cracking of the beam.

The low corrosion rate experienced by steel embedded in the HPC beams is the result of the blocking of the diffusion path. As was mentioned in the Literature Review, the use of supplementary cementitious materials, such as slag, fly ash and silica fume reduces the porosity of concrete. This reduction in the porosity is related to the pozzolanic reaction between the calcium hydroxide and these materials, forming more C-S-H. In this way, the additional C-S-H blocks the path to diffusion of corrosive species and absorbs more free chlorides. The high content of Al_2O_3 (Table 2.1) in Fly ash may also influence in the reduction of the corrosion as a result of the formation of chloroaluminates, which leads to a decrease of free chlorides in the pore solution. Moreover the water/cement ratio of OPC concretes (0.43) is considerably higher than that of HPC beams (0.35). It is a well-known fact that the higher the water/cement ratio the higher the porosity of the concrete.

It is worth noting that the corrosion rate in HPC at the crack is lower than in OPC concretes even though the crack path in HPC is less tortuous than in OPC concretes. It was expected that a more direct path in HPC beams would allow the corrosive agents to reach the metal surface easier and cause higher localized corrosion. The continued pozzolanic activity of Fly ash and slag may cause the self-healing of the crack and then reduce the ingress of the corrosive species. The high resistivity of HPC may also limit the spread of the corrosion along the steel surface.

As can be seen from these data, the results of the corrosion potential measurements agree generally with the values of the corrosion rates. According to Figures 3.7-3.10 the average corrosion rates of HPC concretes are below the limit (around 10 μm/year) proposed in the literature as characteristic of high corrosion. This agrees with the predicted low probability of corrosion based on the values of the corrosion potentials and those established in the ASTM standard. Only a few values from the probes at the crack are over this limit for HPC-Slag beams at the beginning of the test, which is also reflected in the high value of the standard

deviation (Tables B.2 and B.4). These high corrosion rates can be the result of the proximity of the probes to the crack tip. However, as time goes on, the corrosion decreases, which may be due to the sealing of the crack as a consequence of the continuing hydration of cement and the pozzolanic reaction or by corrosion products. As it was mentioned above, some of the probes in HPC-Fly Ash beams have corrosion potentials more negative than -350 mV (vs. CSE); however, the corrosion rates are lower than in other cases that have more positive potentials. This lack of correlation may be associated to the influence of other factors in the corrosion rate, such as the formation of corrosion products.

The probes in OPC-C beams (Figures 3.11 and 3.12) also show average corrosion rates that are generally low. Only the beam C10 presents a high value, but this may be due to the accidental double induced crack, as was previously pointed out. It can be seen from Table B.8 that the maximum values (around 25 μm/year) obtained at the crack corresponds to C10. However, in the case of OPC-TC beams one probe of three of the four beams exhibited high corrosion rates (Table B.11). An increase in the corrosion rate can also be observed from Figures 3.13 and 3.14. The fact that these beams were cast and stored outdoors during the winter may be the reason for these high corrosion rates. It is well known that freezing/thawing cycles can cause microcracking of the cement paste. The formation of microcracks will then facilitate the diffusion of the corrosive species.

It is evident from the results that the corrosion rates of the non-submerged and even the submerged probes are still very low for all the concretes. This is in agreement with the corrosion potential values.

The measurements of the corrosion rates in a two-electrode configuration using the Potentiostat/Galvanostat ParStat 2263 confirmed the results obtained with the CML. As was shown in the Experimental Results section, there is a very good agreement between both systems. The high resistance of concrete made it difficult to obtain good measurements using IR compensation using a three-electrode configuration cell. The objective of this test was to determine the effect of the ohmic resistance on the corrosion rate value. As it will be shown

later from the impedance measurements, it seems that the ohmic resistance is very low compared to the concrete and polarization resistances.

It was also found that the area of the working electrode may be very important in determining the value of the corrosion rate, specifically when the cathodic area is much larger than the anodic one (as it is normally found in practice). An increase in the cathodic section (by attaching a stainless steel rod to the corrosion probe) resulted in an increase of the corrosion rates, considering the polarized area the same as the original area.

The corrosion rates after a period of two weeks in solution were generally similar to those obtained during the following two weeks drying. This might indicate that the internal moisture content of the concretes is not significantly affected during the wetting and drying cycles after several months of exposure to the solution.

The polarization curves (Figure 3.16) from two of the most corroded probes at the crack in OPC beams did not show any indication of pitting corrosion. However, the electrochemical noise technique was able to detect, in another OPC beam, some spikes in the ECN curves (Figure 3.20), which might be due to the initiation of pitting, although they may also originate from crevice corrosion. These peaks did not show up in the subsequent measurements probably due to repassivation or general corrosion. The practically constant immersion of the beams in a solution with a pH around 9 may prevent the formation of a passive layer on the metal surface or its repassivation. This would result in a more generalized corrosion instead of pitting corrosion. The reduction in the pH can also result in the release of bound chlorides and take part in the corrosion process. According to Glass et al. (2000), re-solution of chlorides may occur even at pH values above 11, which is very high compared to that one required to provoke the dissolution of the passive layer.

Nevertheless, the immersion of the beam in the solution may have an opposite effect as well. Since there is an equilibrium between the solution and the components of the concrete, $Ca(OH)_2$ will stop leaching out. In this way the rest of the components of concrete will also be

protected from the action of the water (solution). On the other hand, the hydration of the cement will keep proceeding.

The Electrochemical Noise technique also helped to validate the corrosion data and was able to distinguish the differences between the corrosion rates of the probes at the crack and submerged, especially in those cases where the latter show slightly higher values (obtained by LPR).

The use of the Electrochemical Impedance Spectroscopy (EIS) technique revealed, in some cases (F4 and S1), the control of the corrosion by diffusion, which is characterized in the equivalent circuit by the Warburg impedance and the appearance as a 45^{o} line in the Nyquist diagram at low frequencies. This could explain, for instance, why the corrosion rate of HPC-Fly Ash beams is lower compared to the rest of the beams, even though the corrosion potentials are more negative. However, diffusion control is not always observed even for probes in the same beam and location probably due to the heterogeneities of the concrete.

The EIS data was fitted to a circuit consisting of the solution resistance (R_e), the capacitance (C_c) and the resistance (R_c) of the concrete, a constant phase element (CPE), which represents the double layer capacitance, the polarization resistance (R_p) and the Warburg impedance (W), representing the diffusion control. The corrosion rate obtained by LPR is very similar to that one derived from the R_p determined by EIS for S1-R3. The fact that the corrosion rates from both systems are very similar demonstrates that the ohmic resistance does not affect significantly the value of the R_p determined by LPR and hence the corrosion rate. The lower concrete resistance and higher corrosion rate of the probes at the crack level than at those at the top and submerged, is also confirmed by EIS (Figures 3.23 and 3.24).

The lack of significant differences between most of the concretes when they are wet or dry was also proven by this technique. The use of a three-electrode configuration instead of using two electrodes resulted in a shift of the Bode curves to lower impedances and a decrease of the semicircle at high frequencies in the Nyquist plot (Figure 3.25). The EIS measurements with an internal (ERE) or external reference electrode (SCE) produced identical results.

4.2.- Dynamically loaded Beams

As can be seen from Figures 3.28-3.31, the corrosion potentials of the non-submerged and submerged probes are below the limit for high probability of corrosion for most of the beams with the exception of HPC-Slag beams (mainly S6) under submerged conditions. The corrosion potentials of the submerged probes in S6 were measured versus the SCE. The very negative value of probe R1 was confirmed (-835 mV vs. SCE or -907 mV vs. CSE); however, the other two probes showed values around -150 mV (vs. SCE) or -202 mV (vs. CSE). Thus, the probe R1 is in the range of high probability of corrosion, whereas the other two are below the limit of low probability. This low value of E_{corr} for probe R1 may be due to trapped water in an isolated void close to the probe surface. One of the submerged probes in one beam of HPC-Fly Ash also showed E_{corr} more negative than -350 mV (vs. CSE).

Regarding the probes at the crack level, the OPC beams have the most negative E_{corr} values, which are more negative than -350 mV (vs. CSE), the limit for high probability for corrosion according to the ASTM standard. The OPC-TC beams seem to be more active than the OPC-C beams, while the HPC-Slag beams present more negative values than HPC-Fly Ash.

As Figure 3.32 illustrates, the average of the corrosion potentials from the probes at the crack is relatively close for all the concretes. Only in two cases, there exists a significant difference in these potentials, although they correspond to the same beams (TC9 and F7, respectively). This figure also illustrate how the average potentials differ for the same type of concrete.

As it was pointed out in the previous section, the corrosion potential readings were initially made twice per day to follow the effect of loading on E_{corr}. However, major differences between the unloaded and loaded conditions were not observed. For this reason the measurements were performed using the CML, which enable readings to be taken every one second. Figures 3.33-3.37 represent the variations of E_{corr} (vs. SCE) with the loading conditions. Figure 3.33 corresponds to E_{corr} of the corrosion probe at the crack versus an external SCE. Very few probes (4 out of 16), including the stainless steel, presented this behaviour.

On the other hand, the potentials of the rebar cage shifted in most of the cases analyzed (Figures 3.34-3.37). These figures reveal a shift of E_{corr} toward more negative values during cyclic loading. When the load is held constant, that is, the beams are kept statically loaded, the potential stays around the same value reached during the cyclic loading, although less noisy. The small difference between the cyclic and static (constant load) loading stages observed in the plots is due to an increase of the load (from 80 to 100 psi), as was explained in the section 2.6.2. Once the load is completely removed, the potential reverts relatively fast to the original baseline. Although the variations in the potential are not really significant and E_{corr} returns quickly to its initial value on the removal of the load, this could have important consequences in the corrosion of the reinforcing steel. In practice, concrete structures can be subjected to greater loads and for longer periods of time. One possible cause of these changes in E_{corr} to more negative values might be related to the stress concentration on the metal surface near the bending site, so that the probability of corrosion is increased. It should be remembered that this effect is observed both under wetting and drying conditions. Nevertheless, a more detailed study is necessary to find all possible causes responsible for this behaviour.

From Figures 3.38-3.45 is clear that, under dynamic loading, the average corrosion rates of the probes at the top and bottom of the beams are very low. This was expected since, at these locations, the loading should not affect the corrosion mechanism of the probes. In the case of the probes at the crack, can be seen that one pair of each type of concrete undergoes low corrosion rates but in the other one they are relatively higher. Apparently the HPC-Slag beams, particularly the beam S9, is having higher corrosion than Fly ash concrete and even than OPC beams during some time. However, after 14 weeks the corrosion decreases and then starts increasing again with the use of the new loading system. This behaviour is also observed in the OPC concretes. The fact that several beams experienced an increase in the corrosion rate after installing the new set-up suggests that probably some of the original pistons were not reaching the desired crack opening displacement.

The values of the corrosion rates for each probe embedded in the four concretes at different locations are collected in Tables C.1-C.12. Tables C.2, C.5, C.8 and C.11 present the corrosion rates of the probes at the crack for HPC-Fly Ash, HPC-Slag, OPC-C and OPC-TC,

respectively. Note from these tables the large values of the standard deviation, due to the high corrosion rates of a relatively small number of probes, whereas the rest show passive corrosion. These high values should correspond to the closest probe to the crack path. The differences in width, pattern and location of the crack (with respect to the probes), as well as the blocking of the steel surface by the aggregates (this apply for all exposure conditions), may also be some of the causes for disparity in some of the results. As was mentioned in the section 2.7, the crack width of most of the beams was around 0.1 mm; however, that in HPC-Slag beam S9 had a width ~0.5 mm. The larger crack width of S9 can be the cause for the high corrosion rates of the probes at the crack. The vertical location of the crack in some beams differs by more than 100 mm between each other.

After 25 and 26 weeks in solution, the corrosion rates of C4 and TC1 are very high (Tables C8 and C.11, respectively), although the former shows a reduction with respect to the two previous weeks. The beam TC1 exhibits a consistently high corrosion rate, reaching values above 200 μm/year (not plotted in Figure 3.44). The opening of the induced crack and microcracks, which may have formed by freezing/thawing cycles during the initial two months of outdoor exposure, could be some of the reasons for this high corrosion rate. However, the possible formation of secondary cracks during induced cracking, which may also be present in other beams can not be disregarded. This latter statement might explain why in some cases the probes R1 and R3 show much higher corrosion than probe R2, even though they are not adjacent.

According to Tables C.6, C.9 and C.12 the average corrosion rates of the submerged probes in HPC-Slag beams are slightly higher than those in OPC concretes. A possible explanation to this particular behaviour could be based on a dominating effect of the lower pH of the pore solution in the HPC beams as a consequence of the pozzolanic reaction. The low pH of the solution (around 9) may also enhance the effect of the pore solution pH. This would result in a reduction of the stability of the passive layer and/or a decrease of the necessary chloride concentration to break it down. The formation of microcracks at early ages can also be a reason for this behaviour.

In general, there is a good agreement between the corrosion potentials and the corrosion rates determined by LPR. In most of the cases is observed that the more positive the potential, the lower the corrosion rate. Thus, the OPC concretes, which show the most negatives potential at the crack, also undergo the highest corrosion rate. The only clear exception to the latter statement is the beam S9, which experiences a very high corrosion due to a larger crack width, as was previously mentioned. The immersion of the beams in the solution chloride affects the OPC beams more than the HPC beams. The chlorides cause the leaching of the calcium from the main components of the concrete ($Ca(OH)_2$ and C-S-H). However, it has been reported that silica fume seems to prevent calcium leaching (Delagrave et al. 1996).

As it was pointed out above, the submerged corrosion probe R1 in beam S6 presented very negative corrosion potentials, and very high corrosion rates than the other two probes under the same conditions. However, despite the E_{corr} of this probe being more negative than those at the crack, the corrosion rates of the latter are much higher. This could be due to a lower diffusion rate of oxygen through the concrete under submerged conditions. It is well known that when the concentration of oxygen is depleted, the reinforcing steel can develop very negative corrosion potentials, as in the case of submerged structures. This supports the abovementioned as for the low E_{corr} may be a result of trapped water close to the metal surface, where the oxygen diffusion is restricted.

On the other hand, the corrosion probes at the crack in beam F7 have very negative potentials and undergo corrosion rates (the highest among the HPC-Fly Ash beams) that reach values around 20 μm/year. In this case, the oxygen diffusion should not be a limiting factor. Internal additional cracks during induced cracking and the formation of microcracks, due to shrinkage of the cement paste, might be the reason for the relatively high corrosion of the three probes in this beam.

The Cyclic Polarization curves (Figure 3.46) of one of the probes at the crack in beams C4 and TC1 showed some differences regarding their tendency to pitting corrosion. Whereas TC1 practically did not show any tendency to undergo pitting, C4 seems to be more susceptible to this form of corrosion. C4 (rebar 1) shows an abrupt increase of the current around -72 mV

(vs. SCE) probably as a result of the initiation of pits, despite its lower corrosion rate than TC1. However, even in this case the hysteresis loop is very small, so that under the present exposure conditions the probability of pitting corrosion seems to be very low. A passive region in the curve between -534 mV and -72 mV (vs. SCE) is also observed, before the increase in the current occurs. The latter value corresponds to the pitting corrosion potential (E_{pit}). Pits are expected to form at potentials more positive than E_{pit}. The protection potential (E_{prot}), also known as the repassivation potential, appears around -222 mV (vs. SCE) where the reverse scan intersects the forward scan. At potentials more negative than E_{prot} pitting corrosion will not take place and the active pits will repassivate. Between E_{pit} and E_{prot} new pits will not form but the old ones will propagate. Notice from Figure 3.46 that the lower current level in the polarization curve agrees with the lower corrosion rate of C4 compared to TC1. It should be kept in mind that OPC-TC beams were cast during the winter, so that the presence of microcracks due to freezing/thawing cycles is possible.

The Electrochemical Noise measurements (Figures 3.47 and 3.48) of the corrosion probes at the crack in another OPC beam (C5) revealed the probable rupture and subsequently repassivation of the passive layer. This behaviour is characteristic of unstable pitting. The relatively slow repassivation may be associated with the slow diffusion of oxygen necessary to restore the passive film. These figures show a very good correlation between the ECN and EPN, confirming that those probes are undergoing corrosion.

4.3.- Comparison between statically and dynamically loaded beams

The corrosion potentials from the non-submerged and submerged probes did not show significant differences between the static and dynamic tests for all the concretes. Most of the values are in the same range. Only in the case of HPC-Slag were some values of E_{corr} more negative in the dynamic test under submerged conditions. However, those values correspond to only one probe (beam S6). It should be noted that, only one of the three probes under submerged conditions was connected to the DAQ system in order to measure the E_{corr}. In the

S6 beam the other two probes had much more positive E_{corr} values. Thus, the type of loading did not affect the corrosion behaviour of those probes that were far from the zone of bending.

In the case of the probes at the crack, it can be seen from the histograms in Appendixes B and C that, in all the concretes, the corrosion potentials reached more negative values when the beams are under cyclic loading.

According to the results recorded in Appendices B and C, the corrosion rates showed good qualitative agreement with the corrosion potentials. However, a more negative potential does not necessarily mean a higher corrosion rate; it will depend on other factors such as the pH and the availability of oxygen. Thus, the non-submerged and submerged probes under static loading presented corrosion rates similar to those under dynamic loading. In the case of the probes at the crack, the corrosion rates were generally much higher for dynamically loaded beams than for statically loaded beams, despite the latter having been exposed to the solution for almost twice as long as the former. However, in several cases, the corrosion rates of some probes at the crack are in the same range of those submerged in both statically and dynamically loaded beams. This suggests that these probes are relatively far from the crack. Only the OPC-C beams presented very few values that were higher in dynamic beams (without taking into consideration C10, which has a double crack).

The more positive corrosion potentials and lower corrosion rates of the probes at the crack in the statically loaded beams compared to the dynamically loaded beams could be due to two important factors. The first one has to do with the self-healing of the crack under static loading as the hydration reactions proceed. This would result in a partial sealing of the crack, and hence in a reduction of the ingress of corrosive species, such as chloride ions, water and oxygen. The additional opening of the crack (0.1 mm) during the dynamic loading avoid this self-healing. The second factor deals with the internal damage of the concrete, with the appearance of defects and cracks during the cyclic loading. The latter would still enhance the ingress of the species responsible for the corrosion of the carbon steel probes. The formation of the corrosion products may also block the crack of the statically loaded beams. However, in

the dynamically loaded beams the corrosion products may be removed during the cyclic loading.

The heterogeneous nature of concrete and the difficulties in inducing the cracks with the same characteristics are some of the factors that could cause variability in the results. This complicates the comparison of the corrosion measurements between beams of the same concrete and under the same exposure conditions or even between probes within the same beam in a particular condition. The failure and leaking of the pistons during the dynamic test is another issue that may have influenced the corrosion measurements.

5. Summary and Conclusions

Most of corrosion potentials from the non-submerged and submerged probes in all the concretes and for both static and dynamic, are more positive than -350 mV (vs. CSE), i.e. below the limit established by the ASTM standard C876-87 for a 90% probability of corrosion. The probes at the crack show more negative potentials so that the probability of corrosion is higher. In general, the OPC concretes presented more negative potentials than HPC. The general ranking from more negative to more positive potentials was as follows: OPC-TC<OPC-C<HPC-Slag<HPC-Fly Ash. The probes in the crack of the statically loaded beams exhibited more positive potentials than those in the dynamically loaded beams.

The corrosion rates under submerged and non-submerged conditions for both loading tests behaved in a similar way to the corrosion potentials. The low corrosion rates under these conditions indicate that the probes are still passive. In the case of the probes at the crack level higher corrosion rates were obtained, under both static and dynamic loading. The corrosion rates generally occurred same order as for the corrosion potentials, i.e.: OPC-TC>OPC-C>HPC-Slag>HPC-Fly Ash. The presence of cracks can increase significantly the corrosion rate of the steel, under both static and dynamic loading. Cyclic loading can enhance the corrosion rate even more. Despite the relatively low strength and high water/cement ratio of HPC beams, compared to standard mixes for HPC, they show a good performance from a corrosion point of view. The better corrosion behaviour of HPC than OPC concrete is agreement with work reported in the literature.

In general, while there was a good agreement between the corrosion potentials and the corrosion rates, a very negative corrosion potential did not always give rise to a high corrosion rate. This depended on different factors, such as the diffusion of oxygen to the metal surface. For this reason, the corrosion potential values recommended by the ASTM standard should not be taken as conclusive indication of corrosion and the corrosion rates must be evaluated. The corrosion rates of the probes at the crack were higher in dynamically loaded beams than in the statically loaded beams. The former, specifically the OPC concretes, reached values around

200 μm/year, whereas those in the statically loaded beams was ~50 μm/year, even though they have been exposed to the solution for half of the time of the statically loaded beams.

The lower corrosion rates of the probes at the crack in statically loaded beams may be attributed to a self-healing of the concrete as a result of the progressing of the hydration reactions or blocking by corrosion products. The possible formation of microcracks during cyclic loading may also cause higher corrosion of dynamic beams, by creating additional paths for the diffusion of corrosive species, such as chloride ions, water and oxygen.

The higher corrosion rates of the OPC beams than HPC beams, under both static and dynamic loading, as well as the higher resistance of HPC than OPC concrete, was confirmed by the EIS measurements.

The application of a cyclic or static load shifted the corrosion potential to more negative values. This shift seems to increase with the increase in the amount of load. A possible cause of this behaviour could be due to stress concentration on the reinforcement.

The heterogeneous nature of concrete, as well as the complications in reproducing similar experimental conditions can give rise to some variability between the results for supposedly “identical” exposure conditions.

6. Recommendations

For a better understanding of the corrosion mechanism of the reinforcing steel probes embedded in the beams, it is recommended that a larger number of specimens be evaluated by Electrochemical Impedance Spectroscopy (EIS) and Cyclic Polarization. Visual examination of the probes and the identification of the corrosion products formed by Raman Spectroscopy and/or X-rays diffraction would be of great help with this aim.

For future work, it would be interesting to compare the corrosion behaviour of cracked concrete with sound concrete both under dynamic loading. With respect to those who designed of the beams used in this work, there are some points that can be improved in a new design. The use of larger probes along the crack region and parallel to each other would allow the crack to intersect all the probes. In this way, more reproducibility in the results can be obtained and the probes will be more representative of the reinforcing steel. The stainless steel probes can be located further from the concrete surface, so that they are less affected by corrosion and the loading. Corrosion probes may be embedded in both sides of the sound concrete beams to study the effect of compression on one side and of bending on the other one. Since the corrosion rates of the non-submerged probes are still very low, it is not worth embedding probes at this level in new beams.

Other factors that should be considered are the increase of the concentration of chlorides and/or the period of wetting and drying, the measurement of the corrosion rate after the drying period, especially during the first months and the monitoring of the corrosion potential using the CML during loading or unloading for a longer period. It would also be interesting to study the effect of loading on reinforcing steel exposed to a solution simulating the concrete with or without chlorides. The use of EIS in this case will also help in the interpretation of the results obtained for the probes embedded in concrete, in the search of the most appropriate equivalent circuit and in the identification of the mechanisms controlling the corrosion process.

References

ACI-222 (2001). American Concrete Institute Manual of Concrete Practice.

ACI-224 (2001). American Concrete Institute Manual of Concrete Practice.

Ahmad, S. (2003). "Reinforcement corrosion in concrete structures, its monitoring and service life prediction—a review". *Cement and Concrete Composites* 25, 459–471.

Ahn, W., Reddy, D.V. (2001). "Galvanostatic testing for the durability of marine concrete under fatigue loading". *Cement and Concrete Research* 31, 343-349.

Aldea, C.M., Young, F., Wanga, K., Shah, S.P. (2000). "Effects of curing conditions on properties of concrete using slag replacement". *Cement and Concrete Research* 30, 465-472.

Alonso, C., Andrade, C., Castellote, M., Castro, P. (2000). "Chloride threshold values to depassivate reinforcing bars embedded in a standardized OPC mortar". *Cement and Concrete Research* 30 (7) 1047-1055.

Andrade, C; Gonzalez, J.A. (1978). Quantitative measurements of the corrosion rate of reinforcing steel embedded in concrete using polarization resistance measurements. *Werkstoffe und Korrosion* 29, 515-519.

ASTM (1991). C 876-91, Standard test method for half-cell potentials of uncoated reinforcing steel in concrete. American Society for Testing and Materials, Philadelphia, PA.

Babu, K.G., Prakash, P.V.S. (1995). "Efficiency of silica fume in concrete". *Cement and Concrete Research* 25, 1273-1283.

Bakker, R.F.M. (1983). *"Permeability of blended cement concretes"*. Proceedings of the CANMET/ACI First International Conference on the use of Fly Ash, Silica Fume, Slag and other mineral by-products in concrete, pp. 589-605.

Bentz, D.P. (2000). "Influence of silica fume on diffusivity in cement-based materials: II. Multi-scale modeling of concrete diffusivity". *Cement and Concrete Research* 30, 1121- 1129.

Castel, A., François, R., Arliguie, G. (1999). "Effect of loading on carbonation penetration in reinforced concrete elements". *Cement and Concrete Research* 29, 561–565.

Chiaia, B.; van Mier, J.G.M., Vervuurt, A. (1998). "Crack growth mechanisms in four different concretes: microscopic observations and fractal analysis". *Cement and Concrete Research* 28, 103-114.

Dehghanian, C. (1999). “Corrosion Behaviour of Steel in Concrete Made with Slag-Blended Cement”. *Corrosion* 55, 291-296.

Delagrave, A., Pigeon, M., Marchand, J., Revertégat, É. (1996). *Cement and Concrete Research* 26, 749-760.

Feliu, V.; Gonzalez, J.A.;Andrade, C.; Feliu, S. (1998). “Equivalent circuit for modelling the steel concrete interface. I. Experimental evidence and theoretical predictions”. *Corrosion Science* 39, pp. 864-882.

Glass, G.K., Reddy, B., Buenfeld, N.R. (2000). “The participation of bound chloride in passive film breakdown on steel in concrete”. *Corrosion Science* 42, 2013-2021

Gonzalez, J.A., Andrade, C.; Alonso, C.; Feliu, S. (1995). “Comparison of rates of general corrosion and maximum pitting penetration on concrete embedded steel reinforcement”. *Cement and Concrete Research* 25, 257-264.

Hansson, C.M. (1984). “Comments on electrochemical measurements of the rate of corrosion of steel in concrete”. *Cement and Concrete Research* 14, 547-584.

Hansson, C.M. (2003). Personal communication.

Hansson, C.M. (1995). *Metallurgical and Materials Transactions A* 26A, 1321-1341.

Jaul, W.-C., Tsay, D.-S. (1998). “A study of the basic engineering properties of slag cement concrete and its resistance to seawater corrosion”. *Cement and Concrete Research*, 28 (10) 1363–1371.

Jones, D.A. (1996). “Principles and prevention of corrosion”, second edition.

Khatri, R.P., Sirivivatnanon, V. (1995). “Effect of different supplementary cementitious materials on mechanical properties of high performance concrete”. *Cement and Concrete Research* 25, 209-220.

Kim, J.-K., Kim, Y.-Y. (1999). “Fatigue crack growth of high-strength concrete in wedge-splitting test”. *Cement and Concrete Research* 29, 705–712

Kosmatka, S.H. et al. (2000). *Design and control of concrete mixtures*, EB101, 7th Edition, Cement Association of Canada.

Kuzel, H.-J. (1996). “Initial hydration reactions and mechanisms of delayed ettringite formation in portland cements”. *Cement and Concrete Composites* 18, 195-203.

Lee, C., Lee, M.G. (1997). *Effect of fly ash and corrosion inhibitor on reinforced concrete in marine environments*, Proceedings Fourth CANMET/ACI International Conference Durability of concrete, Sydney, Australia.

Legat, A. and Govekar, E. (1994). "Detection of corrosion by analysis of electrochemical noise". *Fractals* 2 (2) 241-244.

Leng, F., Feng, N., Lu, X. (2000). "An experimental study on the properties of resistance to diffusion of chloride ions of fly ash and blast furnace slag concrete". *Cement and Concrete Research* 30, 989-992.

Li, X., Chung, D.D.L. (1998). "Improving Silica Fume for Concrete by Surface Treatment". *Cement and Concrete Research*, 28, 493-498.

Lilkov, V., Dimitrova, E., Petrov, O.E. (1997). "Hydration process of cement containing fly ash and silica fume: the first 24 hours". *Cement and Concrete Research* 27, 577-588.

Lowea, A.M., Erenb, H., Bailey, S.I. (2003). "Electrochemical noise analysis: detection of electrode asymmetry". *Corrosion Science* 45 (5) 941-955.

Luoa, R., Caib, Y., Wang, C., Huanga, X. (2003). "Study of chloride binding and diffusion in GGBS concrete". *Cement and Concrete Research* 33 (1) 1-7.

Martinez-Perez, B. (2000). "A study of the effect of chloride binding on service life predictions". *Cement and Concrete Research* 30, 1215-1223.

Malhotra, V.M., Ramezanianpour, A.A. (1994). *Fly ash in concrete*. Second edition. Natural Resources Canada.

Mehta, P.K. (1986). *Concrete, structure, properties and materials*, Prentice-Hall, Inc., New Jersey.

Mehta, P.K., Monteiro, P.J.M. (1993). *Concrete, structure, properties and materials*, Prentice-Hall, Inc., New Jersey.

Millard, S.G. et al. (2001). *NDT&E International* 34, 409-417.

Mindess, S., Young, V. (1981). *Concrete*, Prentice-Hall, Inc., New Jersey.

Mohammed, T.U., Hamada, H. (2003). "A discussion of the paper "Relationship between the free and total chloride diffusivity in concrete" by Xinying Lu, Cuiling Li, and Haixia Zhang". *Cement and Concrete Research* 33 (3) 451-452

Montemor, M.F., Simoes, A.M.P., Ferreira, M.G.S. (2003). “Chloride-induced corrosion on reinforcing steel: from the fundamentals to the monitoring techniques”. *Cement & Concrete Composites* 25 491–502.

MTO (1999). “High Performance Concrete at the Ontario Ministry of Transportation”, *ACI High Performance Concrete Seminar*, Toronto, ON.

Neville, A.M. (1990). *Properties of Concrete*, 3rd. Edition. John Wiley & Sons Inc., New York.

Ngala, V.T., Page, C L; Parrott, L J; Yu, S W. (1995). “Diffusion in cementitious materials: II. Further investigations of chloride and oxygen diffusion in well-cured OPC and pastes”. *Cement and Concrete Research* 25 (4) 819-826.

Osborne, G.J. (1999). “Durability of portland blast-furnace slag cement concrete”. *Cement and Concrete Composites* 21, 11-21.

Papadakis, V.G. (1999). “Experimental investigation and theoretical modeling of silica fume activity in concrete”. *Cement and Concrete Research* 29, 79–86.

Polder, R.B., Peelen, W.H.A. (2002). “Characterization of chloride transport and reinforcement corrosion in concrete under cyclic wetting and drying by electrical resistivity”. *Cement & Concrete Composites* 24, 427–435.

Pourbaix, M. (1974). Atlas of Electrochemical Equilibrium in Aqueous Solutions, Franklin, J.A., translator, National Association of Corrosion Engineers, Paris, France.

Saito, M., Ishimori, M. (1995). “Chloride permeability of concrete under static and repeated compressive loading”. *Cement and Concrete Research* 25 (4) 803-808.

Schießl, P., Wiens, U. (1997). Long term influence of fly ash on chloride-induced corrosion, *Proceedings* Fourth CANMET/ACI International Conference Durability of concrete, Sydney, Australia.

Sioulas, B., Sanjayan, J.G. (2000). “Hydration temperatures in large high-strength concrete columns incorporating slag”. *Cement and Concrete Research* 30, 1791-1799.

Sirivivatnanon, V., Kidav, E.U. (1997). Fly ash concretes in south-east Asia and Australia, *Proceedings* Fourth CANMET/ACI International Conference Durability of concrete, Sydney, Australia.

Stansbury, E.E., Buchanan, R.A.(2000). *Fundamentals of Electrochemical Corrosion*, ASM International.

Stern, M., Geary, A.L. (1957). “Electrochemical Polarization: I. A theoretical analysis of the shape of polarization curves”. *Journal of the Electrochemical Society* 104, pp. 56-63.

Swamy, R.N. (1997). Design for Durability and strength through the use of fly ash and slag in concrete. *Proceedings* Third CANMET/ACI International Symposium Advances in Concrete Technology.

Tasdemir, C., Tasdemir, Mehmet A.; Lydon, Frank D.; Barr, Ben I.G. (1996). “Effects of silica fume and aggregate size on the brittleness of concrete”. *Cement and Concrete Research* 26 (1) 63-68.

Taylor, F.W.H. (1990). Cement Chemistry, Ed. Academic Press Limited.

Thomas, M.D., Shehata, M.H.; Shashiprakash, S.G.; Hopkins, D.S.; Cail, K. (1999). “Use of ternary cementitious systems containing silica fume and fly ash in concrete”. *Cement and Concrete Research* 29, 1207–1214.

Thompson, N.G., Payer, J.H. “DC Electrochemical Test Methods”, National Association of Corrosion Engineers (NACE), Vol. 6, 1998.

Turkmen, I., Gavgal, M., Gu, R. (2003). *Materials Letters* 57, 2037– 2043.

Vivekanandam, K. (1997). “Transition zone in high performance concrete during hydration”. *Cement and Concrete Research* 27, 817-823.

Appendix A: Diagrams and Connections

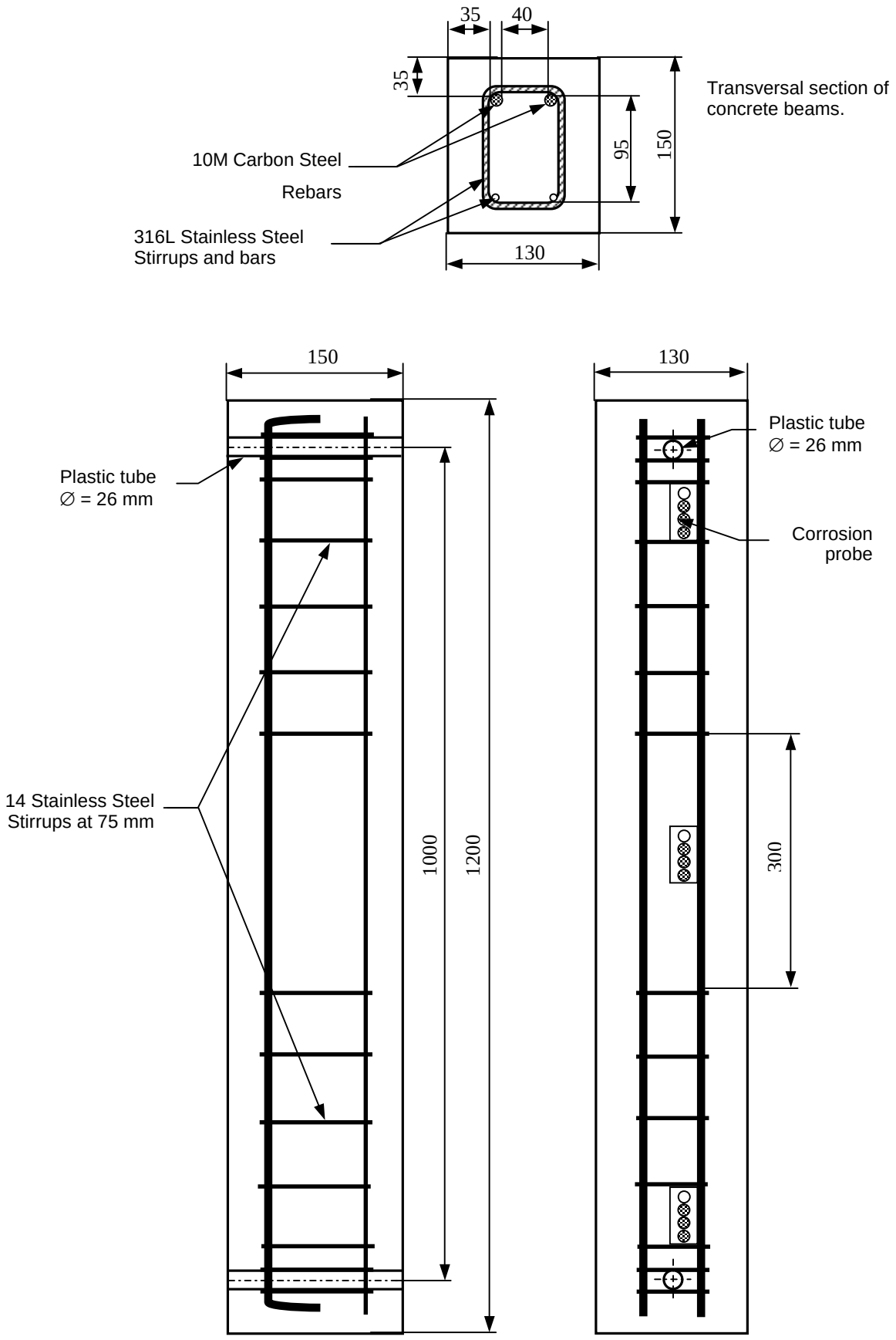

Figure A.1.- Diagram of the different sections of the beam.

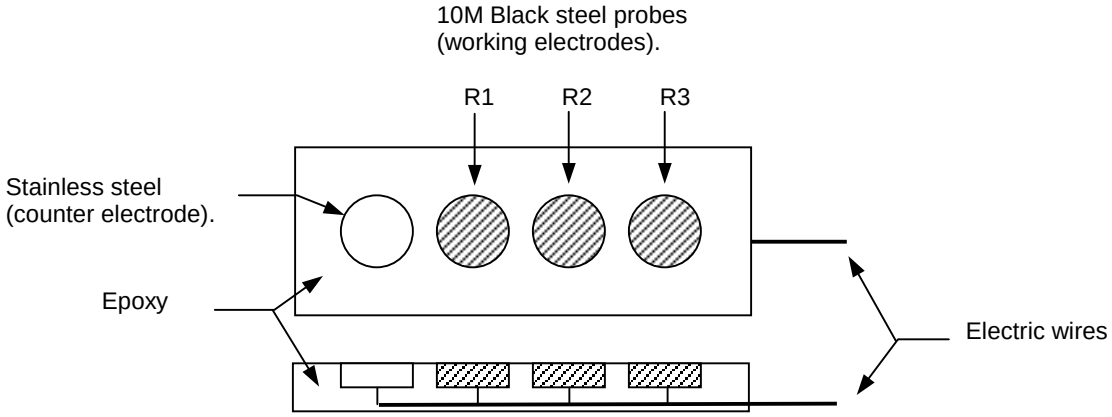

Figure A.2.- Corrosion probe set.

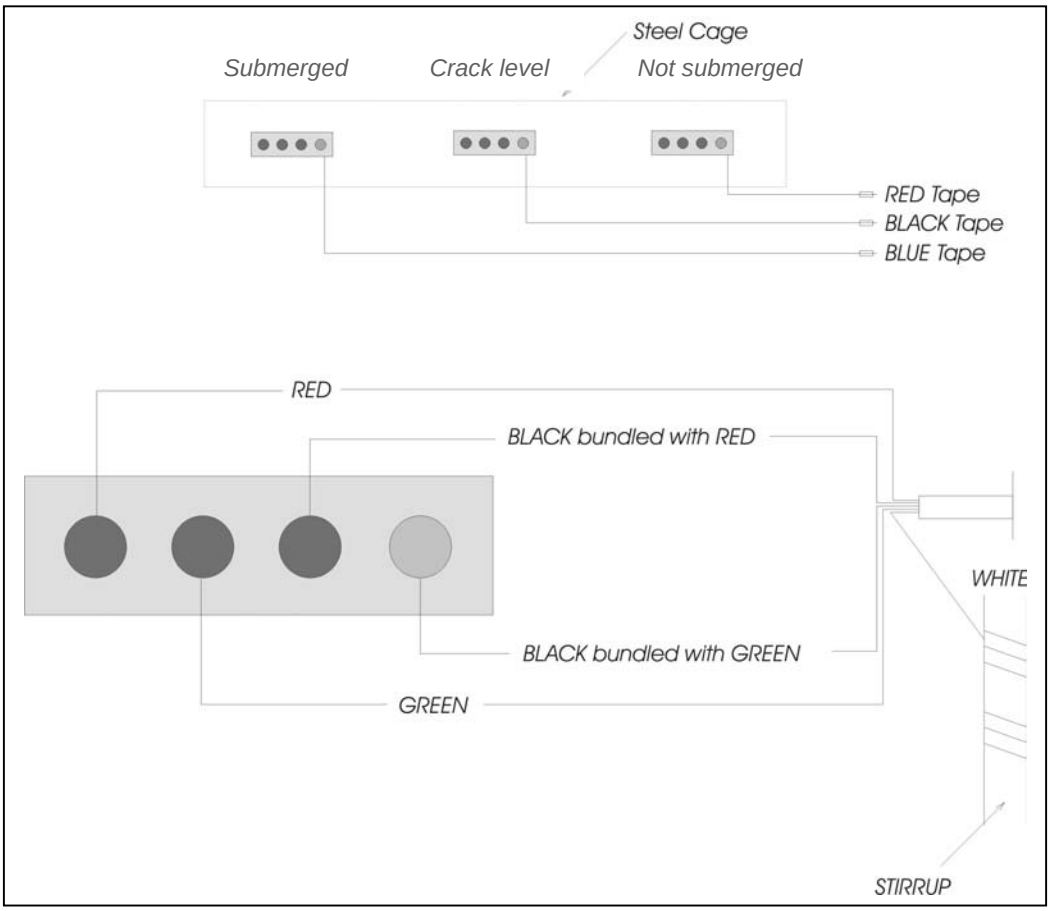

Figure A.3.- Wire connections to each corrosion probe.

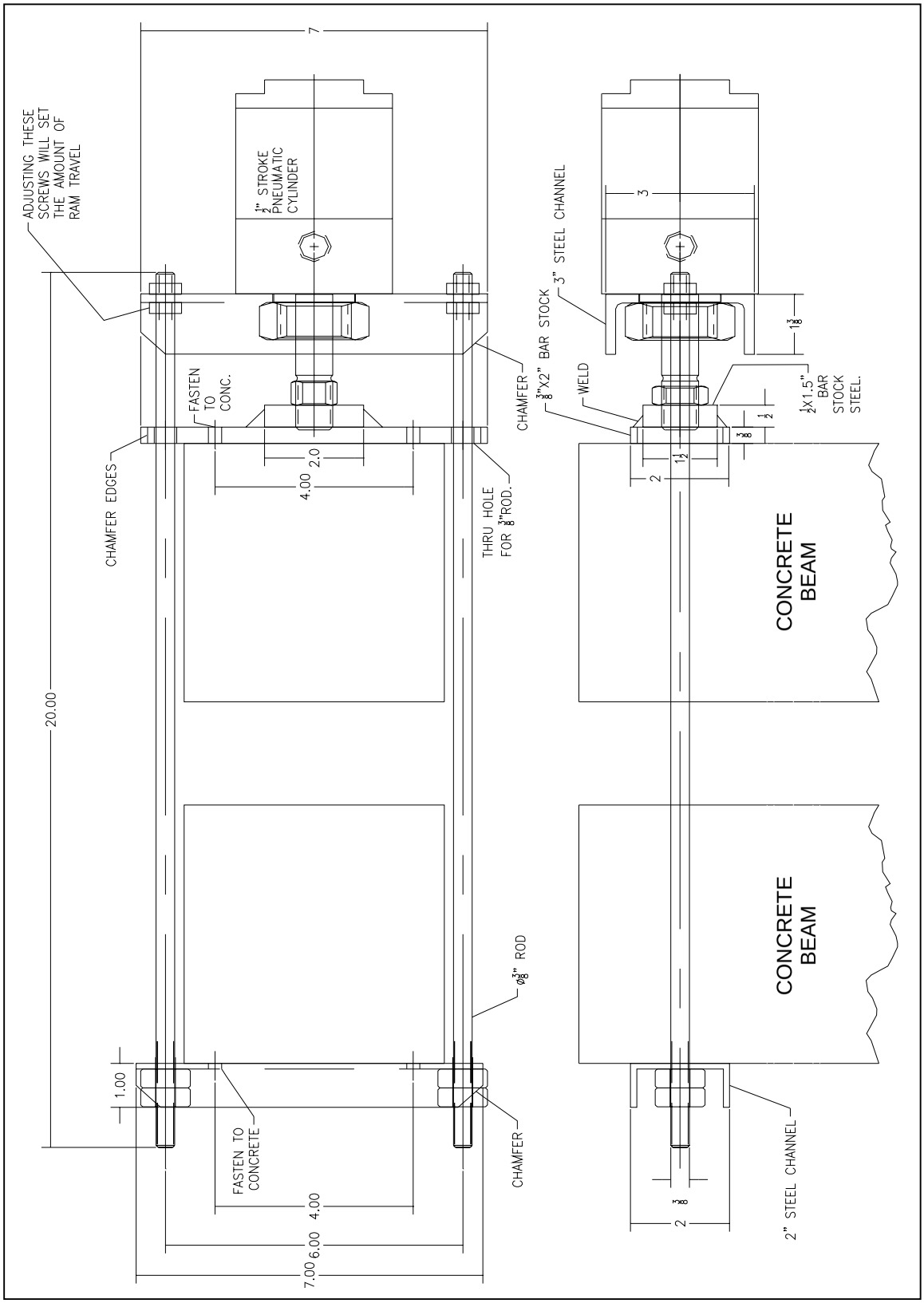

Figure A.4.- Design of new set-up for dynamic beams. Design and drawing by Jim Baleshta.

Table A.1.- Dynamically loaded beams. Junction Box/Data Logger Wire Color Connections (SLOT 1).

Beam Name (Channels)	Wires connected to the Top probe (Pair number)	Wires connected to the Crack level probes (Pair number)	Wires connected to the Bottom probe (Pair number)
TC9 (1-5)	SS=Black in Black/Orange (1) BS=Orange in Black/Orange (1)	SS=Black in Black/Red (2) BS=Red in Black/Red (2) SS=Black in Black/Green (3) BS=Green in Black/Green (3) SS=Black in Black/White (4) BS=White in Black/White (4)	SS=White in White/Red (5) BS=Red in White/Red (5)
TC7 (6-10)	SS=Blue in Blue/Red (6) BS=Red in Blue/Red (6)	SS=Green in Green/Red (7) BS= Red in Green/Red (7) SS=Yellow in Yellow/Red (8) BS=Red in Yellow/Red (8) SS=Black in Black/Blue (9) BS=Blue in Black/Blue (9)	SS=Black in Black/Yellow (10) BS=Yellow in Black/Yellow (10)
F9 (11-15)	SS=Black in Black/Orange (11) BS=Orange in Black/Orange (11)	SS=Black in Black/Brown (12) BS=Brown in Black/Brown (12) SS=Black in Black/Green (13) BS=Green in Black/Green (13) SS=Black in Black/White (14) BS=White in Black/White (14)	SS=White in White/Red (15) BS=Red in White/Red (15)
F8 (16-20)	SS=Blue in Blue/Red (16) BS=Red in Blue/Red (16)	SS=Green in Green/Red (17) BS= Red in Green/Red (17) SS=Yellow in Yellow/Red (18) BS=Red in Yellow/Red (18) SS=Black in Black/Blue (19) BS=Blue in Black/Blue (19)	SS=Black in Black/Yellow (20) BS=Yellow in Black/Yellow (20)
S9 (21-25)	SS=Black in Black/Brown (21) BS=Brown in Black/Brown (21)	SS=Black in Black/Red (22) BS=Red in Black/Red (22) SS=Black in Black/Green (23) BS=Green in Black/Green (23) SS=Black in Black/White (24) BS=White in Black/White (24)	SS=White in White/Red (25) BS=Red in White/Red (25)
S8 (26-30)	SS=Blue in Blue/Red (26) BS=Red in Blue/Red (26)	SS=Green in Green/Red (27) BS= Red in Green/Red (27) SS=Yellow in Yellow/Red (28) BS=Red in Yellow/Red (28) SS=Black in Black/Blue (29) BS=Blue in Black/Blue (29)	SS=Black in Black/Yellow (30) BS=Yellow in Black/Yellow (30)
C6 (31-35)	SS=Black in Black/Orange (31) BS=Orange in Black/Orange (31)	SS=Black in Black/Red (32) BS=Red in Black/Red (32) SS=Black in Black/Green (33) BS=Green in Black/Green (33) SS=Black in Black/White (34) BS=White in Black/White (34)	SS=White in White/Red (35) BS=Red in White/Red (35)
C2 (36-40)	SS=Blue in Blue/Red (36) BS=Red in Blue/Red (36)	SS=Green in Green/Red (37) BS= Red in Green/Red (37) SS=Yellow in Yellow/Red (38) BS=Red in Yellow/Red (38) SS=Black in Black/Blue (39) BS=Blue in Black/Blue (39)	SS=Black in Black/Yellow (40) BS=Yellow in Black/Yellow (40)

Note: SS=Stainless Steel, BS=Black Steel **On Slots, High (H)=SS, Low (L)=BS**

Table A.2.- Dynamically loaded beams. Junction Box/Data Logger Wire Color Connections (SLOT 2).

Beam Name (Channels)	Wires connected to the Top probe (Pair number)	Wires connected to the Crack level probes (Pair number)	Wires connected to the Bottom probe (Pair number)
S2 (1-5)	SS=Black in Black/Orange (1) BS=Orange in Black/Orange (1)	SS=Black in Black/Red (2) BS=Red in Black/Red (2) SS=Black in Black/Green (3) BS=Green in Black/Green (3) SS=Black in Black/White (4) BS=White in Black/White (4)	SS=White in White/Red (5) BS=Red in White/Red (5)
S3 (6-10)	SS=Blue in Blue/Red (6) BS=Red in Blue/Red (6)	SS=Green in Green/Red (7) BS= Red in Green/Red (7) SS=Yellow in Yellow/Red (8) BS=Red in Yellow/Red (8) SS=Black in Black/Blue (9) BS=Blue in Black/Blue (9)	SS=Black in Black/Yellow (10) BS=Yellow in Black/Yellow (10)
F7 (11-15)	SS=Black in Black/Orange (11) BS=Orange in Black/Orange (11)	SS=Black in Black/Brown (12) BS=Brown in Black/Brown (12) SS=Black in Black/Green (13) BS=Green in Black/Green (13) SS=Black in Black/White (14) BS=White in Black/White (14)	SS=White in White/Red (15) BS=Red in White/Red (15)
F5 (16-20)	SS=Blue in Blue/Red (16) BS=Red in Blue/Red (16)	SS=Green in Green/Red (17) BS= Red in Green/Red (17) SS=Yellow in Yellow/Red (18) BS=Red in Yellow/Red (18) SS=Black in Black/Blue (19) BS=Blue in Black/Blue (19)	SS=Black in Black/Yellow (20) BS=Yellow in Black/Yellow (20)
C5 (21-25)	SS=Black in Black/Orange (21) BS=Orange in Black/Orange (21)	SS=Black in Black/Red (22) BS=Red in Black/Red (22) SS=Black in Black/Green (23) BS=Green in Black/Green (23) SS=Black in Black/White (24) BS=White in Black/White (24)	SS=White in White/Red (25) BS=Red in White/Red (25)
C4 (26-30)	SS=Blue in Blue/Red (26) BS=Red in Blue/Red (26)	SS=Green in Green/Red (27) BS= Red in Green/Red (27) SS=Yellow in Yellow/Red (28) BS=Red in Yellow/Red (28) SS=Black in Black/Blue (29) BS=Blue in Black/Blue (29)	SS=Black in Black/Yellow (30) BS=Yellow in Black/Yellow (30)
TC1 (31-35)	SS=Black in Black/Orange (31) BS=Orange in Black/Orange (31)	SS=Black in Black/Red (32) BS=Red in Black/Red (32) SS=Black in Black/Green (33) BS=Green in Black/Green (33) SS=Black in Black/White (34) BS=White in Black/White (34)	SS=White in White/Red (35) BS=Red in White/Red (35)
TC10 (36-40)	SS=Blue in Blue/Red (36) BS=Red in Blue/Red (36)	SS=Green in Green/Red (37) BS= Red in Green/Red (37) SS=Yellow in Yellow/Red (38) BS=Red in Yellow/Red (38) SS=Black in Black/Blue (39) BS=Blue in Black/Blue (39)	SS=Black in Black/Yellow (40) BS=Yellow in Black/Yellow (40)

Table A.3.- Statically loaded beams. Junction Box/Data Logger Wire Color Connections (SLOT 3).

Beam Name (Channels)	Wires connected to the Top probe (Pair number)	Wires connected to the Crack level probes (Pair number)	Wires connected to the Bottom probe (Pair number)
S10 (1-5)	SS=Black in Black/Orange (1) BS=Orange in Black/Orange (1)	SS=Black in Black/Red (2) BS=Red in Black/Red (2) SS=Black in Black/Green (3) BS=Green in Black/Green (3) SS=Black in Black/White (4) BS=White in Black/White (4)	SS=White in White/Red (5) BS=Red in White/Red (5)
S5 (6-10)	SS=Blue in Blue/Red (6) BS=Red in Blue/Red (6)	SS=Green in Green/Red (7) BS= Red in Green/Red (7) SS=Yellow in Yellow/Red (8) BS=Red in Yellow/Red (8) SS=Black in Black/Blue (9) BS=Blue in Black/Blue (9)	SS=Black in Black/Yellow (10) BS=Yellow in Black/Yellow (10)
TC6 (11-15)	SS=Black in Black/Orange (11) BS=Orange in Black/Orange (11)	SS=Black in Black/Red (12) BS=Red in Black/Red (12) SS=Black in Black/Green (13) BS=Green in Black/Green (13) SS=Black in Black/White (14) BS=White in Black/White (14)	SS=White in White/Red (15) BS=Red in White/Red (15)
TC4 (16-20)	SS=Blue in Blue/Red (16) BS=Red in Blue/Red (16)	SS=Green in Green/Red (17) BS= Red in Green/Red (17) SS=Yellow in Yellow/Red (18) BS=Red in Yellow/Red (18) SS=Black in Black/Blue (19) BS=Blue in Black/Blue (19)	SS=Black in Black/Yellow (20) BS=Yellow in Black/Yellow (20)
S7 (21-25)	SS=Black in Black/Orange (21) BS=Orange in Black/Orange (21)	SS=Black in Black/Red (22) BS=Red in Black/Red (22) SS=Black in Black/Green (23) BS=Green in Black/Green (23) SS=Black in Black/White (24) BS=White in Black/White (24)	SS=White in White/Red (25) BS=Red in White/Red (25)
S1 (26-30)	SS=Blue in Blue/Red (26) BS=Red in Blue/Red (26)	SS=Green in Green/Red (27) BS= Red in Green/Red (27) SS=Yellow in Yellow/Red (28) BS=Red in Yellow/Red (28) SS=Black in Black/Blue (29) BS=Blue in Black/Blue (29)	SS=Black in Black/Yellow (30) BS=Yellow in Black/Yellow (30)
TC3 (31-35)	SS=Black in Black/Orange (31) BS=Orange in Black/Orange (31)	SS=Black in Black/Red (32) BS=Red in Black/Red (32) SS=Black in Black/Green (33) BS=Green in Black/Green (33) SS=Black in Black/White (34) BS=White in Black/White (34)	SS=White in White/Red (35) BS=Red in White/Red (35)
TC5 (36-40)	SS=Blue in Blue/Red (36) BS=Red in Blue/Red (36)	SS=Green in Green/Red (37) BS= Red in Green/Red (37) SS=Yellow in Yellow/Red (38) BS=Red in Yellow/Red (38) SS=Black in Black/Blue (39) BS=Blue in Black/Blue (39)	SS=Black in Black/Yellow (40) BS=Yellow in Black/Yellow (40)

Note: SS=Stainless Steel, BS=Black Steel On Slots, High (H)=SS, Low (L)=BS

Table A.4.- Statically loaded beams. Junction Box/Data Logger Wire Color Connections (SLOT 4).

Beam Name (Channels)	Wires connected to the Top probe (number)	Wires connected to the Crack level probes (number)	Wires connected to the Bottom probe (number)
C9 (1-5)	SS=Black in Black/Orange (1) BS=Orange in Black/Orange (1)	SS=Black in Black/Red (2) BS=Red in Black/Red (2) SS=Black in Black/Green (3) BS=Green in Black/Green (3) SS=Black in Black/White (4) BS=White in Black/White (4)	SS=White in White/Red (5) BS=Red in White/Red (5)
C8 (6-10)	SS=Blue in Blue/Red (6) BS=Red in Blue/Red (6)	SS=Green in Green/Red (7) BS= Red in Green/Red (7) SS=Yellow in Yellow/Red (8) BS=Red in Yellow/Red (8) SS=Black in Black/Blue (9) BS=Blue in Black/Blue (9)	SS=Black in Black/Yellow (10) BS=Yellow in Black/Yellow (10)
F3 (11-15)	SS=Black in Black/Orange (11) BS=Orange in Black/Orange (11)	SS=Black in Black/Red (12) BS=Red in Black/Red (12) SS=Black in Black/Green (13) BS=Green in Black/Green (13) SS=Black in Black/White (14) BS=White in Black/White (14)	SS=White in White/Red (15) BS=Red in White/Red (15)
F4 (16-20)	SS=Blue in Blue/Red (16) BS=Red in Blue/Red (16)	SS=Green in Green/Red (17) BS= Red in Green/Red (17) SS=Yellow in Yellow/Red (18) BS=Red in Yellow/Red (18) SS=Black in Black/Blue (19) BS=Blue in Black/Blue (19)	SS=Black in Black/Yellow (20) BS=Yellow in Black/Yellow (20)
C10 (21-25)	SS=Black in Black/Orange (21) BS=Orange in Black/Orange (21)	SS=Black in Black/Red (22) BS=Red in Black/Red (22) SS=Black in Black/Green (23) BS=Green in Black/Green (23) SS=Black in Black/White (24) BS=White in Black/White (24)	SS=White in White/Red (25) BS=Red in White/Red (25)
C3 (26-30)	SS=Blue in Blue/Red (26) BS=Red in Blue/Red (26)	SS=Green in Green/Red (27) BS= Red in Green/Red (27) SS=Yellow in Yellow/Red (28) BS=Red in Yellow/Red (28) SS=Black in Black/Blue (29) BS=Blue in Black/Blue (29)	SS=Black in Black/Yellow (30) BS=Yellow in Black/Yellow (30)
F6 (31-35)	SS=Black in Black/Orange (31) BS=Orange in Black/Orange (31)	SS=Black in Black/Red (32) BS=Red in Black/Red (32) SS=Black in Black/Green (33) BS=Green in Black/Green (33) SS=Black in Black/White (34) BS=White in Black/White (34)	SS=White in White/Red (35) BS=Red in White/Red (35)
F1 (36-40)	SS=Blue in Blue/Red (36) BS=Red in Blue/Red (36)	SS=Green in Green/Red (37) BS= Red in Green/Red (37) SS=Yellow in Yellow/Red (38) BS=Red in Yellow/Red (38) SS=Black in Black/Blue (39) BS=Blue in Black/Blue (39)	SS=Black in Black/Yellow (40) BS=Yellow in Black/Yellow (40)

Note: SS=Stainless Steel, BS=Black Steel On Slots, High (H)=SS, Low (L)=BS

Appendix B: Statically Loaded Beams. Corrosion rates.

Table B.1.- Corrosion potentials (vs. ERE) of black steel probes in beams F4, S10, TC4 and C8 during the wetting stage.

	Days wetting				
Beam (Probe)	1	2	6	10	14
Crack level					
F4 (R1)	-173	-175	-172	-174	-171
F4 (R2)	-364	-382	-360	-114	-370
F4 (R3)	-209	-210	-207	-207	-208
Submerged					
F4 (R1)	-190	-195	-192	-194	-194
F4 (R2)	-343	-353	-350	-350	-315
F4 (R3)	-204	-206	-205	-206	-206
Crack level					
S10 (R1)	-210	-209	-213	-221	-236
S10 (R2)	-154	-154	-158	-158	-158
S10 (R3)	-200	-200	-377	-406	-408
Submerged					
S10 (R1)	-265	-261	-266	-283	-313
S10 (R2)	-228	-227	-228	-225	-223
S10 (R3)	-240	-240	-240	-270	-303
Crack level					
TC4 (R1)	-361	-380	-621	-666	-692
TC4 (R2)	-177	-176	-179	-185	-188
TC4 (R3)	-280	-284	-350	-448	-513
Submerged					
TC4 (R1)	-135	-128	-130	-126	-126
TC4 (R2)	-1117	-1116	-1117	-1117	-1117
TC4 (R3)	-165	-166	-170	-178	-182
Crack level					
C8 (R1)	-454	-461	-485	-489	-495
C8 (R2)	-260	-260	-263	-264	-261
C8 (R3)	-395	-400	-475	-546	-644
Submerged					
C8 (R1)	-221	-222	-225	-227	-229
C8 (R2)	-216	-216	-219	-219	-220
C8 (R3)	-239	-238	-239	-240	-243

Table B. 2.- Corrosion potentials (vs. ERE) of black steel probes in beams F4, S10, TC4 and C8 during the drying stage.

	Days drying				
Beam (Probe)	1	2	6	10	14
Crack level					
F4 (R1)	-156	-152	-149	-145	-145
F4 (R2)	-370	-370	-360	-355	-360
F4 (R3)	-224	-220	-214	-211	-209
Submerged					
F4 (R1)	-216	-215	-220	-218	-220
F4 (R2)	-392	-390	-400	-390	-400
F4 (R3)	-240	-241	-246	-246	-248
Crack level					
S10 (R1)	-192	-218	-200	-185	-191
S10 (R2)	-138	-135	-133	-134	-125
S10 (R3)	-250	-241	-232	-227	-223
Submerged					
S10 (R1)	-175	-201	-222	-229	-250
S10 (R2)	-127	-139	-158	-184	-206
S10 (R3)	-213	-225	-235	-230	-245
Crack level					
TC4 (R1)	-674	-683	-684	-347	-324
TC4 (R2)	-160	-162	-163	-160	-155
TC4 (R3)	-532	-549	-556	-367	-267
Submerged					
TC4 (R1)	-120	-124	-120	-140	-145
TC4 (R2)	-1100	-1096	-1096	-1133	-1140
TC4 (R3)	-171	-170	-178	-186	-186
Crack level					
C8 (R1)	-547	-515	-470	-463	-459
C8 (R2)	-253	-257	-253	-253	-253
C8 (R3)	-668	-678	-505	-461	-450
Submerged					
C8 (R1)	-158	-161	-154	-154	-153
C8 (R2)	-137	-145	-139	-140	-141
C8 (R3)	-157	-166	-158	-159	-160

Table B.3.- Corrosion rates (μm/year) of non-submerged probes in HPC-Fly Ash beams.

Beam	Probe	Exposure time in solution (weeks)													
		2	6	8	10	12	14	18	20	29	35	37	41	43	45
F4	R1	0.00	0.09	0.11	0.12	0.07	0.11	0.07	0.07	0.09	0.22	0.16	0.12	0.13	0.21
	R2	0.06	0.09	0.004	0.10	0.16	0.03	0.11	0.27	0.06	0.18	0.04	0.20	0.12	0.02
	R3	0.49	0.07	0.18	0.15	0.19	0.04	0.12	0.11	0.21	0.17	0.07	0.18	0.08	0.15
F3	R1	0.22	0.26	0.18	0.19	0.18	0.24	0.15	0.14	0.08	0.20	0.16	0.15	0.16	0.20
	R2	0.26	0.25	0.17	0.29	0.25	0.16	0.16	0.06	0.22	0.37	0.36	0.10	0.13	0.07
	R3	0.21	0.24	0.15	0.31	0.28	0.26	0.15	0.19	0.27	0.31	0.12	0.27	0.18	0.14
F1	R1	0.35	0.41	0.37	0.42	0.41	0.38	0.31	0.34	0.26	0.36	0.32	0.30	0.31	0.37
	R2	0.05	0.08	0.10	0.20	0.25	0.11	0.08	0.18	0.08	0.08	0.06	0.08	0.04	0.08
	R3	0.24	0.11	0.09	0.15	1E-4	0.26	0.16	0.23	0.14	0.09	0.15	0.10	0.09	0.09
F6	R1	0.20	0.17	0.15	0.18	0.15	0.20	0.15	0.12	0.17	0.24	0.17	0.14	0.15	0.13
	R2	0.15	0.09	0.14	0.14	0.19	0.16	0.15	0.17	0.19	0.14	0.10	0.16	0.12	0.16
	R3	0.16	0.20	0.20	0.21	0.21	0.22	0.18	0.20	0.10	0.11	0.17	0.18	0.14	0.20
Minimum		0.001	0.07	0.004	0.10	1E-4	0.03	0.07	0.06	0.06	0.08	0.04	0.08	0.04	0.02
Maximum		0.49	0.41	0.37	0.42	0.41	0.38	0.31	0.34	0.27	0.37	0.36	0.30	0.31	0.37
Average		0.20	0.17	0.15	0.21	0.19	0.18	0.15	0.17	0.16	0.21	0.16	0.16	0.14	0.15
Standard Deviation		0.13	0.11	0.09	0.09	0.10	0.10	0.06	0.08	0.08	0.10	0.10	0.07	0.07	0.09

Table B.4.- Corrosion rates (μm/year) of probes at the crack in HPC-Fly Ash beams.

Beam	Probe	Exposure time in solution (weeks)																		
		2	6	8	10	12	14	18	20	22	24	26	29	31	33	35	37	41	43	45
F4	R1	14.54	1.42	1.09	1.26	1.00	1.13	1.01	1.01	1.00	0.88	0.83	0.88	0.75	0.87	0.85	0.93	0.88	0.95	1.12
	R2	3.68	0.13	0.15	0.57	0.43	0.35	0.72	0.61	0.14	0.35	0.32	0.25	0.12	0.38	0.34	0.18	0.65	0.26	0.78
	R3	14.49	2.22	1.82	2.08	1.56	1.81	1.54	1.58	1.37	1.29	1.13	1.26	1.22	1.16	1.32	1.40	1.36	1.36	1.60
F3	R1	2.18	1.00	0.98	1.26	0.75	0.98	1.31	0.86	1.08	0.43	0.65	0.61	0.78	0.62	0.74	0.73	0.73	0.87	1.03
	R2	1.47	0.75	0.50	0.70	0.69	0.63	0.55	0.45	0.50	0.42	0.18	0.35	0.54	0.88	0.38	0.50	0.52	0.74	0.41
	R3	8.83	1.28	0.97	1.46	0.96	1.36	1.07	1.13	1.16	0.73	0.67	0.70	0.69	0.66	0.75	0.65	0.77	0.66	0.73
F1	R1	1.84	3.84	3.17	3.73	2.26	2.11	1.55	1.75	1.07	0.83	0.78	0.90	0.71	0.71	0.91	0.56	0.65	0.90	1.48
	R2	5.08	2.66	1.95	1.34	1.36	1.73	1.08	0.94	0.80	0.73	0.56	0.57	0.54	0.47	0.67	0.63	0.76	1.14	1.20
	R3	3.49	2.93	2.14	1.96	1.58	1.28	1.19	1.16	0.86	0.42	0.36	0.41	0.65	0.40	0.50	0.50	0.67	0.78	1.08
F6	R1	0.92	0.59	0.39	0.42	0.41	0.31	0.26	0.35	0.33	0.28	0.25	0.22	0.23	0.35	0.25	0.36	0.29	0.23	0.28
	R2	1.09	0.47	0.38	0.36	0.37	0.24	0.28	0.24	0.16	0.23	0.35	0.24	0.24	0.25	0.20	0.20	0.20	0.19	0.26
	R3	2.06	1.11	0.52	0.47	0.63	0.39	0.35	0.51	0.45	0.47	0.25	0.40	0.51	0.49	0.47	0.35	0.38	0.25	0.51
Minimum		0.92	0.13	0.15	0.36	0.37	0.24	0.26	0.24	0.14	0.23	0.18	0.22	0.12	0.25	0.20	0.18	0.20	0.19	0.26
Maximum		14.54	3.84	3.17	3.73	2.26	2.11	1.55	1.75	1.37	1.29	1.13	1.26	1.22	1.16	1.32	1.40	1.36	1.36	1.60
Average		4.97	1.53	1.17	1.30	1.00	1.03	0.91	0.88	0.74	0.59	0.53	0.56	0.58	0.60	0.62	0.58	0.66	0.69	0.87
Standard Deviation		4.96	1.13	0.91	0.96	0.58	0.65	0.47	0.48	0.42	0.31	0.29	0.32	0.30	0.27	0.32	0.34	0.30	0.39	0.45

Table B.5.- Corrosion rates (μm/year) of submerged probes in HPC-Fly Ash beams.

Beam	Probe	Exposure time in solution (weeks)																		
		2	6	8	10	12	14	18	20	22	24	26	29	31	33	35	37	41	43	45
F4	R1	0.09	0.41	0.28	0.34	0.47	0.69	0.57	0.66	0.45	0.59	0.71	0.70	0.41	0.74	0.58	0.53	0.78	0.60	0.73
	R2	0.08	0.33	0.16	0.29	0.35	0.23	0.48	0.45	0.30	0.29	0.43	0.43	0.22	0.37	0.19	0.20	0.42	0.24	0.53
	R3	0.27	1.77	1.42	1.48	1.38	1.55	1.37	1.28	1.20	1.91	1.42	1.40	1.35	1.20	1.31	1.17	1.15	1.30	1.30
F3	R1	0.22	3.21	1.93	1.32	1.36	1.58	0.88	1.21	1.02	0.91	0.86	0.84	0.80	0.90	1.19	0.93	0.90	0.76	0.85
	R2	0.12	3.46	2.12	0.86	0.66	0.51	0.52	0.45	0.50	0.36	0.38	0.41	0.40	0.45	0.50	0.34	0.43	0.50	0.38
	R3	0.28	0.38	0.14	0.11	0.22	0.72	0.58	0.50	0.63	0.30	0.20	0.11	0.45	0.46	0.59	0.59	0.48	0.79	0.77
F1	R1	0.43	1.99	1.24	1.19	0.64	0.88	0.66	0.58	0.58	0.47	0.45	0.42	0.43	0.49	0.67	0.64	0.61	0.62	0.84
	R2	0.20	0.70	0.53	0.54	0.60	0.36	0.67	0.50	0.61	0.51	0.63	0.54	0.37	0.59	0.71	0.35	0.26	0.30	0.34
	R3	1.09	3.82	2.76	1.46	0.79	0.85	0.91	0.57	0.55	0.53	0.46	0.59	0.35	0.51	0.76	0.72	0.50	0.65	1.02
F6	R1	0.31	0.45	0.42	0.46	0.42	0.45	0.42	0.39	0.36	0.36	0.25	0.33	0.35	0.31	0.54	0.51	0.53	0.41	0.55
	R2	0.18	0.38	0.32	0.25	0.22	0.25	0.27	0.26	0.28	0.22	0.22	0.17	0.21	0.19	0.34	0.23	0.35	0.29	0.23
	R3	0.38	0.43	0.42	0.46	0.48	0.41	0.36	0.41	0.28	0.33	0.35	0.28	0.26	0.27	0.43	0.40	0.42	0.39	0.33
Minimum		0.08	0.33	0.14	0.11	0.22	0.23	0.27	0.26	0.28	0.22	0.20	0.11	0.21	0.19	0.19	0.20	0.26	0.24	0.23
Maximum		1.09	3.82	2.76	1.48	1.38	1.58	1.37	1.28	1.20	1.91	1.42	1.40	1.35	1.20	1.31	1.17	1.15	1.30	1.30
Average		0.30	1.44	0.98	0.73	0.63	0.71	0.64	0.60	0.56	0.57	0.53	0.52	0.47	0.54	0.65	0.55	0.57	0.57	0.66
Standard Deviation		0.27	1.36	0.89	0.51	0.38	0.45	0.30	0.32	0.29	0.46	0.35	0.35	0.32	0.29	0.32	0.29	0.25	0.30	0.32

Table B.6.- Corrosion rates (μm/year) of non-submerged probes in HPC-Slag beams.

Beam	Probe	Exposure time in solution (weeks)														
		2	6	8	10	12	14	18	20	22	29	35	37	41	43	45
S5	R1	0.40	0.51	0.17	0.50	0.14	0.23	0.32	0.14	0.09	0.18	0.28	0.19	0.10	0.08	0.02
	R2	0.16	0.34	0.06	0.09	0.10	0.08	0.03	0.08	0.10	0.13	0.21	0.06	0.10	0.07	0.04
	R3	0.11	0.02	0.02	0.05	0.07	0.10	0.08	0.21	0.11	0.06	0.08	0.004	0.02	0.06	0.08
S10	R1	0.05	0.26	0.16	0.02	0.17	0.06	0.16	0.09	0.27	0.15	0.16	0.18	0.13	0.03	0.03
	R2	0.06	0.18	0.06	0.10	0.12	0.03	0.08	0.28	0.21	0.21	0.21	0.05	0.06	0.04	0.03
	R3	0.22	0.17	0.07	0.15	0.16	0.16	0.17	0.14	0.08	0.23	0.05	0.14	0.14	0.02	0.05
S1	R1	0.41	0.01	0.08	0.14	0.25	0.08	0.13	0.28	0.13	0.06	0.02	0.08	0.05	0.11	0.06
	R2	0.004	0.002	0.02	0.15	0.08	0.03	0.10	0.07	0.14	0.06	0.42	0.15	0.09	0.07	0.07
	R3	0.16	0.10	0.10	0.09	0.02	0.20	0.11	0.07	0.05	0.21	0.10	0.20	0.09	0.05	0.05
S7	R1	0.02	0.05	0.19	0.10	0.05	0.06	0.08	0.13	0.15	0.03	0.09	0.01	0.12	0.10	0.03
	R2	0.16	0.17	0.16	0.11	0.04	0.09	0.01	0.07	0.10	0.10	0.19	0.03	0.08	0.01	0.04
	R3	0.05	0.15	0.11	0.10	0.10	0.05	0.06	0.11	0.10	0.22	0.18	0.03	0.09	0.06	0.03
Minimum		0.004	0.002	0.02	0.02	0.02	0.03	0.01	0.07	0.05	0.03	0.02	0.004	0.02	0.01	0.02
Maximum		0.41	0.51	0.19	0.50	0.25	0.23	0.32	0.28	0.27	0.23	0.42	0.20	0.14	0.11	0.08
Average		0.15	0.16	0.10	0.13	0.11	0.10	0.11	0.14	0.13	0.14	0.17	0.09	0.09	0.06	0.04
Standard Deviation		0.14	0.15	0.06	0.12	0.07	0.07	0.08	0.08	0.06	0.07	0.11	0.07	0.03	0.03	0.02

Table B.7.- Corrosion rates (μm/year) of probes at the crack in HPC-Slag beams.

Beam	Probe	Exposure time in solution (weeks)																		
		2	6	8	10	12	14	18	20	22	24	26	29	31	35	37	41	43	45	47
S5	R1	34.5	23.8	4.06	3.36	2.47	4.44	1.21	0.32	1.30	1.02	0.81	0.51	0.34	0.49	0.55	0.57	0.58	0.49	0.53
	R2	17.8	1.09	0.85	0.79	0.79	0.97	0.75	1.20	0.39	0.40	0.94	0.35	0.23	0.27	0.62	0.33	0.32	0.36	0.29
	R3	25.8	8.61	11.0	11.6	9.27	0.38	0.03	1.01	0.83	1.21	1.02	0.70	0.76	1.02	1.32	0.75	0.91	0.79	0.85
S10	R1	7.13	9.09	8.05	10.4	7.87	9.93	0.68	0.48	1.54	0.02	0.36	0.33	0.30	0.65	0.45	0.77	1.06	0.31	1.06
	R2	1.83	2.65	1.66	1.72	0.98	1.09	3.69	2.47	0.68	0.08	0.58	0.31	0.12	0.63	0.39	0.50	0.50	0.33	0.55
	R3	3.41	3.98	4.76	5.19	4.03	2.13	1.18	1.03	0.56	0.19	0.32	0.25	0.20	0.55	0.65	0.75	0.57	0.96	0.94
S1	R1	12.8	18.5	3.24	2.30	1.36	2.03	0.81	1.07	3.15	0.81	0.82	2.95	3.91	3.71	3.39	8.66	5.02	5.34	4.24
	R2	0.95	1.09	0.55	0.49	0.30	0.10	0.62	0.27	0.21	0.19	0.15	0.10	0.52	0.36	0.36	0.61	0.47	0.42	0.37
	R3	9.46	8.61	3.28	1.63	0.12	0.60	1.39	0.94	0.74	0.64	0.79	4.75	3.42	2.36	1.28	1.97	2.02	2.33	1.51
S7	R1	2.00	3.31	1.07	1.12	2.35	4.07	1.96	1.72	0.78	0.60	0.66	0.57	0.61	0.53	0.41	0.45	0.58	0.44	0.55
	R2	1.12	2.82	0.90	1.05	1.18	3.43	2.62	1.42	0.85	0.68	0.61	0.90	0.40	0.45	0.49	0.46	0.48	0.46	0.47
	R3	10.5	8.68	2.75	11.6	11.2	3.18	7.37	2.76	2.61	2.44	1.65	0.91	0.59	0.94	1.40	0.89	0.66	0.84	0.54
Minimum		0.95	1.09	0.55	0.49	0.12	0.10	0.03	0.27	0.21	0.02	0.15	0.10	0.12	0.27	0.36	0.33	0.32	0.31	0.29
Maximum		34.5	23.7	11.0	11.6	11.2	9.93	7.37	2.76	3.15	2.44	1.65	4.75	3.91	3.71	3.39	8.66	5.02	5.34	4.24
Average		10.6	7.68	3.52	4.27	3.49	2.70	1.86	1.22	1.14	0.69	0.73	1.05	0.95	1.00	0.94	1.39	1.10	1.09	0.99
Standard Deviation		10.7	7.07	3.19	4.38	3.81	2.71	2.00	0.78	0.90	0.66	0.39	1.38	1.29	1.02	0.86	2.33	1.32	1.45	1.08

Table B.8.- Corrosion rates (μm/year) of submerged probes in HPC-Slag beams.

Beam	Probe	Exposure time in solution (weeks)																		
		2	6	8	10	12	14	18	20	22	24	26	29	31	35	37	41	43	45	47
S5	R1	1.14	0.81	0.99	0.53	0.57	1.14	2.08	1.25	2.09	1.24	1.72	0.72	0.98	1.04	1.03	0.92	0.23	1.12	0.28
	R2	0.24	0.51	0.18	0.14	0.50	0.29	0.29	1.01	0.61	0.43	0.83	0.36	0.71	0.80	0.07	0.27	0.13	0.20	0.13
	R3	0.64	1.09	0.78	1.38	0.96	0.89	2.21	2.52	1.93	1.94	2.41	1.10	0.67	1.28	0.78	0.98	0.11	1.04	0.21
S10	R1	0.37	0.54	0.46	0.58	0.62	1.11	1.56	1.06	0.99	0.88	0.76	0.37	0.65	1.08	0.15	0.35	0.48	0.39	0.45
	R2	1.40	1.02	0.48	0.46	0.57	0.36	0.47	0.59	0.67	0.46	0.13	0.54	0.14	0.49	0.64	0.55	0.47	0.42	0.41
	R3	0.15	0.54	0.22	0.41	0.45	0.53	0.96	0.75	1.02	0.32	0.54	0.27	0.48	0.12	0.49	0.33	0.42	0.39	0.40
S1	R1	0.16	0.27	0.07	0.15	2.46	2.31	2.46	2.52	1.71	0.85	0.82	1.05	1.40	0.21	0.42	0.18	0.26	0.16	0.26
	R2	0.13	0.48	0.05	0.20	0.10	0.14	0.34	0.31	0.28	0.15	0.42	0.13	0.33	0.61	0.46	0.46	0.52	0.44	0.38
	R3	0.23	0.49	0.19	0.16	2.23	2.86	2.57	3.46	2.30	1.47	2.38	2.88	2.90	0.66	0.62	1.12	1.25	0.90	0.73
S7	R1	1.80	2.41	0.77	0.56	0.84	1.21	1.75	1.66	1.21	1.01	0.95	0.33	0.35	0.32	0.52	0.44	0.61	0.55	0.44
	R2	0.10	0.19	0.02	0.16	0.15	0.40	0.28	0.12	0.11	0.14	0.35	0.14	0.10	0.24	0.11	0.12	0.16	0.09	0.04
	R3	0.09	0.11	0.09	0.09	0.14	0.60	0.36	0.39	0.23	0.16	0.30	0.30	0.29	0.22	0.03	0.17	0.15	0.10	0.17
Minimum		0.09	0.11	0.02	0.09	0.10	0.14	0.28	0.12	0.11	0.14	0.13	0.13	0.10	0.12	0.03	0.12	0.11	0.09	0.04
Maximum		1.80	2.41	0.99	1.38	2.46	2.86	2.57	3.46	2.30	1.94	2.41	2.88	2.90	1.28	1.03	1.12	1.25	0.96	0.73
Average		0.54	0.70	0.36	0.40	0.80	0.99	1.28	1.30	1.10	0.75	0.97	0.68	0.75	0.59	0.44	0.49	0.40	0.45	0.33
Standard Deviation		0.59	0.61	0.33	0.36	0.77	0.83	0.92	1.04	0.76	0.58	0.78	0.76	0.77	0.39	0.31	0.34	0.32	0.36	0.18

Table B.9.- Corrosion rates (μm/year) of non-submerged probes in OPC-C beams.

Beam	Probe	Exposure time in solution (weeks)													
		2	6	8	10	12	14	18	20	29	35	37	41	43	45
C3	R1	0.58	0.08	0.35	0.17	0.17	0.39	0.33	0.12	0.09	0.20	0.12	0.06	0.13	0.12
	R2	0.43	0.34	0.12	0.13	0.15	0.14	0.05	0.11	0.15	0.11	0.13	0.12	0.11	0.11
	R3	0.26	0.74	0.31	0.39	0.15	0.38	0.11	0.13	0.17	0.13	0.17	0.16	0.11	0.16
C10	R1	0.38	0.18	0.16	0.06	0.22	0.09	0.02	0.08	0.43	0.12	0.07	0.08	0.09	0.37
	R2	0.17	0.30	0.11	0.23	0.16	0.13	0.10	0.09	0.10	0.09	0.02	0.11	0.05	0.10
	R3	0.20	0.14	0.10	0.04	0.53	0.05	0.04	0.03	0.27	0.06	0.18	0.24	0.01	0.05
C8	R1	0.41	0.50	0.45	0.43	0.32	0.33	0.14	0.15	0.21	0.17	0.43	0.25	0.28	0.21
	R2	0.14	0.15	0.28	0.11	0.06	0.09	0.02	0.22	0.08	0.31	0.28	0.08	0.11	0.12
	R3	0.21	0.04	0.32	0.17	0.18	0.22	0.19	0.13	0.09	0.20	0.45	0.04	0.04	0.11
C9	R1	0.21	0.21	0.29	0.15	0.10	0.10	0.24	0.23	0.02	0.23	0.36	0.13	0.11	0.07
	R2	0.25	0.22	0.02	0.27	0.09	0.09	0.20	0.24	0.20	0.17	0.30	0.11	0.33	0.11
	R3	0.14	0.08	0.17	0.21	0.09	0.18	0.14	0.14	0.09	0.34	0.17	0.11	0.02	0.10
Minimum		0.14	0.04	0.02	0.04	0.06	0.05	0.02	0.03	0.02	0.06	0.02	0.04	0.01	0.05
Maximum		0.58	0.74	0.45	0.43	0.53	0.39	0.33	0.24	0.43	0.34	0.45	0.25	0.33	0.37
Average		0.28	0.25	0.22	0.20	0.18	0.18	0.13	0.14	0.16	0.18	0.22	0.12	0.12	0.13
Standard Deviation		0.14	0.20	0.13	0.12	0.13	0.12	0.09	0.06	0.11	0.08	0.14	0.07	0.10	0.08

Table B.10.- Corrosion rates (μm/year) of probes at the crack in OPC-C beams.

Beam	Probe	Exposure time in solution (weeks)																			
		2	6	8	10	12	14	18	20	22	24	26	29	31	33	35	37	41	43	45	47
C3	R1	1.67	12.9	10.8	1.26	2.77	4.42	4.43	3.49	4.32	3.92	2.79	3.54	2.05	2.34	1.54	1.33	1.32	0.92	0.75	0.59
	R2	1.68	4.83	6.64	3.01	5.62	5.98	6.82	5.64	2.40	1.61	2.26	2.78	1.98	2.09	0.71	0.64	1.50	0.32	0.77	0.50
	R3	2.28	2.16	2.46	1.97	2.00	3.29	3.36	3.44	2.51	2.49	2.13	2.50	1.93	2.29	1.26	1.03	1.68	1.02	0.95	0.77
C10	R1	7.33	9.64	11.0	23.9	15.3	11.9	13.4	9.47	8.80	10.1	7.22	8.81	12.1	8.80	9.31	9.32	10.6	10.9	12.5	13.4
	R2	38.8	26.9	25.0	22.6	47.4	42.2	13.1	26.1	26.7	28.6	9.87	11.0	8.64	28.6	27.9	42.2	34.0	17.3	14.6	18.3
	R3	15.7	11.7	8.12	1.02	3.29	7.00	14.1	11.6	18.7	8.72	10.6	14.6	12.2	14.0	29.2	34.9	39.5	31.8	35.7	36.9
C8	R1	4.18	12.2	3.35	3.00	2.65	3.80	3.17	1.73	3.75	4.39	2.80	1.32	0.99	-	1.59	1.50	2.61	2.09	4.01	4.88
	R2	0.50	2.34	0.47	0.48	0.65	1.32	1.10	0.49	0.61	0.72	0.25	0.29	0.34	-	0.35	0.20	0.82	0.57	0.89	2.13
	R3	3.98	6.83	4.63	3.50	3.76	5.98	5.31	5.03	4.64	4.59	3.70	2.39	1.57	-	3.22	1.99	4.11	4.39	6.02	3.72
C9	R1	5.16	2.18	2.03	1.71	1.55	1.73	1.77	1.24	1.28	1.60	0.37	0.36	1.32	-	0.60	0.52	0.53	0.74	0.70	0.74
	R2	0.36	0.33	9.50	0.50	0.30	0.07	0.36	0.26	0.20	0.26	0.08	0.46	1.05	-	0.55	0.30	0.24	0.24	0.30	0.33
	R3	3.75	4.77	3.56	3.90	9.43	7.70	2.37	1.98	1.60	1.40	0.24	0.89	1.48	-	0.77	0.69	0.48	0.70	1.01	0.87
Minimum		0.36	0.33	0.47	0.48	0.30	0.07	0.36	0.26	0.20	0.26	0.08	0.29	0.34	2.09	0.35	0.20	0.24	0.24	0.30	0.33
Maximum		38.8	26.9	25.0	23.9	47.4	42.2	14.0	26.1	26.7	28.6	10.6	14.5	12.2	28.6	29.2	42.2	39.5	31.8	35.7	36.9
Average		7.11	8.06	7.30	5.57	7.89	7.96	5.77	5.87	6.29	5.69	3.53	4.07	3.81	9.69	6.41	7.89	8.12	5.92	6.52	6.92
Standard Deviation		10.8	7.35	6.61	8.34	13.2	11.3	4.99	7.27	8.18	7.83	3.72	4.73	4.44	10.4	10.6	14.6	13.7	9.72	10.4	11.1

Table B.11.- Corrosion rates (μm/year) of submerged probes in OPC-C beams.

Beam	Probe	Exposure time in solution (weeks)																			
		2	6	8	10	12	14	18	20	22	24	26	29	31	33	35	37	41	43	45	47
C3	R1	0.64	0.72	0.77	0.74	0.63	0.80	0.63	0.63	0.67	0.55	0.49	0.63	0.63	0.49	0.62	0.64	0.62	0.53	0.55	0.48
	R2	0.10	0.29	0.39	0.31	0.33	0.37	0.24	0.40	0.32	0.24	0.25	0.32	0.31	0.27	0.27	0.31	0.38	0.30	0.29	0.38
	R3	0.66	0.74	0.79	0.70	0.64	0.79	0.59	0.65	0.69	0.59	0.55	0.70	0.56	0.54	0.50	0.61	0.59	0.53	0.63	0.55
C10	R1	0.70	8.60	7.44	10.7	6.72	8.43	11.0	10.3	9.47	7.26	5.71	4.42	1.28	1.18	1.42	1.76	2.63	1.38	1.83	1.34
	R2	0.54	5.31	5.63	7.51	6.42	7.15	5.08	10.5	1.75	1.40	1.39	1.27	0.93	0.81	0.76	0.85	0.85	0.64	0.65	0.57
	R3	3.98	7.08	12.9	8.87	7.25	5.81	4.84	11.5	10.5	8.43	7.16	6.39	3.77	1.55	1.61	1.96	3.04	1.37	1.84	1.44
C8	R1	2.82	2.52	1.00	1.01	1.06	1.30	1.72	1.66	1.11	0.89	0.95	0.58	0.94	-	0.55	0.88	0.63	0.92	0.80	0.80
	R2	0.47	0.66	0.78	0.60	0.54	0.54	0.34	0.33	0.35	0.32	0.95	0.21	0.66	-	0.27	0.07	0.28	0.29	0.22	0.38
	R3	1.92	1.61	1.39	0.48	0.73	1.06	1.36	1.12	0.82	0.70	0.71	0.32	0.24	-	0.36	0.53	0.45	0.73	0.60	0.57
C9	R1	3.65	4.93	2.77	1.20	1.06	1.44	3.25	2.48	0.70	0.52	0.61	1.52	1.68	-	1.31	1.08	1.07	1.24	0.85	1.05
	R2	0.36	5.98	0.92	2.92	2.57	3.02	2.98	2.41	1.00	0.36	1.61	2.18	2.03	-	1.22	0.54	1.04	1.49	1.15	1.37
	R3	3.95	7.08	1.03	1.83	0.32	1.04	1.98	2.42	0.89	0.49	1.55	1.29	1.28	-	1.21	1.34	0.97	1.43	0.96	1.05
Minimum		0.10	0.29	0.39	0.31	0.32	0.37	0.24	0.33	0.32	0.24	0.25	0.21	0.24	0.27	0.27	0.07	0.28	0.29	0.22	0.38
Maximum		3.98	8.60	12.9	10.68	7.25	8.43	11.0	11.5	10.5	8.43	7.16	6.39	3.77	1.55	1.61	1.96	3.04	1.49	1.84	1.44
Average		1.65	3.79	2.99	3.07	2.35	2.65	2.83	3.70	2.36	1.81	1.83	1.65	1.19	0.81	0.84	0.88	1.05	0.90	0.86	0.83
Standard Deviation		1.53	3.02	3.83	3.72	2.75	2.84	3.06	4.35	3.59	2.85	2.22	1.89	0.97	0.51	0.48	0.57	0.88	0.46	0.52	0.40

Table B.12.- Corrosion rates (μm/year) of non-submerged probes in OPC-TC beams.

Beam	Probe	Exposure time in solution (weeks)														
		2	6	8	10	12	14	18	20	22	29	35	37	41	43	45
TC5	R1	0.09	0.58	0.22	0.07	0.17	0.19	0.01	0.05	0.05	0.09	0.09	0.09	0.20	0.06	0.03
	R2	0.23	0.24	0.01	0.07	0.08	0.08	0.13	0.11	0.13	0.14	0.26	0.26	0.06	0.15	0.09
	R3	0.14	0.15	0.18	0.13	0.16	0.08	0.08	0.13	0.13	0.04	0.12	0.12	0.08	0.10	0.04
TC3	R1	0.10	0.30	0.21	0.15	0.12	0.09	0.01	0.13	0.03	0.53	0.31	0.14	0.38	0.02	0.07
	R2	0.18	0.07	0.28	0.05	0.06	0.07	0.12	0.08	0.07	0.27	0.07	0.07	0.07	0.07	0.05
	R3	0.08	0.08	0.03	0.07	0.06	0.05	0.04	0.09	0.27	0.10	0.23	0.23	0.09	0.05	0.07
TC4	R1	0.10	0.08	0.005	0.08	0.44	0.26	0.01	0.11	0.08	0.07	0.23	0.23	0.09	0.08	0.05
	R2	0.23	0.33	0.14	0.11	0.21	0.10	0.18	0.51	0.12	0.16	0.20	0.20	0.05	0.10	0.08
	R3	0.10	0.45	0.26	0.64	0.55	0.03	0.09	0.10	0.09	0.08	0.19	0.19	0.11	0.08	0.07
TC6	R1	0.04	0.07	0.13	0.12	0.02	0.15	0.27	0.10	0.10	0.05	0.12	0.12	0.09	0.05	0.03
	R2	0.12	0.07	0.06	0.10	0.13	0.16	0.11	0.15	0.10	0.27	0.02	0.02	0.11	0.05	0.05
	R3	0.11	0.08	0.27	0.12	0.09	0.13	0.14	0.17	0.36	0.08	0.35	0.35	0.17	0.11	0.07
Minimum		0.04	0.07	0.005	0.05	0.02	0.03	0.01	0.05	0.03	0.04	0.02	0.02	0.05	0.02	0.03
Maximum		0.23	0.58	0.28	0.64	0.55	0.26	0.27	0.51	0.36	0.53	0.35	0.35	0.38	0.15	0.09
Average		0.13	0.21	0.15	0.14	0.18	0.11	0.10	0.14	0.13	0.16	0.18	0.17	0.13	0.08	0.06
Standard Deviation		0.06	0.17	0.10	0.16	0.16	0.06	0.08	0.12	0.09	0.14	0.10	0.09	0.09	0.03	0.02

Table B.13.- Corrosion rates (μm/year) of probes at the crack in OPC-TC beams.

Beam	Probe	Exposure time in solution (weeks)																		
		2	6	8	10	12	14	18	20	22	24	26	29	31	35	37	41	43	45	47
TC5	R1	0.67	1.91	1.41	1.18	1.82	1.79	1.72	1.31	1.95	2.03	2.40	4.93	4.67	2.22	2.23	1.75	2.81	2.22	1.97
	R2	0.94	3.77	0.85	0.83	9.67	14.2	9.97	5.53	5.50	9.88	6.98	3.22	0.90	0.71	1.42	1.38	3.84	1.23	1.08
	R3	0.92	1.03	1.71	2.77	3.05	4.34	3.22	2.56	2.14	2.32	2.46	2.37	1.44	4.37	2.01	4.45	3.51	3.56	1.40
TC3	R1	4.89	2.05	0.12	1.33	1.81	11.5	11.8	0.13	0.27	4.11	0.22	17.3	19.9	13.8	9.55	42.3	26.6	21.7	19.4
	R2	0.45	0.41	0.25	0.32	0.49	2.16	3.86	0.08	4.64	4.12	0.12	3.20	16.2	9.51	4.09	6.52	5.90	5.66	9.15
	R3	1.54	0.14	0.001	2.06	1.83	1.96	7.31	0.14	4.53	3.88	0.32	6.82	3.44	6.93	3.80	14.4	10.7	3.93	4.53
TC4	R1	13.0	2.87	1.82	1.71	6.83	6.99	7.69	9.42	12.2	6.70	5.35	40.7	23.8	40.0	20.4	16.3	10.4	12.1	15.7
	R2	1.69	0.44	0.20	0.58	3.92	5.20	0.97	3.04	4.04	3.22	5.15	19.0	5.47	3.35	3.00	3.40	1.92	2.94	4.15
	R3	16.9	3.97	2.24	2.70	9.90	10.8	6.31	5.12	8.76	3.28	2.21	5.56	6.36	5.85	2.58	8.88	4.41	3.25	2.34
TC6	R1	2.71	3.72	1.17	1.78	3.38	1.71	2.08	2.29	2.06	1.84	3.30	11.9	30.7	8.27	18.7	28.0	30.3	2.58	2.68
	R2	9.65	7.72	4.35	6.32	5.60	6.05	7.65	3.78	3.90	1.91	2.59	3.34	3.82	2.72	6.75	4.01	4.13	3.31	3.60
	R3	6.93	20.8	6.53	11.1	11.1	13.3	3.68	5.13	3.78	5.10	3.67	9.66	7.92	14.9	14.8	4.68	26.2	50.4	52.5
Minimum		0.45	0.14	0.001	0.32	0.49	1.71	0.97	0.08	0.27	1.84	0.12	2.37	0.90	0.71	1.42	1.38	1.92	1.23	1.08
Maximum		16.9	20.8	6.53	11.1	11.1	14.2	11.7	9.42	12.2	9.88	6.98	40.7	30.7	40.0	20.4	42.3	30.2	50.4	52.5
Average		5.03	4.07	1.72	2.73	4.95	6.67	5.52	3.21	4.48	4.03	2.90	10.7	10.4	9.38	7.45	11.3	10.9	9.41	9.87
Standard Deviation		5.49	5.69	1.94	3.08	3.63	4.68	3.44	2.78	3.24	2.33	2.16	11.0	9.81	10.6	6.84	12.4	10.5	14.1	14.6

Table B.14.- Corrosion rates (μm/year) of submerged probes in OPC-TC beams.

Beam	Probe	Exposure time in solution (weeks)																		
		2	6	8	10	12	14	18	20	22	24	26	29	31	35	37	41	43	45	47
TC5	R1	2.99	4.73	0.42	0.89	0.51	0.78	1.24	0.63	0.86	0.69	0.52	0.29	0.24	1.14	0.63	0.53	0.62	0.73	0.71
	R2	17.74	3.64	0.64	0.49	0.58	0.51	0.53	0.58	0.41	0.43	0.48	0.05	0.36	0.73	0.26	0.27	0.44	0.24	0.27
	R3	1.64	3.86	0.38	0.80	0.74	0.65	0.83	0.77	0.70	0.45	1.21	0.42	0.32	0.61	0.36	0.49	0.62	0.43	0.47
TC3	R1	0.15	0.38	0.21	0.41	0.50	0.63	0.75	0.73	0.60	0.33	0.26	2.02	0.30	0.69	0.27	0.49	0.53	0.45	0.46
	R2	0.21	0.50	0.20	0.13	0.47	0.41	0.30	0.25	0.29	0.19	0.83	0.27	0.47	0.47	0.08	0.23	0.38	0.43	0.21
	R3	0.15	0.23	0.31	0.07	0.18	0.37	0.47	0.37	0.10	0.25	0.30	0.17	0.10	0.58	0.27	0.17	0.22	0.27	0.19
TC4	R1	3.21	1.10	1.64	0.78	1.00	0.74	0.61	0.37	0.14	0.67	0.47	1.18	0.31	1.49	0.02	0.14	0.17	0.29	0.16
	R2	27.28	38.85	7.59	7.34	2.63	3.48	7.92	5.77	6.20	5.27	4.62	4.23	3.80	2.66	2.40	2.10	2.49	1.28	2.13
	R3	2.63	0.16	2.25	0.46	4.63	3.52	3.25	3.59	0.15	0.60	1.40	0.77	0.11	0.42	0.27	0.43	0.54	0.01	0.07
TC6	R1	0.63	0.89	0.46	0.50	0.75	0.68	2.28	0.84	0.74	0.55	0.34	0.19	0.23	0.31	0.14	0.33	0.28	0.51	0.15
	R2	0.24	0.25	0.09	0.32	0.29	0.45	0.82	0.43	0.29	0.40	0.22	0.37	0.28	0.47	0.43	0.24	0.31	0.29	0.22
	R3	1.06	1.36	0.70	1.12	0.56	1.51	1.88	1.70	0.83	0.96	0.63	0.58	0.48	0.41	1.28	0.48	0.84	0.64	0.59
Minimum		0.15	0.16	0.09	0.07	0.18	0.37	0.30	0.25	0.10	0.19	0.22	0.05	0.10	0.31	0.02	0.14	0.17	0.01	0.07
Maximum		27.28	38.85	7.59	7.34	4.63	3.52	7.92	5.77	6.20	5.27	4.62	4.23	3.80	2.66	2.40	2.10	2.49	1.28	2.13
Average		4.83	4.66	1.24	1.11	1.07	1.14	1.74	1.34	0.94	0.90	0.94	0.88	0.58	0.83	0.53	0.49	0.62	0.46	0.47
Standard Deviation		8.58	10.89	2.10	1.99	1.29	1.14	2.14	1.67	1.68	1.39	1.22	1.19	1.02	0.67	0.67	0.52	0.62	0.32	0.56

Table B.15.- Corrosion rates after two weeks drying and after the beams being submerged for 45 weeks.

	Probe					
	R1	R2	R3	R1	R2	R3
Beam	*Crack level*			*Submerged*		
F3	0.65	0.42	0.63	0.7	0.32	0.57
F4	0.99	0.39	1.34	0.44	0.43	1.04
F1	1.28	0.68	0.64	0.46	0.53	0.66
F6	0.25	0.16	0.32	0.41	0.21	0.34
S7	0.56	0.46	0.74	0.39	0.017	0.33
S1	3.95	0.35	1.76	0.28	0.34	0.79
S10	1.06	0.44	0.56	0.43	0.36	0.35
S5	0.39	0.29	0.71	-	-	-
C8	2.48	0.58	1.81	0.74	0.41	0.50
C9	0.56	0.23	0.68	0.84	0.99	0.75
TC6	9.43	3.54	38.34	0.27	0.23	0.38
TC4	8.17	1.7	1.85	0.11	0.41	0.32
TC3	16.99	5.85	5.22	0.49	0.22	0.18
TC5	1.67	1.83	0.65	0.61	0.33	0.38

Appendix C: Dynamically Loaded Beams. Corrosion rates

Table C.1.- Corrosion rates (μm/year) of non-submerged probes in HPC-Fly Ash beams.

Beam	Probe	Exposure time in solution (weeks)						
		0.5	4.5	8.5	14	16	20	22
F9	R1	0.06	0.07	0.03	0.10	0.12	0.21	0.12
	R2	0.23	0.03	0.07	0.11	0.09	0.10	0.17
	R3	0.28	0.11	0.17	0.25	0.06	0.10	0.18
F8	R1	0.51	0.12	0.07	0.23	0.15	0.07	0.06
	R2	0.25	0.10	0.07	0.13	0.07	0.11	0.09
	R3	0.39	0.14	0.13	0.01	0.12	0.08	0.15
F7	R1	0.33	-	0.43	0.48	0.10	0.39	0.08
	R2	0.24	-	0.08	0.05	0.13	0.13	0.28
	R3	0.11	-	0.46	0.12	0.10	0.07	0.16
F5	R1	0.25	-	0.10	0.15	0.15	0.18	0.12
	R2	0.20	-	0.14	0.12	0.11	0.11	0.13
	R3	0.06	-	0.13	0.13	0.11	0.16	0.18
Minimum		0.06	0.03	0.03	0.01	0.06	0.07	0.06
Maximum		0.51	0.14	0.46	0.48	0.15	0.39	0.28
Average		0.24	0.10	0.16	0.16	0.11	0.14	0.14
Standard Deviation		0.13	0.04	0.14	0.12	0.03	0.09	0.06

Table C.2.- Corrosion rates (μm/year) of probes at the crack in HPC-Fly Ash beams.

Beam	Probe	Exposure time in solution (weeks)											
		0.5	4.5	8.5	12	14	16	20	22	23	24	25	26
F9	R1	5.76	10.36	3.71	0.23	0.10	1.27	2.46	2.60	1.51	1.79	1.49	-
	R2	0.40	4.27	0.32	0.38	0.42	0.41	0.35	0.33	0.46	0.64	0.49	-
	R3	9.93	8.55	0.54	0.85	0.74	0.72	0.73	0.69	0.72	0.86	0.63	-
F8	R1	3.18	12.92	1.64	1.73	1.57	2.30	1.58	3.53	1.86	2.61	1.82	-
	R2	0.52	0.64	0.31	0.43	0.55	0.43	0.36	0.52	0.46	7.25	0.64	-
	R3	0.99	1.74	2.12	1.05	1.17	1.63	0.96	1.00	1.09	1.49	1.54	-
F7	R1	1.35	-	1.02	26.42	22.83	21.30	1.30	1.16	21.70	27.10	19.61	17.28
	R2	0.30	-	0.34	11.80	10.67	0.18	0.42	0.44	7.57	16.00	12.83	11.82
	R3	0.82	-	0.65	24.11	9.34	6.51	1.16	1.01	21.81	30.20	23.84	19.25
F5	R1	1.48	-	22.42	11.26	11.15	8.08	8.17	7.70	3.91	4.90	4.37	4.78
	R2	0.26	-	5.47	0.58	0.47	0.25	0.47	0.47	0.28	0.32	0.31	0.32
	R3	3.32	-	3.90	0.43	0.81	0.45	0.47	0.35	0.29	0.30	0.44	0.32
Minimum		0.26	0.64	0.31	0.23	0.10	0.18	0.35	0.33	0.28	0.30	0.31	0.32
Maximum		9.93	12.92	22.42	26.42	22.83	21.30	8.17	7.70	21.81	30.20	23.84	19.25
Average		2.36	6.41	3.54	6.61	4.98	3.63	1.54	1.65	5.14	7.79	5.67	8.96
Standard Deviation		2.90	4.95	6.18	9.66	7.10	6.14	2.18	2.14	8.04	10.72	8.31	8.37

Table C.3.- Corrosion rates (μm/year) of submerged probes in HPC-Fly Ash beams.

Beam	Probe	Exposure time in solution (weeks)											
		0.5	4.5	8.5	12	14	16	20	22	23	24	25	26
F9	R1	1.79	1.32	1.28	1.49	1.41	1.28	0.72	1.26	2.00	3.18	2.58	-
	R2	0.12	0.17	0.06	0.41	0.23	0.22	0.14	0.21	0.19	1.30	0.31	-
	R3	1.60	1.38	0.10	0.87	1.63	1.42	1.06	1.42	1.33	1.27	1.36	-
F8	R1	0.16	1.36	1.00	1.32	1.33	1.07	1.24	1.18	1.30	1.37	1.34	-
	R2	0.12	0.22	0.15	0.20	0.29	0.29	0.19	0.25	0.34	0.48	0.40	-
	R3	2.22	1.05	0.68	1.01	1.01	0.81	0.82	0.93	0.94	1.01	0.86	-
F7	R1	0.94	-	1.58	1.05	1.19	0.90	0.99	1.08	0.71	0.58	0.69	0.67
	R2	0.60	-	1.26	0.59	0.56	0.49	0.50	0.53	0.43	0.52	0.37	0.37
	R3	1.57	-	0.99	1.65	1.67	0.96	0.83	0.88	0.52	0.54	0.48	0.46
F5	R1	0.38	-	0.72	0.84	0.89	0.69	0.76	0.74	0.45	0.47	0.46	0.51
	R2	0.14	-	0.13	0.35	0.23	0.20	0.24	0.28	0.20	0.23	0.25	0.29
	R3	0.35	-	0.61	0.29	0.69	0.58	0.58	0.35	0.40	0.51	0.48	0.44
Minimum		0.12	0.17	0.06	0.20	0.23	0.20	0.14	0.21	0.19	0.23	0.25	0.29
Maximum		2.22	1.38	1.58	1.65	1.67	1.42	1.24	1.42	2.00	3.18	2.58	0.67
Average		0.83	0.92	0.71	0.84	0.93	0.74	0.67	0.76	0.73	0.96	0.80	0.46
Standard Deviation		0.76	0.57	0.52	0.48	0.53	0.40	0.35	0.43	0.55	0.80	0.67	0.13

Table C.4.- Corrosion rates (μm/year) of non-submerged probes in HPC-Slag beams.

Beam	Probe	Exposure time in solution (weeks)						
		0.5	4.5	8.5	14	16	20	22
S9	R1	0.14	0.24	0.15	0.10	0.29	0.09	0.24
	R2	0.14	0.06	0.19	0.15	0.10	0.11	0.13
	R3	0.02	0.02	0.14	0.22	0.12	0.07	0.11
S6	R1	0.02	0.17	0.16	0.18	0.12	0.12	0.18
	R2	0.18	0.09	0.13	0.09	0.14	0.11	0.04
	R3	0.29	0.13	0.55	0.17	0.19	0.08	0.10
S2	R1	0.13	-	0.20	0.08	0.47	0.12	0.12
	R2	0.11	-	0.10	0.09	0.11	0.13	0.16
	R3	0.19	-	0.19	0.12	0.10	0.04	0.11
S3	R1	0.24	-	0.30	0.18	0.20	0.22	0.34
	R2	0.08	-	0.11	0.08	0.09	0.30	0.08
	R3	0.36	-	0.32	0.34	0.25	0.21	0.26
Minimum		0.02	0.02	0.10	0.08	0.09	0.04	0.04
Maximum		0.36	0.24	0.55	0.34	0.47	0.30	0.34
Average		0.16	0.12	0.21	0.15	0.18	0.13	0.16
Standard Deviation		0.10	0.08	0.13	0.07	0.11	0.07	0.09

Table C.5.- Corrosion rates (μm/year) of probes at the crack in HPC-Slag beams.

Beam	Probe	Exposure time in solution (weeks)											
		0.5	4.5	8.5	12	14	16	20	22	23	24	25	26
S9	R1	16.13	23.39	63.22	73.48	50.53	44.88	38.75	39.45	47.88	49.80	59.90	-
	R2	3.92	4.73	5.47	18.28	3.70	10.48	3.91	3.27	1.87	1.79	2.02	-
	R3	18.04	99.91	33.02	46.76	32.83	23.53	16.08	13.18	14.32	15.30	15.45	-
S6	R1	8.15	38.00	7.86	0.96	0.64	1.80	0.37	0.17	0.28	0.20	0.32	-
	R2	5.52	5.63	2.49	10.78	3.21	3.30	2.16	1.37	2.64	1.96	5.95	-
	R3	25.01	33.95	13.69	24.36	4.30	2.21	1.63	17.80	22.30	26.05	20.18	-
S2	R1	10.47	-	20.26	5.94	3.38	5.00	2.85	15.10	2.66	10.85	4.85	7.10
	R2	0.85	-	8.09	1.16	0.94	2.20	1.17	4.69	0.42	0.93	0.65	0.77
	R3	1.12	-	5.72	4.77	3.69	4.92	2.22	12.43	7.36	5.12	13.17	10.83
S3	R1	7.42	-	15.46	0.74	0.98	0.48	0.71	0.93	0.26	0.31	0.35	0.15
	R2	0.61	-	1.23	0.51	0.74	0.26	0.49	0.13	0.25	0.31	0.20	0.24
	R3	9.44	-	15.26	0.76	0.80	0.60	0.52	0.70	0.23	0.25	0.20	0.25
Minimum		0.61	4.73	1.23	0.51	0.64	0.26	0.37	0.13	0.23	0.20	0.20	0.15
Maximum		25.01	99.91	63.22	73.48	50.53	44.88	38.75	39.45	47.88	49.80	59.90	10.83
Average		8.89	34.27	15.98	15.71	8.81	8.30	5.91	9.10	8.37	9.41	10.27	3.22
Standard Deviation		7.58	35.03	17.29	22.82	15.87	13.22	11.20	11.57	14.22	15.02	17.07	4.61

Table C.6.- Corrosion rates (μm/year) of submerged probes in HPC-Slag beams.

Beam	Probe	Exposure time in solution (weeks)											
		0.5	4.5	8.5	12	14	16	20	22	23	24	25	26
S9	R1	0.26	8.55	1.30	1.98	0.59	1.61	0.95	1.02	0.85	0.68	0.97	-
	R2	0.25	4.75	2.41	2.93	0.89	1.84	0.83	0.53	0.69	0.53	0.53	-
	R3	1.17	3.06	3.11	0.51	2.11	1.54	1.05	1.14	1.13	1.13	1.14	-
S6	R1	0.17	11.23	0.62	1.25	1.57	2.07	6.06	1.91	3.35	3.92	3.94	-
	R2	0.09	0.78	0.15	1.39	0.24	0.13	0.46	0.61	0.50	1.14	0.45	-
	R3	2.78	1.73	0.55	1.75	0.99	0.76	0.15	0.28	0.50	0.65	0.38	-
S2	R1	1.06	-	1.48	0.53	0.82	0.75	1.13	1.75	0.79	0.87	0.95	0.79
	R2	1.02	-	1.36	0.68	1.71	0.80	1.13	1.34	0.79	1.17	0.99	0.93
	R3	0.36	-	1.96	0.63	1.03	0.72	1.15	1.80	0.67	0.72	0.83	0.90
S3	R1	3.62	-	8.53	0.50	0.94	2.77	1.68	1.61	3.66	4.40	1.98	2.01
	R2	3.66	-	3.12	1.68	5.85	3.43	5.35	5.98	3.89	4.04	1.26	1.05
	R3	0.15	-	10.91	0.73	0.86	0.63	0.99	0.82	0.40	0.45	0.40	0.42
Minimum		0.09	0.78	0.15	0.50	0.24	0.13	0.15	0.28	0.40	0.45	0.38	0.42
Maximum		3.66	11.23	10.91	2.94	5.85	3.43	6.06	5.98	3.89	4.40	3.94	2.01
Average		1.22	5.02	2.96	1.21	1.47	1.42	1.74	1.57	1.44	1.64	1.15	1.02
Standard Deviation		1.36	4.09	3.33	0.76	1.47	0.98	1.89	1.49	1.34	1.52	0.99	0.53

Table C.7.- Corrosion rates (μm/year) of non-submerged probes in OPC-C beams.

Beam	Probe	Exposure time in solution (weeks)						
		0.5	4.5	8.5	14	16	20	22
C6	R1	0.03	0.13	0.08	0.01	0.09	0.06	0.08
	R2	0.10	0.04	0.36	0.46	0.22	0.15	0.15
	R3	0.06	0.28	0.30	0.10	0.17	0.09	0.14
C2	R1	0.13	0.12	0.08	0.08	0.05	0.11	0.08
	R2	0.07	0.04	0.05	0.12	0.12	0.17	0.08
	R3	0.08	0.12	0.04	0.08	0.01	0.05	0.06
C5	R1	0.12	-	0.09	0.27	0.15	0.12	0.27
	R2	0.10	-	0.11	0.09	0.15	0.19	0.20
	R3	0.08	-	0.14	0.12	0.11	0.30	0.21
C4	R1	0.11	-	0.13	0.12	0.06	0.18	0.16
	R2	0.09	-	0.12	0.15	0.10	0.10	0.08
	R3	0.05	-	0.21	0.26	0.09	0.05	0.13
Minimum		0.03	0.04	0.04	0.01	0.01	0.05	0.06
Maximum		0.13	0.28	0.36	0.46	0.22	0.30	0.27
Average		0.09	0.12	0.14	0.15	0.11	0.13	0.14
Standard Deviation		0.03	0.09	0.10	0.12	0.06	0.07	0.06

Table C.8.- Corrosion rates (μm/year) of probes at the crack in OPC-C beams.

Beam	Probe	Exposure time in solution (weeks)											
		0.5	4.5	8.5	12	14	16	20	22	23	24	25	26
C6	R1	2.55	4.23	7.90	-	7.58	0.74	3.27	2.43	2.78	1.92	2.52	-
	R2	0.72	3.27	7.51	-	0.28	0.64	2.57	1.75	3.11	5.32	4.17	-
	R3	4.30	6.24	9.88	-	3.92	2.22	3.79	3.26	3.45	3.92	4.83	-
C2	R1	3.91	6.73	1.30	-	1.28	0.66	12.1	17.7	45.47	44.14	44.26	-
	R2	1.16	3.91	0.61	-	0.27	0.24	1.20	3.02	4.62	7.98	6.82	-
	R3	11.2	11.8	2.17	-	0.39	0.22	7.27	10.2	2.98	4.94	2.95	-
C5	R1	2.67	-	18.9	9.49	0.09	0.15	0.06	0.64	0.97	2.26	1.51	2.30
	R2	1.34	-	6.25	0.87	0.41	2.95	1.47	2.44	0.30	0.42	0.81	1.36
	R3	2.60	-	44.3	1.86	0.69	3.01	1.99	1.74	0.50	0.58	0.87	1.46
C4	R1	5.54	-	9.85	2.27	1.44	0.92	2.61	1.50	97.5	141.5	34.34	61.59
	R2	1.20	-	4.83	0.62	0.58	0.29	0.31	0.72	19.9	19.7	8.16	10.62
	R3	11.6	-	3.66	3.47	2.26	0.98	0.73	1.06	13.6	15.4	6.58	7.97
Minimum		0.72	3.27	0.61	0.62	0.09	0.15	0.06	0.64	0.30	0.42	0.81	1.36
Maximum		11.57	11.79	44.33	9.49	7.58	3.01	12.05	17.72	97.50	141.5	44.26	61.59
Average		4.06	6.03	9.77	3.10	1.60	1.09	3.11	3.87	16.27	20.67	9.82	14.22
Standard Deviation		3.71	3.13	11.96	3.30	2.18	1.04	3.42	5.04	28.67	40.01	14.13	23.52

Table C.9.- Corrosion rates (μm/year) of submerged probes in OPC-C beams.

Beam	Probe	Exposure time in solution (weeks)											
		0.5	4.5	8.5	12	14	16	20	22	23	24	25	26
C6	R1	2.00	3.14	0.92	-	0.64	0.38	0.37	0.26	0.32	0.36	0.31	-
	R2	0.37	0.77	0.29	-	0.23	0.19	0.12	0.17	0.14	0.55	0.17	-
	R3	1.91	3.65	0.90	-	0.50	0.36	0.38	0.42	0.53	0.49	0.70	-
C2	R1	4.85	5.14	1.52	-	1.52	0.72	0.63	0.62	0.59	0.46	0.53	-
	R2	4.94	7.23	1.57	-	1.83	0.81	0.61	0.76	0.52	0.43	0.51	-
	R3	4.80	7.14	1.57	-	2.04	1.10	0.98	0.81	0.75	0.86	0.66	-
C5	R1	0.75	-	4.70	0.94	0.12	0.11	0.32	0.16	0.41	0.37	0.38	0.45
	R2	0.36	-	10.86	0.46	0.49	0.57	0.44	0.71	0.28	0.32	0.36	0.26
	R3	1.31	-	16.32	1.22	1.00	0.82	0.75	0.96	0.48	0.47	0.48	0.55
C4	R1	0.16	-	9.31	2.14	3.67	3.70	1.83	2.38	1.18	1.21	0.38	0.53
	R2	0.83	-	0.72	1.45	1.42	2.53	1.19	1.10	0.33	0.20	0.38	0.45
	R3	0.13	-	12.31	3.12	1.99	2.39	2.13	3.34	0.38	0.39	0.49	0.22
Minimum		0.13	0.77	0.29	0.46	0.12	0.11	0.12	0.16	0.14	0.20	0.17	0.22
Maximum		4.94	7.23	16.32	3.12	3.67	3.70	2.13	3.34	1.18	1.21	0.70	0.55
Average		1.87	4.51	5.08	1.56	1.29	1.14	0.81	0.97	0.49	0.51	0.45	0.41
Standard Deviation		1.91	2.50	5.59	0.95	1.02	1.12	0.62	0.95	0.27	0.27	0.15	0.14

Table C.10.- Corrosion rates (μm/year) of non-submerged probes in OPC-TC beams.

Beam	Probe	Exposure time in solution (weeks)						
		0.5	4.5	8.5	14	16	20	22
TC9	R1	0.07	0.05	0.12	0.10	0.17	0.09	0.01
	R2	0.09	0.00	0.01	0.21	0.06	0.11	0.13
	R3	0.15	0.16	0.11	0.65	0.04	0.09	0.08
TC7	R1	0.06	0.27	0.16	0.24	0.11	0.08	0.07
	R2	0.13	0.08	0.04	0.22	0.07	0.10	0.07
	R3	0.06	0.12	0.08	0.13	0.25	0.07	0.04
TC1	R1	0.09	-	0.06	0.22	0.00	0.07	0.63
	R2	0.11	-	0.11	0.33	0.07	0.06	0.62
	R3	0.02	-	0.24	0.08	0.23	0.30	0.80
TC10	R1	0.24	-	0.17	0.16	0.17	0.19	0.01
	R2	0.06	-	0.13	0.10	0.13	0.09	0.46
	R3	0.17	-	0.13	0.15	0.15	0.14	0.43
Minimum		0.02	0.00	0.01	0.08	0.00	0.06	0.01
Maximum		0.24	0.27	0.24	0.65	0.25	0.30	0.80
Average		0.10	0.11	0.11	0.22	0.12	0.12	0.28
Standard Deviation		0.06	0.09	0.06	0.15	0.07	0.07	0.28

Table C.11.- Corrosion rates (μm/year) of probes at the crack in OPC-TC beams.

Beam	Probe	Exposure time in solution (weeks)											
		0.5	4.5	8.5	12	14	16	20	22	23	24	25	26
TC9	R1	6.46	3.01	3.88	2.30	0.65	24.84	3.01	0.50	5.22	10.56	14.85	-
	R2	0.92	1.72	13.35	12.18	7.93	7.44	6.11	9.29	6.32	5.23	8.65	-
	R3	8.23	6.14	16.11	12.19	10.91	6.76	4.51	5.82	5.63	5.49	11.30	-
TC7	R1	2.38	6.66	25.19	6.40	5.54	33.13	33.94	48.31	34.63	34.80	36.89	-
	R2	0.55	0.81	15.86	2.22	0.72	2.56	6.02	5.74	9.89	5.05	9.99	-
	R3	5.75	10.81	58.26	11.13	9.47	0.02	4.95	43.36	26.97	28.60	23.26	-
TC1	R1	3.19	-	60.82	21.18	23.53	3.32	8.24	4.87	47.04	49.30	44.43	45.47
	R2	54.18	-	2.68	13.79	11.99	1.20	0.60	1.06	5.75	7.09	7.61	6.23
	R3	5.84	-	20.96	37.97	24.07	27.70	24.40	4.95	98.01	113.10	204.7	204.2
TC10	R1	2.80	-	2.58	0.97	2.82	10.63	6.00	15.79	1.42	3.78	4.75	6.28
	R2	0.43	-	1.02	0.44	1.86	0.94	0.50	1.21	0.41	0.34	0.35	0.47
	R3	2.31	-	14.37	1.45	3.46	0.23	3.96	3.15	0.89	1.05	1.03	1.33
Minimum		0.429	0.81	1.02	0.44	0.65	0.02	0.50	0.50	0.41	0.34	0.35	0.47
Maximum		54.18	10.81	60.82	37.97	24.07	33.13	33.94	39.79	98.01	113.10	204.7	204.2
Average		7.75	4.86	19.59	10.19	8.58	9.90	8.52	10.71	20.18	22.03	30.65	43.99
Standard Deviation		14.84	3.74	20.20	10.92	8.09	11.83	10.11	13.45	28.75	32.59	56.51	80.27

Table C.12.- Corrosion rates (μm/year) of submerged probes in OPC-TC beams.

Beam	Probe	Exposure time in solution (weeks)											
		0.5	4.5	8.5	12	14	16	20	22	23	24	25	26
TC9	R1	0.09	3.73	0.16	0.68	0.46	0.06	0.18	0.17	0.12	0.08	0.29	-
	R2	0.18	4.56	0.01	0.79	0.37	0.25	0.02	0.17	0.13	0.23	0.25	-
	R3	0.004	10.04	0.48	0.89	0.69	0.26	0.26	0.17	0.18	0.08	0.24	-
TC7	R1	0.10	25.45	2.45	1.12	0.77	0.43	0.10	0.28	0.25	0.12	0.29	-
	R2	0.06	6.10	2.00	0.53	0.42	0.29	0.21	0.26	0.34	0.40	0.18	-
	R3	0.09	46.28	0.94	1.14	0.60	0.16	0.26	0.25	0.24	0.35	0.27	-
TC1	R1	0.14	-	20.68	0.35	0.68	0.68	0.39	0.33	0.28	0.29	0.28	0.45
	R2	0.13	-	6.11	0.37	0.49	0.42	0.48	0.85	0.27	0.34	0.33	0.32
	R3	0.23	-	3.66	0.45	0.58	0.65	0.51	0.62	0.30	0.30	0.30	0.34
TC10	R1	0.04	-	2.30	0.09	0.21	0.18	0.18	0.53	0.17	0.14	0.14	0.19
	R2	0.09	-	1.21	0.17	0.14	0.14	0.15	0.50	0.12	0.15	0.21	0.16
	R3	0.12	-	2.33	0.19	0.18	0.17	0.38	0.33	0.15	0.17	0.31	0.36
Minimum		0.004	3.73	0.01	0.09	0.14	0.06	0.02	0.17	0.12	0.08	0.06	0.11
Maximum		0.23	46.28	20.68	1.14	0.77	0.68	0.51	0.85	0.34	0.40	0.14	0.16
Average		0.11	16.03	3.53	0.56	0.47	0.31	0.26	0.37	0.21	0.22	0.33	0.45
Standard Deviation		0.06	16.86	5.66	0.36	0.21	0.20	0.15	0.21	0.08	0.11	0.26	0.30